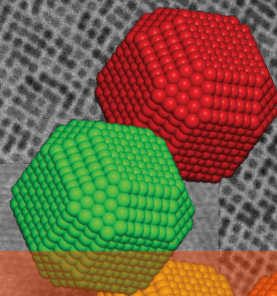
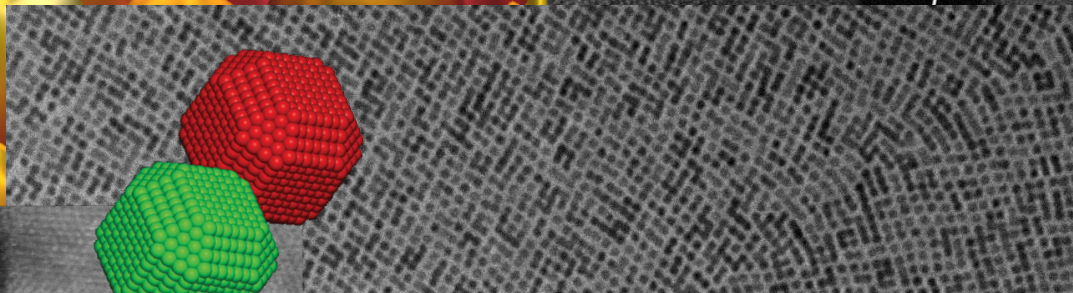
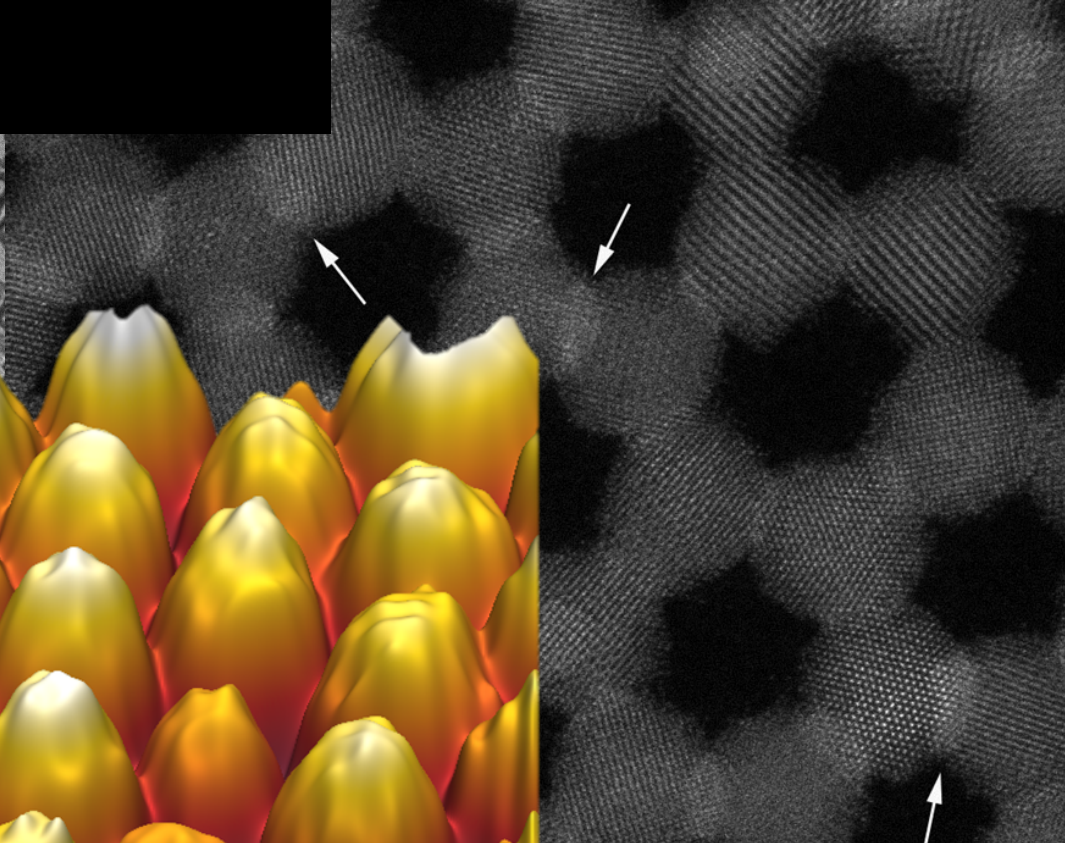
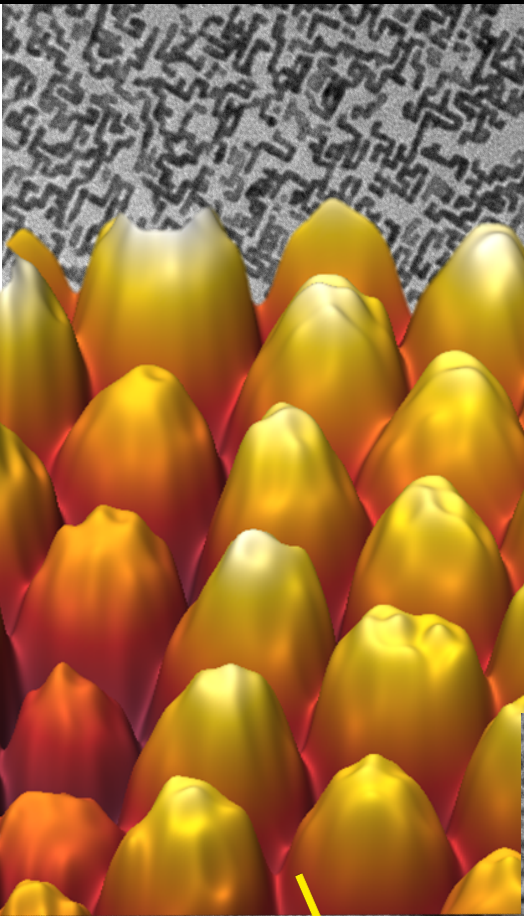
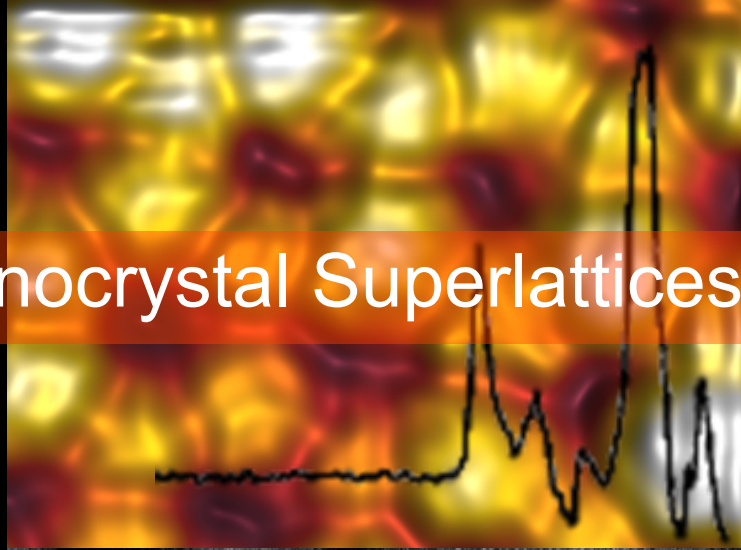
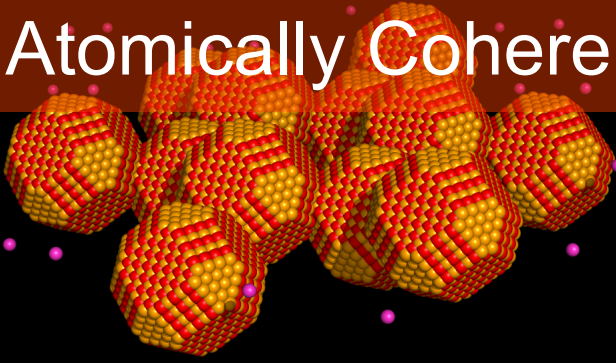


# Atomically Coherent Nanocrystal Superlattices



Master Thesis  
J.J. Geuchies

Supervision:  
Prof. dr. D. Vanmaekelbergh  
M.Sc. M.P. Boneschanscher  
Dr. I. Swart

First name: Jacob Jan  
Last name: Geuchies  
Student number: 3849082  
Date: August 15, 2013  
Advisor 1: Prof. dr. Daniel Vanmaekelbergh  
Advisor 2: M. Sc. Mark P. Boneschanscher  
Advisor 3: Dr. Ingmar Swart

# Abstract

Many applications have been envisioned for supercrystals of quantum dots (QDs), ranging from solar cells to LEDs. The properties of such systems depend on the properties of the constituent particles, but also on the structure of the supercrystal. Especially the novel effects related to the formation of a superstructure remain to be addressed experimentally. Here we present a combined scanning tunneling microscopy (STM), electron microscopy (EM) and electron tomography study on the two-dimensional oriented attachment of PbSe QDs. Several different atomically coherent nanocrystal superlattices are formed with linear, cubic and honeycomb symmetry depending on the synthesis conditions. We show that the interpretation of STM and TEM data is not straightforward, hence we used electron-tomography to prove that the honeycomb crystal is actually buckled into a silicene like structure. Moreover, initial scanning tunneling spectroscopy results are presented and, combined with atomistic tight binding calculations, a first interpretation is given to the acquired spectra.

# List of abbreviations

AFM - Atomic Force Microscope  
BZ - Brillouin Zone  
CB - Conduction Band  
DBTJ - Double Barrier Tunnel Junction  
DFT - Density Functional Theory  
DOS - Density of States  
EDX - Energy Dispersive X-ray spectroscopy  
EELS - Electron Energy Loss Spectroscopy  
EG - Ethylene Glycol  
EM - Electron Microscopy  
FFT - Fast Fourier Transform  
FT - Fourier Transform  
HAADF - High Angle Annular Dark Field  
HOPG - Highly Ordered Pyrolytic Graphite  
HR SEM - High Resolution Scanning Electron Microscopy  
IR - Infrared  
IFT - Inverse Fourier Transform  
LDOS - Local Density of States  
LED - Light Emitting Diode  
LHe - Liquid Helium  
LN<sub>2</sub> - Liquid Nitrogen  
LT - Low Temperature  
MWS - Meerwein's Salt (triethyloxonium tetrafluoroborate)  
NC - Nanocrystal  
OA - Oleic Acid  
QD - Quantum Dot  
STEM - Scanning Transmission Electron Microscopy  
STM - Scanning Tunneling Microscope  
STS - Scanning Tunneling Spectroscopy  
TEM - Transmission Electron Microscopy  
UHV - Ultrahigh Vacuum  
VB - Valence Band  
VT - Variable Temperature  
2D - Two Dimensional  
3D - Three Dimensional

# Contents

|          |   |           |
|----------|---|-----------|
| <b>1</b> | <b>General introduction</b>   | <b>7</b>  |
| <b>2</b> | <b>Geometry and symmetry of nanocrystals and their supercrystals</b>                                    | <b>9</b>  |
| 2.1      | Nanocrystal geometry . . . . .  | 10        |
| 2.2      | Supercrystals: attachment and geometry . . . . .  | 14        |
| <b>3</b> | <b>Electronic structure of nanocrystals and their supercrystals</b>                                     | <b>16</b> |
| 3.1      | Electronic structure of bulk semiconductors . . . . .   | 17        |
| 3.2      | From Bulk to Nano - Quantum Confinement via a Top-Down approach . . . . .                               | 20        |
| 3.3      | From Bulk to Nano - Quantum Confinement via a Bottom-Up approach . . . . .                              | 21        |
| 3.4      | There and back again, from nano to bulk? Supercrystal symmetry dictating electronic structure . . . . . | 22        |
| <b>4</b> | <b>Observing the nano - Scanning Probe Microspectroscopy</b>  | <b>24</b> |
| 4.1      | Introduction - a short history of nearly everything . . . . .   | 25        |
| 4.2      | Quantum tunneling . . . . .   | 25        |
| 4.2.1    | Bardeen theory of tunneling . . . . .   | 26        |
| 4.2.2    | Scanning Tunneling Spectroscopy . . . . .   | 28        |
| 4.3      | STM/STS on quantum dots and supercrystals . . . . .   | 29        |
| <b>5</b> | <b>Experimental</b>   | <b>31</b> |
| 5.1      | Nanocrystal and supercrystal preparation . . . . .  | 32        |
| 5.2      | Scanning Probe Microscopy setup - the 'beast in the basement' . . . . .                                 | 32        |
| 5.2.1    | Preparation chamber . . . . .   | 33        |
| 5.2.2    | Analysis chamber - VT SPM . . . . .   | 33        |
| 5.2.3    | LT SPM - Combined STM/AFM setup . . . . .   | 33        |
| 5.3      | Electron microscopy . . . . .   | 34        |
| 5.4      | Electron tomography . . . . .   | 35        |
| <b>6</b> | <b>Results</b>  | <b>37</b> |
| 6.1      | Supercrystal synthesis . . . . .  | 38        |
| 6.1.1    | Synthesis stability . . . . .   | 39        |
| 6.1.2    | Stripping of surface capping - Meerwein's salt . . . . .  | 41        |
| 6.2      | Linear supercrystals . . . . .  | 42        |
| 6.2.1    | Anomalous facet attachment . . . . .  | 46        |
| 6.3      | Square supercrystals . . . . .  | 47        |
| 6.4      | Honeycomb supercrystals - geometry and electronic structure . . . . .                                   | 50        |
| 6.4.1    | Geometry - TEM . . . . .  | 50        |
| 6.4.2    | Geometry - STM . . . . .  | 51        |

|          |   |           |
|----------|---|-----------|
| 6.4.3    | Geometry - HR-SEM . . . . .   | 56        |
| 6.4.4    | Geometry - Electron Tomography . . . . .  | 59        |
| 6.4.5    | Geometry - HAADF-STEM . . . . .   | 61        |
| 6.4.6    | Electronic Structure - STS . . . . .  | 62        |
| <b>7</b> | <b>Conclusions and outlook</b>  | <b>68</b> |
| 7.1      | Conclusion and discussion . . . . .   | 68        |
| 7.2      | Outlook . . . . .   | 69        |
| 7.3      | Bibliography . . . . .  | 70        |
| <b>A</b> | <b>Ab Initio Density Functional Study of the Energetics of PbSe Nanocrystal Facets through Passivation by Capping Ligands</b> | <b>76</b> |
| <b>B</b> | <b>STM Tip Preparation by Electrochemical Etching and Fast Ion Bombardment</b>  | <b>82</b> |

# Chapter 1

## General introduction

“Before I refuse to take your questions, I have an opening statement.” - Ronald Reagan

The work described in this thesis is performed over the past two years. In close collaboration with numerous people the oriented attachment of PbSe nanocubes into atomically coherent nanocrystal superlattices was studied. The first chapters are a general introduction into the subject.

We start off with an explanation of the overall nanocrystal shapes in chapter two, with an emphasis on PbSe. It is shown that surface energy is the driving force in shaping the nanocrystals. Further discussions are held on the supercrystal geometries and via which crystal facets the nanocrystals attach.

The third chapter is devoted to understanding the electronic structure of the supercrystals. The chapter starts off with the theory of bulk semiconductors, which is followed by adding quantum confinement to the description in order to account for the finite size of the nanocrystals. A bridge is made between the two extrema to describe the electronic structure of the formed supercrystals.

The fourth chapter describes the workhorse of this thesis, namely scanning tunneling microscopy. After a short historical introduction several aspects of electron (hole) tunneling are given. We finish off with a brief description of scanning tunneling spectroscopy and its application to dielectric materials (such as semiconductor quantum dots).

Chapter five describes the experimental methods used to perform the work described in this thesis. The synthesis of the PbSe nanocrystals is very briefly described and followed by the description of the supercrystal synthesis. Furthermore electron microscopy is briefly explained and the microscopy setup available at the Condensed Matter and Interfaces lab is described.

Chapter six finally elaborates on the obtained results. It starts off with a short introduction into the synthesis method and how sensitive this is to external conditions (ligand concentration, glovebox atmosphere, etc.). The obtained supercrystals are presented after which the linear structures are described. The obtained square sheets are elaborated on after which the discussion on the honeycomb supercrystal, which was the main structure of interest, starts. It is shown that the scanning tunneling microscopy data of these supercrystals is quite misleading, which could be explained by the geometry of the supercrystal. The geometry of the supercrystal was unraveled by a number of different techniques, such as high resolution scanning electron microscopy, electron tomography and high-angle annular dark field scanning transmission electron microscopy. After presenting the results obtained on the geometry of the supercrystal, the description of the low temperature scanning tunneling microscopy experiments start. Various

forms of image contrast were obtained and could be explained by the sharpness/bluntness of the microscope's tip apex. The chapter finishes off with the initial scanning tunneling spectroscopy results acquired on the CdSe honeycomb supercrystals. The thesis ends with general conclusions, an outlook and acknowledgements.

## Chapter 2

# Geometry and symmetry of nanocrystals and their supercrystals

“There is geometry in the humming of the strings, there is music in the spacing of the spheres” - Pythagoras

The truncation of PbSe nanocrystals is of vital importance for the work described in this thesis. As each facet has a unique surface energy, it immediately implies that the reactivity also varies from facet to facet. This means that we can tune nanocrystal attachment by varying sample preparation parameters, such as concentration and temperature. This section deals with the equilibrium shape of PbSe nanocrystals, how this can be predicted by thermodynamics and can easily be constructed from simple geometrical arguments. Furthermore the final supercrystal geometry is discussed for various obtained structures and how the honeycomb structure can be constructed via two different attachments: graphene-like or silicene-like.

## 2.1 Nanocrystal geometry

The shape and geometry of nanocrystals is completely determined by equilibrium thermodynamics. Naively one could assume that all crystal facets will have identical surface energies, resulting in a spherical shape for all nanocrystals. In reality this is almost never observed, as the surface energy differs from crystal plane to crystal plane. This can be understood by numerous factors;

- Atoms in different crystal facets have different coordination numbers, i.e. number of neighbours. For example the three crystal facets of PbSe nanocrystals -  $\{100\}$ ,  $\{110\}$  and  $\{111\}$  - have coordination numbers of 8, 4 and 7 respectively.
- If the crystal is composed of multiple elements, the chemical environment of specific facets can vary as well. For example the  $\{100\}$  planes in PbSe are composed of alternating Pb and Se elements, while its  $\{111\}$  plane consists out of only Pb or Se.

The above described aspects will determine surface relaxation and reconstruction and are of vital importance for the nanocrystal shape, hence for the formation of the supercrystals in this thesis. Three different surfaces of a rocksalt crystal structure, which is the atomic crystal lattice of PbSe, are displayed in the figure below.

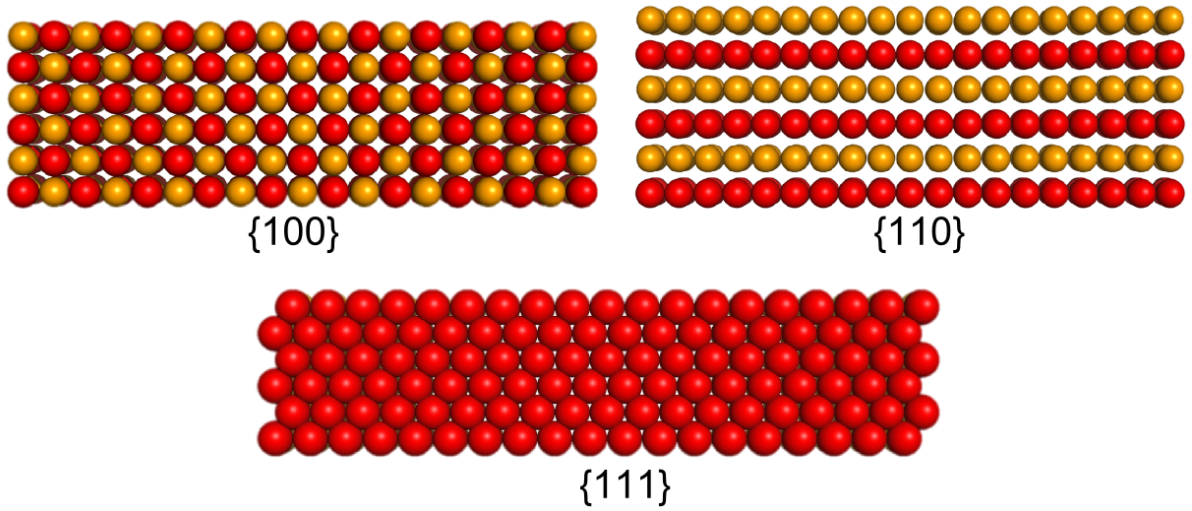


Figure 2.1: The relevant rocksalt FCC facets:  $\{100\}$ ,  $\{110\}$  and  $\{111\}$ . The truncation of the nanocrystals is caused by a difference in surface energy for each facet which in turn can be modified by different surface passivations

The thermodynamics of surfaces has been studied intensively [1; 2; 3]. It can be stated that the equilibrium crystal shape gives rise to the lowest free energy of the crystal. For nanocrystals only the surface energy gives a relevant contribution to the free energy. Hence we can write the total surface free energy as the sum of all crystal plane free energies;

$$G = \sum_i \gamma_i S_i \quad (2.1)$$

Where  $\gamma_i$  is the surface energy per unit area of facet  $i$  and  $S_i$  is the surface area of that specific crystal plane. The equilibrium geometry of the crystal is found by minimizing the free

energy of the crystal, hence - using the fact that  $\gamma_i$  is constant for every surface plane - we can write;

$$\delta G = \sum_i \gamma_i \delta S_i = 0 \quad (2.2)$$

To determine the equilibrium shape of a nanocrystal we need to assume that the surface free energy is proportional to a vector drawn from the center of the crystal to the specific facet. This is proven in the section below. Naturally, we require that the volume of the nanocrystal is conserved;

$$\delta V = \sum_i h_i \delta S_i + \sum_i S_i \delta h_i = 0 \quad (2.3)$$

The second term is equal to zero, as it corresponds to a change in volume of the crystal, hence the first term has to be equal to zero as well. Combining the above two equations we state that

$$\sum_i (h_i - \lambda \gamma_i) = 0 \quad (2.4)$$

As the shape is arbitrary, we require that  $h_i = \lambda \gamma_i$ , where  $\lambda$  is a proportionality constant. This is known as the Gibbs-Wulff theorem. It states that the distance of a surface plane from the center-of-mass of the crystal is proportional to the surface energy of this plane [4; 5]. This allows us to predict a (nano)crystal's equilibrium geometry, which is known as the Wulff construction. It is demonstrated in 2D for the PbSe truncated nanocubes.

The Wulff reconstruction is indicated in the figure below in four steps. The first step is to draw a cubic sheet of the material or crystal of interest, indicated in (A). Step two is to draw the surface tensions of the different crystal facets - as calculated from theory or measured in experiments - as a vector perpendicular to its crystal plane, as indicated in (B). As can be seen, the obtained nanocrystal will be spherical if the surface energy is independent of the crystal planes (*i.e.*  $\gamma_i$  is equivalent for all crystal facets), indicated by the dashed red line in the figure. *E.g.* the [10] direction is proportional to its surface energy  $\gamma_{[10]}$ . Step three is to draw lines perpendicular to all the surface energy vectors  $\bar{\gamma}_i$  as shown in (C). The smallest enclosed surface by these lines determines the degree of truncation. The final nanocrystal shape is indicated in (D), where the entire crystal is truncated in the [11] direction. In 3D the procedure is identical, but instead of drawing lines one has to draw planes normal to the surface energy vector, and the smallest enclosed volume by these planes determines the degree of truncation [6].

From geometrical arguments it can be easily shown that the PbSe nanocrystals will be fully truncated, *i.e.* the {110} and {111} will be cut off. The surface tensions of unpassified PbSe are taken from [2] and are shown below;

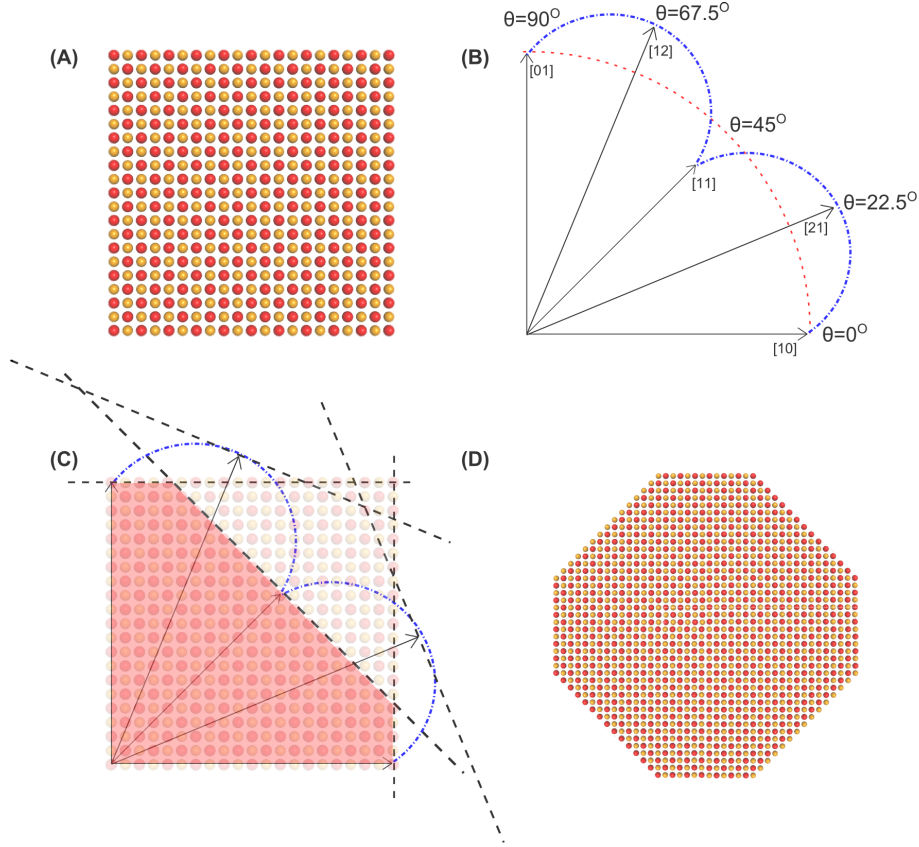


Figure 2.2: Wulff construction of a truncated PbSe nanocrystal in 2D. (A) The square [10] plane of a 2D PbSe sheet. (B) Vector representation of the different surface tensions. (C) The actual reconstruction, the enclosed volume is marked red. (D) The final 2D PbSe sheet, which has been truncated in all [11] directions.

$$\gamma_{100} = 0.184 \text{ Jm}^{-2}$$

$$\gamma_{110} = 0.318 \text{ Jm}^{-2}$$

$$\gamma_{111} = 0.419 \text{ Jm}^{-2} \text{ for a nonpolar Se terminated facet } ^1$$

$$\gamma_{111} = 0.328 \text{ Jm}^{-2} \text{ for a nonpolar Pb terminated facet}$$

In order for the  $\{110\}$  facet to be truncated, the surface tension vector of this facet has to be smaller than  $\sqrt{2}$  times the surface tension vector of the  $\{100\}$  facet, *i.e.*  $\gamma_{110} < \sqrt{2} \gamma_{100}$ . The same geometrical arguments hold for the  $\{111\}$  facet:  $\gamma_{111} < \sqrt{3} \gamma_{100}$ . This is clearly not the case for the unpassivated PbSe nanocrystals.

Recent DFT calculations on oleic acid capped PbSe nanocrystals have shown that the  $\{111\}$  facet will be truncated [2]. The surface energy calculated for this plane is approximately  $0.120 \text{ Jm}^{-2}$ , which causes a high degree of truncation. It has to be noted however, that the surface energy depends on the equilibrium ligand coverage on that specific facet [1]:

$$\Theta_{equi}^{hkl} = \frac{\frac{c}{c_0} \exp\left(\frac{-E_{bind}}{k_b T}\right)}{1 + \frac{c}{c_0} \exp\left(\frac{-E_{bind}}{k_b T}\right)} \quad (2.5)$$

<sup>1</sup>The polar facets were found to be unstable for both the Pb and Se terminated configurations.

Where  $\Theta_{equi}^{hkl}$  is the equilibrium ligand coverage of a  $\{hkl\}$  at ligand concentration  $c$  which binds with an energy  $E_{bind}$  to the specific facet at a temperature  $T$ .  $C_0$  is the critical concentration of ligands in solution. A model of a fully truncated nanocrystal, which will be used throughout this thesis, is shown below.

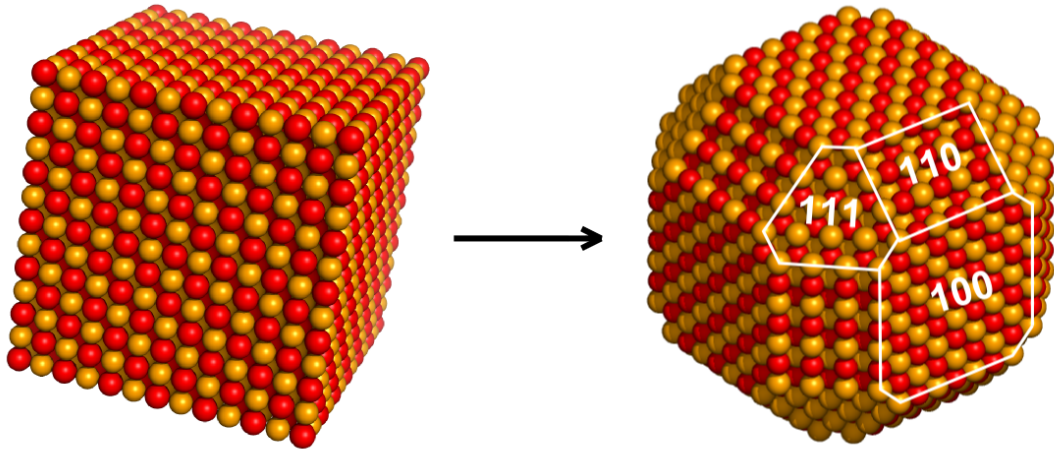


Figure 2.3: From a PbSe nanocube to a fully truncated PbSe nanocube. The truncation is induced by the unique surface tensions of the different facets. The  $\{100\}$ ,  $\{110\}$  and  $\{111\}$  facets are indicated in the figure on the right.

## 2.2 Supercrystals: attachment and geometry

As described in the experimental section we are able to synthesize different atomically coherent supercrystals depending on the preparation conditions [7];

- 1D supercrystal - linear lattice via  $\{100\}$  facet attachment
- 2D supercrystal - square lattice via  $\{100\}$  facet attachment
- 2D supercrystal - honeycomb lattice via  $\{110\}$  or  $\{111\}$  facet attachment

The various supercrystals are schematically depicted in the figure below;

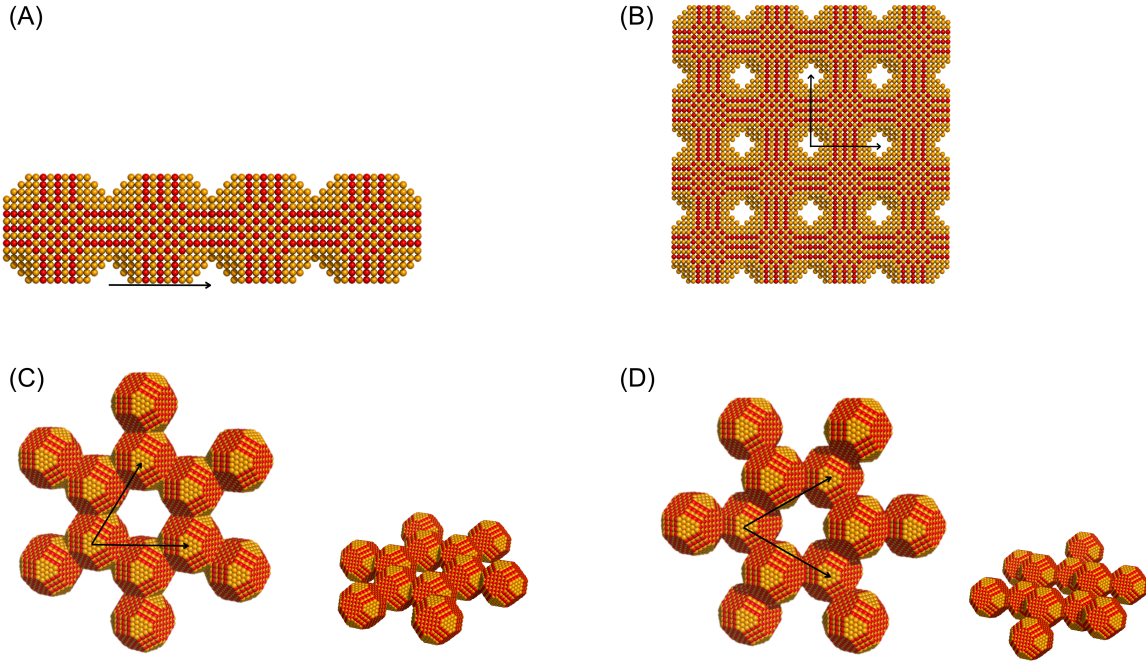


Figure 2.4: The various obtained supercrystals. (A) 1-D Linear superlattice, the nanocrystals are attached via the  $\{100\}$  facets. (B) Square superlattice, the nanocrystals are again attached via the  $\{100\}$  facets. (C) and (D) are representations of the honeycomb superlattice. This lattice can be realized by two different facet-attachments. (C) Graphene type superlattice, the nanocrystals are attached via the  $\{110\}$  facets, resulting in a supercrystal with the nanocrystals in one plane. (D) Silicene type superlattice, the nanocrystals are attached via the  $\{111\}$  facets, resulting in buckled supercrystal where neighbouring NCs are in two different planes.

The linear and square supercrystals both attach via the  $\{100\}$  facets. At relatively low concentrations the linear chains are formed, while at higher concentrations the square sheets dominate the sample coverage. At intermediate concentrations the sample is covered with the honeycomb structure for which two different configurations are possible; attachment via the  $\{110\}$  facets, resulting in a truly flat graphene-like structure and attachment via the  $\{111\}$  facets, resulting in a buckled silicene-like structure. Hence by tuning the concentration we can determine which region of phase space we enter.

As discussed in the previous section, the nanocrystal shape is vital for the formation of the supercrystals as each nanocrystal attaches via different reactive facets. Each facet has a unique

surface tension and hence different reactivity. By varying the sample preparation conditions (such as concentration, added amount of ligands and temperature) the supercrystal geometry can be tuned. The process is expected to occur in two steps (which is still in need of experimental verification);

- Adsorption and self-assembly at the liquid-air interface
- Attachment of specific facets and formation of atomic bonds

More information on the obtained superlattices and its formation can be found in the experimental and results chapters (chapter 5 and 6 respectively).

## Chapter 3

# Electronic structure of nanocrystals and their supercrystals

Semiconductor nanocrystals contain many interesting properties [8; 9]. One of the most remarkable features is the size dependent electronic structure, which are a result of quantum size effects. This section deals with the various theoretical description of these so called quantum dots from different points of view, i.e. via the bottom-up and top-down approach. Furthermore the electronic properties of the supercrystals will be discussed briefly.

### 3.1 Electronic structure of bulk semiconductors

To understand the unique properties of (colloidal) quantum dots, which originate from quantum confinement, it is instructive to first look at the electronic properties of bulk semiconductors. The electrons (and holes) moving throughout the semiconductor cannot be described by the free electron model; all charge carriers in the crystal experience the periodic potential imposed by the atomic lattice. The charge carriers still obey the Schrödinger equation [10];

$$\frac{-\hbar}{2m} \frac{\partial^2 \psi(x)}{\partial^2 x} + V(x)\psi(x) = E\psi(x) \quad (3.1)$$

Where  $\psi(x)$  is the wavefunction describing the system and  $V(x)$  is the periodic potential imposed by the lattice ions. Another way to view this Hamiltonian is that we have added the periodic potential as an external perturbation to the free electron kinetic energy. As  $V(x)$  is periodic with the lattice, the following must also hold;

$$\frac{-\hbar}{2m} \frac{\partial^2 \psi(x+a)}{\partial^2 x} + V(x)\psi(x+a) = E\psi(x+a) \quad (3.2)$$

Where  $a$  is the lattice constant in the  $x$  direction. After translation over a distance  $a$ , the wavefunction should have the same eigenvalue and hence  $\psi(x)$  and  $\psi(x+a)$  only can differ by a phase factor. This is the Bloch criterion and a wavefunction obeying this theorem is called a Bloch wave [11];

$$\psi_{block,k_x}(x) = e^{ik_x x} \cdot u_k(x) \quad (3.3)$$

Here  $k$  is defined as the wavevector ( $k_x = 2\pi/\lambda$ ) and  $u_k(x)$  is a function which is periodic with the atomic lattice. This Bloch wave consists of two parts; a plane wave ( $e^{ik_x x}$ ) which physically represents the phase (shift) of the wavefunction which in turn is modified by the periodic potential ( $u_k(x)$ ) of the lattice.

Another property of the Bloch waves is that the dispersion relation is very much altered by the periodic potential of the lattice. Electrons moving through the crystal with a wavelength differing from the lattice constant  $a$  are not much affected by the lattice, hence their energy is similar to that of a free electron. However when half of the electron wavelength is approximately equal to  $a$ , *i.e.* when  $k = \pi/a$ , the electrons are scattered by the atomic lattice. This is called Bragg reflection and the resulting standing wave is made by a linear combination of the two running waves with opposite momentum ( $k = \pi/a$  and  $k = -\pi/a$ ). The two resulting Bloch waves,  $\psi_{block}^+$  and  $\psi_{block}^-$ , are relatively similar but they are displaced by a factor  $a/2$ , as illustrated in figure 3.1;

This displacement factor causes an energy difference between the two waves; the first standing wave,  $\psi_{block}^+$ , concentrates the electron probability density above the ions, lowering the overall potential energy. However the second standing wave,  $\psi_{block}^-$ , concentrates the electron probability density between the ions, leading to an overall increase in energy. The energy difference between  $\psi_{block}^+$  and  $\psi_{block}^-$  leads to a discontinuity in the dispersion relation, opening an energy gap which is called the bandgap, which is displayed in figure 3.2;

Describing the crystal lattice with Bloch waves has another major advantage; wavefunctions which differ in  $k$  by a value of  $n2\pi/a$ , where  $n$  is an integer, are equivalent. Taking the minimum in energy at  $k = 0$ , all relevant  $k$ -values lie in the interval  $-\pi/a \leq k \leq \pi/a$ . This region of relevant  $k$ -values is called the first Brillouin zone (BZ). All  $k$ -values in neighbouring zones can be translated back into the first BZ by addition or subtraction of an integer times the reciprocal lattice vector  $\mathbf{G}(\tilde{\mathbf{r}})$  from the original  $k$ -value.

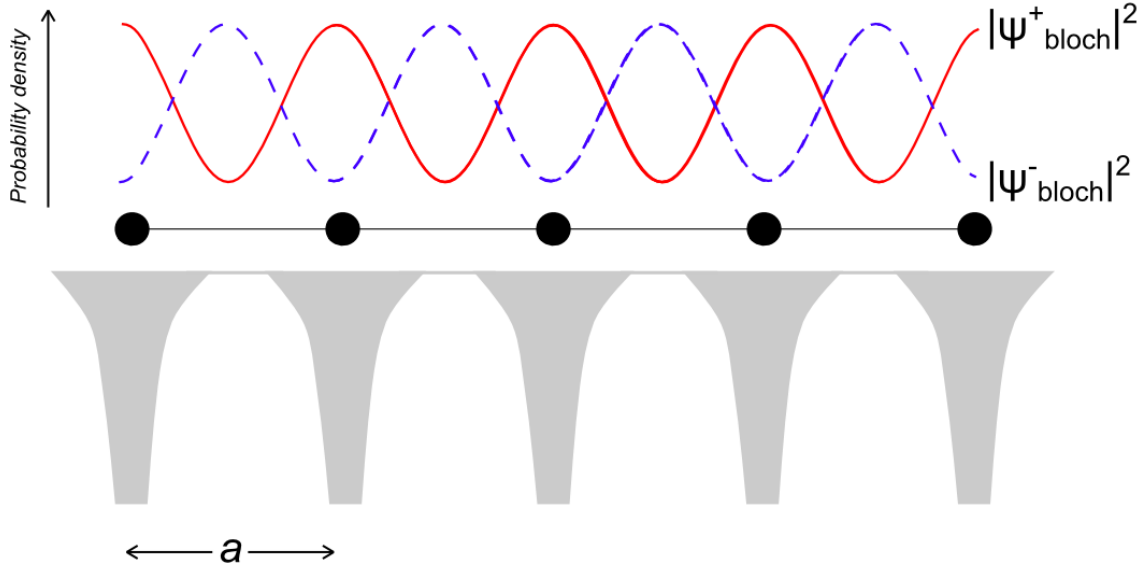


Figure 3.1: Illustration of Bragg reflection in a crystal. Two standing waves are formed at  $k = \pi/a$  and  $k = -\pi/a$  which are displaced by  $a/2$ . As these standing waves have a significant energy difference, a bandgap is opened at these  $k$  values.

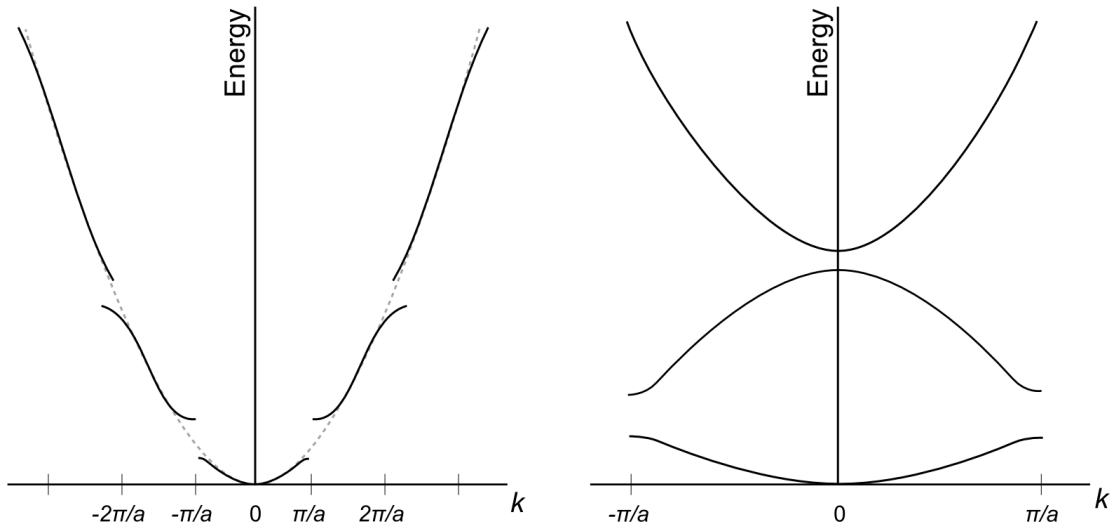


Figure 3.2: (A) Full band diagram, showing the opening of energy gaps at integer values of  $\pi/a$ . (B) Resulting dispersion relation by translation of the bands outside the first BZ by an integer times the reciprocal lattice vector.

Now what happens if we add two dimensions and describe the crystal in 3D? We can apply the same analogy as in the one-dimensional crystal, however the band structure becomes more complex; Bragg reflections occur when the wavefunction has the same periodicity as the lattice, but this periodicity differs in different directions of the crystal. As a consequence, bandgaps can open at various  $k$ -points, which are now defined as vectors from the center of the BZ. This point is referred to as the  $\Gamma$ -point ( $k_x = k_y = k_z = 0$ ). All high-symmetry points in the BZ are indicated with either a Greek letter (inside the BZ) or a Roman letter (on a vertex of the BZ).

As can be seen in the band diagram of bulk PbSe [12], figure 3.3, the valence band maximum

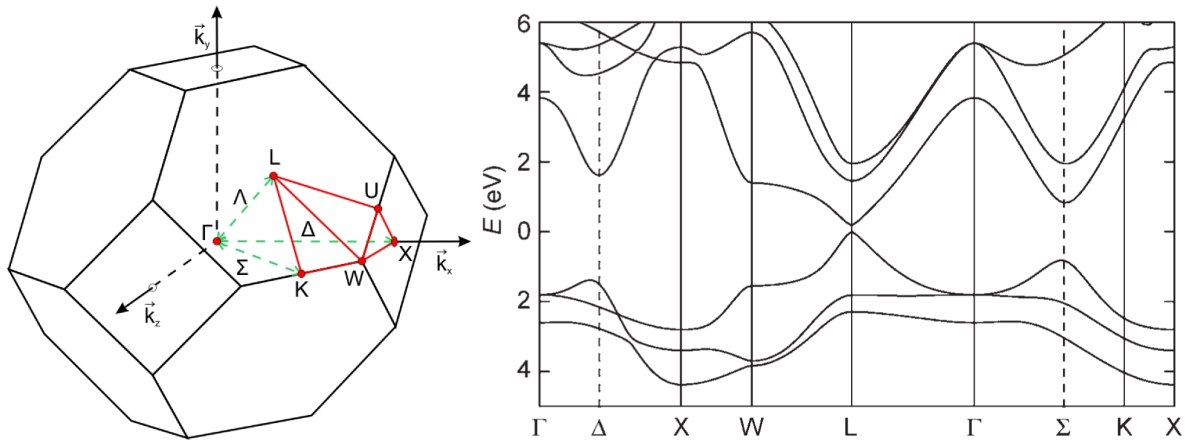


Figure 3.3: The first Brillouin zone of an FCC crystal structure. High symmetry points are indicated with Greek letters when the specific point is inside the zone and with Roman letters if the point is on one of the vertices. The image on the right displays the rich band structure of bulk PbSe, one of the materials which is being researched throughout this thesis.

and the conduction band minimum are at the same  $k$ -value. This means that an electron experiences no change in (angular) momentum and can be excited by absorption of a photon. These materials are referred to as direct semiconductors (i.e. they have a direct bandgap). If the conduction band minimum and valence band maximum have distinct  $k$ -values, the momentum of the electron has to be changed upon excitation. This is an unlikely (and so called  $k$ -forbidden) process as photons do not have enough momentum compared to the change in momentum associated with the electronic transition. These materials are called indirect semiconductors (i.e. they have an indirect bandgap). It is very tedious to draw the full dispersion relation for a 3D system. The convenient and most common way to plot the  $E - k$  relation for 3D semiconductors is displayed in figure 3.3 (B). The diagram is plotted along a route via various high symmetry points in the BZ. In the case of PbSe the bandgap lies at the  $L$ -point in the BZ. As the  $L$ -point is fourfold degenerate (each BZ has 8  $L$ -points which are shared with neighbouring BZ's), the bandgap becomes four-fold degenerate (eight-fold if we include spin degeneracy). This makes the electronic transitions in PbSe more complicated than for example CdSe, where the fundamental bandgap is located at the  $\Gamma$ -point [13].

## 3.2 From Bulk to Nano - Quantum Confinement via a Top-Down approach

So far the electronic description of semiconductors was based on infinitely sized crystals. However, in order to describe the properties of colloidal quantum dots one has to take the finite crystal size into account. In other words we need to confine the electron and hole wavefunctions inside the nanocrystal, an effect named quantum confinement. The basic concept from the top-down approach is that the bulk wavefunctions, described by Bloch waves, are modified for the electron and hole confinement by an envelope function [14; 15];

$$\Psi_{total}(\vec{r}) = \psi_{bloch}(\vec{r})\phi_{env}(\vec{r}) \quad (3.4)$$

The total wavefunction  $\Psi_{total}(\vec{r})$  is described as a product of the bulk Bloch wavefunction  $\psi_{bloch}(\vec{r})$  which is modified by the confinement of the charge carriers by an envelope wavefunction  $\phi_{env}(\vec{r})$ . It is convenient to describe  $\phi_{env}(\vec{r})$  by separation of variables into a radial part and an angular part as we are working with (nearly spherical) quantum dots. Instead of a particle in a box, the analogy of a particle in a spherical potential is used ( $u=0$  for  $r < a/2$ ,  $u=\infty$  for  $r > a/2$ );

$$\phi_{env}(\vec{r}) = Y_l^m(\theta, \Phi)R(r) \quad (3.5)$$

The envelope wavefunction is now rewritten into an angular part  $Y_l^m(\theta, \Phi)$  (spherical harmonics) and a radial part  $R(r)$  (radial Bessel function). Note the close resemblance with the hydrogen atom, where there is not a spherical potential well (as for the quantum dots), but a coulombic potential set up by the electron-proton interaction. When equation 3.4 is inserted into equation 3.1 and solved for its eigenvalues, the energies of the confined electron and hole are obtained;

$$E_{n,l}^{conf} = \frac{2\hbar^2\chi_{nl}^2}{m^*a^2} \quad (3.6)$$

Here  $m^*$  is the reduced electron (or hole) mass,  $\chi_{nl}$  are the  $n$ th roots of the  $l$ th order Bessel functions. The lowest energy electron and hole states are the 0th order bessel functions, hence they have S-symmetry. The higher order solutions are obtained for  $l=1,2,\dots$  and therefore obtain P,D, etc. symmetry. It is very illustrative to equate the bandgap of the nanocrystals now, including the confinement effects;

$$E_g^{tot}(a) = E_g^0 + E_{nl}^{conf}(a) = E_g^0 + \frac{2\hbar^2\chi_{nl}^2}{m_e^*a^2} + \frac{2\hbar^2\chi_{nl}^2}{m_h^*a^2} \quad (3.7)$$

The bandgap is now obtained by adding the confinement energies of both the electrons and holes (from equation 1.6). As can be seen, the bandgap increases with decreasing nanocrystal size  $a$ , scaling as  $a^{-2}$ . Also discrete energy states arise at the band edges, which are asymmetrically displaced with respect to the Fermi level for both electrons and holes. The above electron description provides the fundamental key for designing novel electronic semiconducting materials by varying only the size of the nanocrystal.

### 3.3 From Bulk to Nano - Quantum Confinement via a Bottom-Up approach

For most chemists the most common way to describe a semiconductor is to use the analogy with a large molecule [9]. Like in molecules, molecular orbital (MO) theory can be used. A linear combination is made of the constituent atomic orbitals (AO) to form new molecular orbitals, otherwise known as LCAO-MO. The most simple case where one can use this theory is that of diatomic hydrogen, where the 1s levels of the hydrogen atoms combine into two MO's; the bonding and anti-bonding level. As both electrons pair up in the bonding MO, there is a net energy gain.

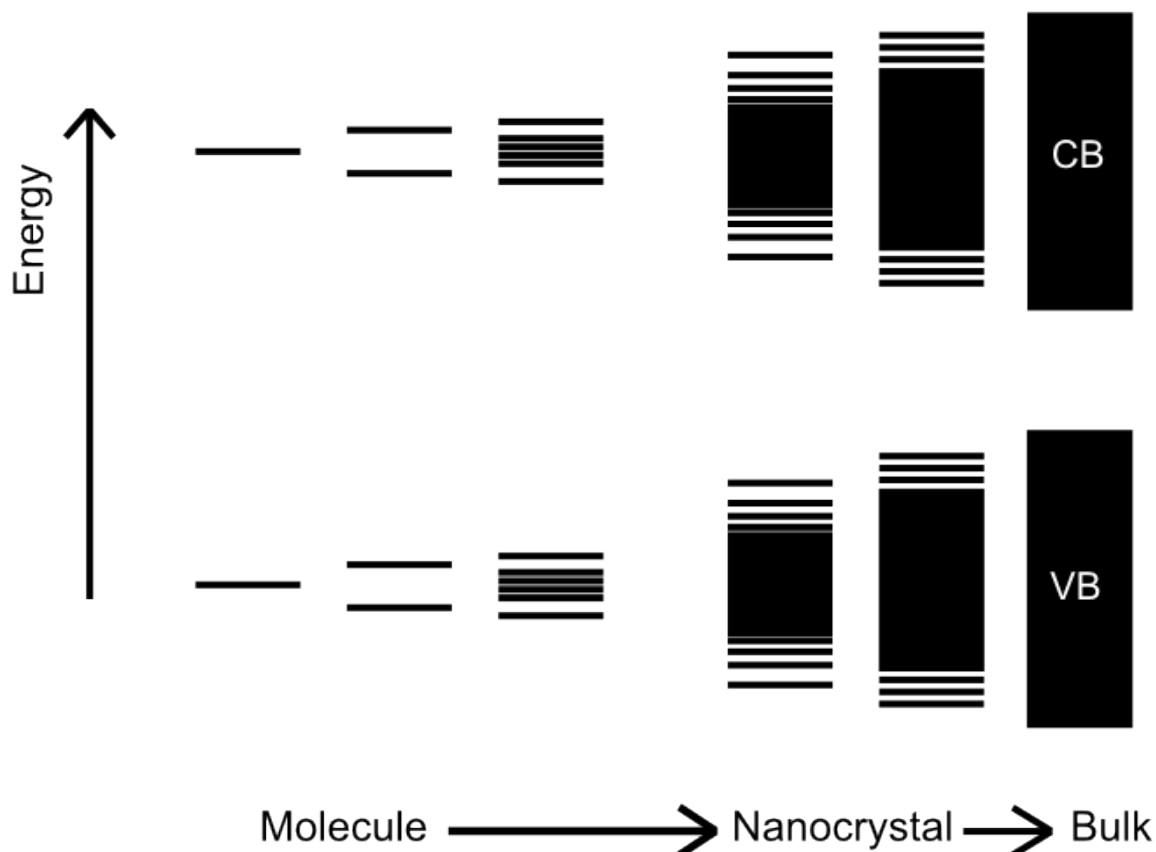


Figure 3.4: Progression of molecular orbitals as the number of atoms in a system increases from a few atoms (molecules) to a few 100 to 1000 atoms (nanocrystal) to bulk semiconductors

As the number of atoms increases, hence the number of AO's which contribute to the system, the MO diagram becomes more complex. Eventually the number of MO's which constitute to the system becomes so large and closely spaced in energy, that they are described as a continuum. In this continuum limit, the filled band is referred to as the valence band (VB) and the empty band is referred to as the conduction band (CB). In analogy with a more chemists point of view; the highest occupied energy level and the lowest unoccupied energy level are referred to as the HOMO and LUMO respectively. The energy difference between the highest occupied state and lowest occupied state is referred to as the bandgap in semiconductors.

### 3.4 There and back again, from nano to bulk? Supercrystal symmetry dictating electronic structure

Various atomically coherent nanocrystal superlattices can be obtained, depending on the exact synthesis conditions. The question that remains is if the remarkable properties of the colloidal quantum dots will be preserved or not. Depending on the quantum mechanical coupling strength (i.e. the wavefunction overlap between neighbouring nanocrystals) one can see individual nanocrystal behaviour or collective properties. However, since we have attached quantum dots, the reality will be a convolution of the two; the system will not behave as a 2-dimensional electron gas (2DEG) and neither as individual particles, depending on the contact area between the nanocrystals [16; 17].

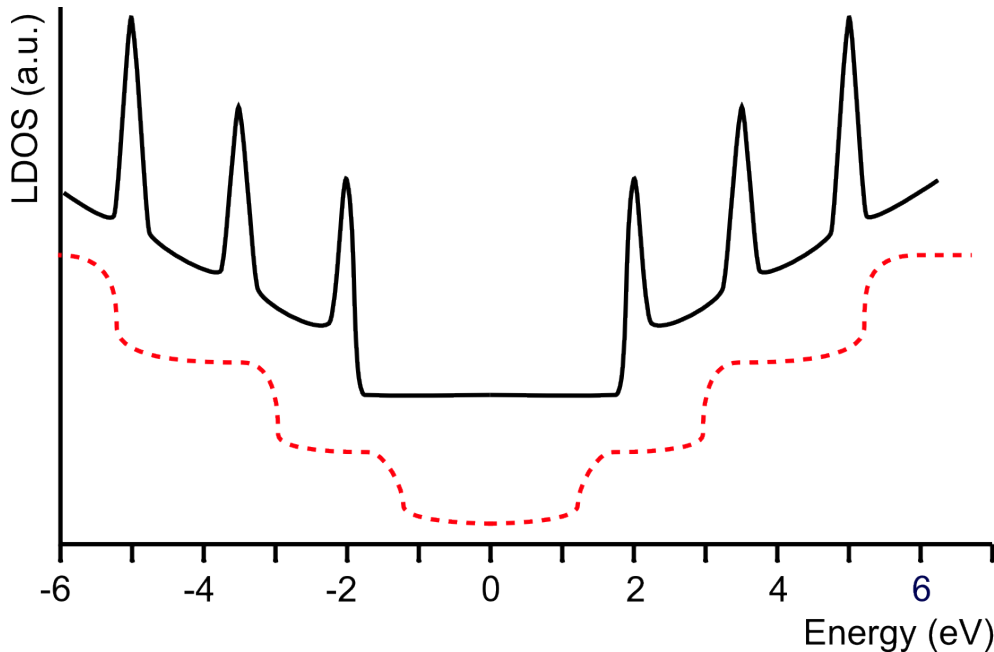


Figure 3.5: Schematic depiction of the LDOS vs. energy for a 2-dimensional electron gas and an individual quantum dot. The 2DEG increases stepwise whereas the QD shows sharp, single-level resonances.

A particularly interesting supercrystal geometry is the honeycomb structure. The lattice has a trigonal symmetry of PbSe nanocrystals which are oriented into a graphene-like lattice. It is important to note that the properties of graphene arise from the periodic potential imposed by the honeycomb lattice. Apart from the remarkable mechanical properties of graphene, its electronic properties are widely investigated, both in fundamental and more applied studies [18; 19; 20]. The valence and conduction band of graphene touch at the  $K$  and  $K'$  points (hence graphene is a semimetal). As a striking difference with conventional (semi-)conductors, graphene does not show a parabolic, but a linear dispersion around the Fermi-level ( $E_f$ ). Similar to photons, which also have a linear dispersion, the electrons with an energy close to  $E_f$  have an effective mass of zero, i.e. they behave like Dirac-fermions. This has many consequences, for instance, such carriers show reduced backscattering on electrostatic defects. As a result the mobility of the charge carriers in graphene is extremely high ( $20 \text{ m}^2\text{V}^{-1}\text{s}^{-1}$ ) [21], offering the prospect of ballistic transport.

As all the before mentioned remarkable properties only arise from the honeycomb symmetry of the lattice, the idea of the honeycomb supercrystal having these remarkable properties as

well popped up. Recently, a theoretical study by Efterpi et. al. (see reference [17]) showed that indeed the linear dispersion around the  $K$  and  $K'$  points is conserved for both the graphene and silicene analogue of the supercrystal (i.e. Dirac bands form) when they are made out of CdSe NCs. PbSe supercrystals have been calculated as well, but as their electronic structure is so complicated for the nanocrystals alone (due to intervalley coupling, band hybridization, etc.), the true understanding of the formed bands is difficult.

The predicted collective properties of both the graphene and silicene CdSe superlattices are summarized below;

- Both the graphene and silicene type lattice form 1S and 1P Dirac bands in the conduction states at the  $K$  and  $K'$  points. These are separated by about 200 meV. In graphene-type superlattices, these bands are connected just at the  $K$  and  $K'$  points of the Brillouin zone where the dispersion is linear (Dirac points). The 1P Dirac bands are very dispersive when compared to the 1S Dirac bands. The presence of Dirac points at two different energies is remarkable and has not been found in any other solid-state system. These bands can be understood when describing the CdSe supercrystal electronic states by one 1S envelope wavefunction and three 1P excited state envelope wavefunctions. In the silicene type lattice the gap between the two Dirac 1S bands can be opened and closed depending on the applied electric field. This gap arises from the absence of mirror symmetry with respect to the (111) contact facet.
- Both the graphene and silicene type superlattice form dispersionless 1P bands. These bands arise from the destructive interference of the electron waves in the honeycomb geometry. This band could give rise to very high conducting states (which we should be able to observe in STS), since these bands should have infinite capacitance theoretically.
- A peculiar property of the honeycomb lattice is its wavefunction chirality (or handedness), which basically means that the direction along which an electron propagates and the amplitude of its wave function are not independent. This is reflected in the pseudo-spin of the honeycomb lattice, associated with different A and B subpositions within the lattice. Due to this chirality the electrons experience less backscattering on electrostatic defects, which allows for ballistic transport.
- Another remarkable feature, relevant for applications in spintronics, is the spin-orbit coupling in the graphene superlattice (approximately  $50 \mu\text{eV}$ ). This spin-orbit coupling arises from Rashba/Dresselhaus interactions, which are induced by the absence of inversion symmetry and confinement in the superlattice [22].

## Chapter 4

# Observing the nano - Scanning Probe Microspectroscopy

“We see past time in a telescope and present time in a microscope. Hence the apparent enormities of the present.” - V. Hugo

The supercrystals described in the previous chapters and investigated throughout this thesis are in the nanometer size regime. As we cannot observe them with diffraction limited microscopy, such as conventional light microscopy or confocal microscopy, other ways of imaging these particles have to be used. Electron microscopy is widely applied in the nanomaterials field, but has no way of characterizing the electronic properties simultaneously with imaging on the local scale yet. A solution is given by scanning probe microscopy. Having the ability to both probe the geometric and electronic structure at the same time, scanning tunneling microscopy holds the key to unraveling our structures' fascinating geometry and electronics. This chapter describes the various aspects of scanning tunneling microscopy and spectroscopy, which is by far the most applied technique during the research described in this thesis.

## 4.1 Introduction - a short history of nearly everything

At the end of the nineteen seventies two scientists at the IBM Research Laboratory in Zurich, Gerd Binnig and Heinrich Rohrer, were interested in measuring the properties of thin films on a small scale (100 Å). They decided to use a positionable metal tip to act as one electrode and electrically wire this to the substrate. Realizing that they could not only probe the electronic structure, but also move the metal tip over the substrate to measure its topography, the scanning tunneling microscope (STM) was born [23]. In honor of this astounding achievement, they got the 1986 Nobel prize in physics, shared with Ernst Ruska who developed the first electron microscope.

Since its invention numerous adaptations and improvements were made in the field. One of the biggest drawbacks of the STM is that it cannot measure non-conducting substrates. A solution was found in the atomic force microscope (AFM) [24], which uses the force between the tip and a sample as a feedback signal rather than the current (also developed by Binnig, Quate and Gerber). Using both techniques simultaneously is nowadays possible with the invention of the qPlus<sup>TM</sup> sensor [25]. With the possibility of resolving atoms down to carbon and hydrogen in single molecules nowadays [26], true nanoscale engineering, or rather true atomic engineering, will flourish in the coming decades.

## 4.2 Quantum tunneling

The basis of the feedback in STM is a small current flowing from the tip to the sample or vice versa. Using classical mechanics, however, the nature of this current cannot be understood [27]. It was not until the mid 1920s that this phenomenon was described using the newly developed theory of quantum mechanics. The description of tunneling was first applied to explain the photoelectric effect and has since achieved many more successes, amongst which explaining nuclear decay [28].

A particle, or rather a particle's wavefunction, cannot penetrate an infinite potential well. When we trap the wavefunction between two of these wells, we end up with the well known particle-in-a-box problem. When we lower the potential well to a finite height, the wavefunction will decay exponentially and the probability that a particle appears on the other side becomes finite. The electron inside the potential well satisfies the Schrödinger equation;

$$\left[-\frac{\hbar^2}{2m} \frac{\partial^2}{\partial z^2} + U_a\right]\psi_u = E_u \psi_u \quad (4.1)$$

and has solutions of the form  $\psi(z) = \psi(0)e^{\pm ikz}$ , with  $k = \frac{\sqrt{2m(E-V)}}{\hbar}$  being the wavevector of the electron. Inside the potential barrier the wavefunction is decaying exponentially with  $\psi(z) = \psi(0)e^{\pm \kappa z}$  (the + and - indicate the motion of the electron in the +z or -z direction), where  $\kappa = \frac{\sqrt{2m(V-E)}}{\hbar}$  (note the difference between  $k$  and  $\kappa$ ). This 'electron spilling' out of the confined geometry is the basis of tunneling and many other effects, such as the presence of surface states.

Now for describing tunneling in the most general case; metal-vacuum-metal. One of the most basic concepts necessary is the work function  $\phi$  of a material, which is defined as the energy required to move an electron from the highest occupied energy state to the vacuum level. Taking the vacuum as reference we can define the Fermi energy as  $E_f = -\phi$ . When we apply a bias between the tip and the sample electrons can tunnel from tip to sample and

*vice versa* depending on the bias polarity. We can define a transmission coefficient  $T$  which is the ratio of the probability of finding an electron at a distance  $z$  from a reference position (e.g. the tip);

$$T = \frac{p(z=z)}{p(z=0)} = e^{-2\kappa z} \quad (4.2)$$

Here  $\kappa = \frac{\sqrt{2m\phi}}{\hbar}$  and is a decay constant of an energy state near the Fermi level. When  $z$  approaches the average atomic diameter the two outermost atoms of the tip and sample touch each other and the conduction for metals approaches the quantum of conductance  $G_0 = \frac{e^2}{\pi\hbar} \approx 77.5 \mu S$

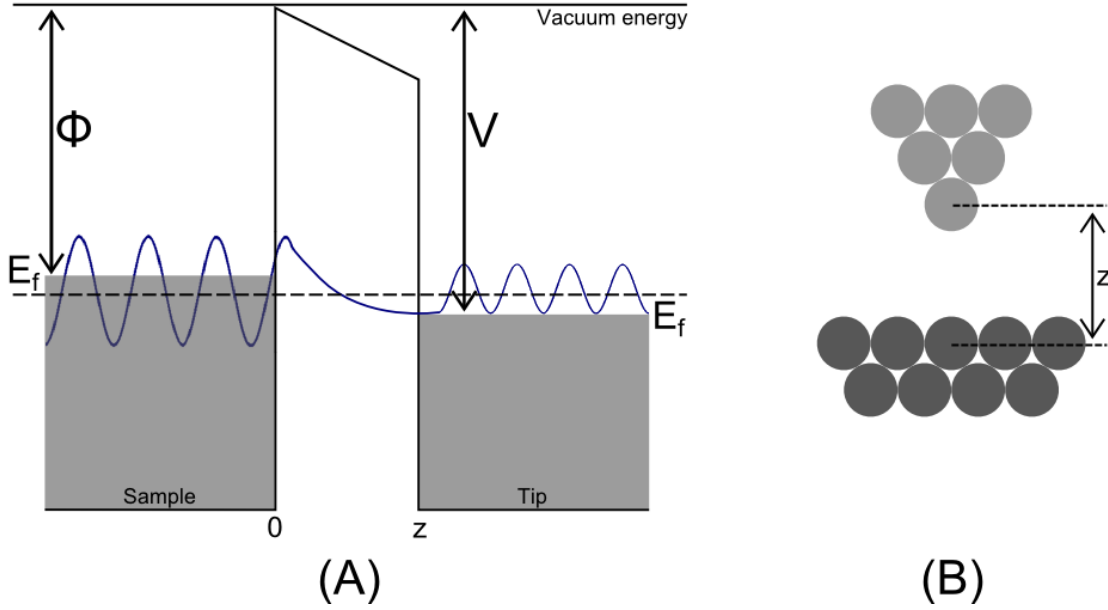


Figure 4.1: (A) Schematic of a metal-vacuum-metal tunnel junction. The top of the grey boxes indicate the Fermi levels of the tip and the sample and  $\phi$  is the sample workfunction. (B) Side view of the tip-sample tunnel junction. When  $z$  equals the atomic diameter (i.e. when the outermost atom of the tip touches an atom of the sample) a quantum point contact is established.

The following section deals with tunneling in a more rigorous manner, namely Bardeen's theory of tunneling in one dimension, which provided a solid basis for the interpretation of tunneling spectra [29; 30].

#### 4.2.1 Bardeen theory of tunneling

The tunneling phenomenon in STM is most widely described by the Bardeen theory, which basically is a time dependent perturbation on the 'regular' tunneling problem. We start with two electrodes,  $A$  and  $B$ , which are separated by a large distance. Now we can write the wavefunction of the free electrode  $A$  as;

$$i\hbar \frac{\partial \Psi}{\partial t} = \left[ -\frac{\hbar^2}{2m} \frac{\partial^2}{\partial z^2} + U_a \right] \Psi$$

where  $U_a$  is the function describing the potential landscape of electrode  $A$ . We can separate the time dependent and time-independent parts of this problem;

$$\Psi = \psi_u e^{-\frac{iE_u t}{\hbar}} \quad (4.4)$$

where the energy eigenvalues obey;

$$\left[-\frac{\hbar^2}{2m} \frac{\partial^2}{\partial z^2} + U_a\right] \psi_u = E_u \psi_u \quad (4.5)$$

Similar equations can be set up for electrode B, where we define its spatial wavefunction as  $\chi_v$ . At this large distance, both wavefunctions will decay exponentially in the barrier. As we bring the electrodes closer, the wavefunctions will start to overlap significantly and we can write the Schrödinger equation of the combined electrodes;

$$i\hbar \frac{\partial \Psi}{\partial t} = \left[-\frac{\hbar^2}{2m} \frac{\partial^2}{\partial z^2} + U_a + U_b\right] \Psi$$

What can be seen now is that a state located at electrode A,  $\psi_u$ , can transfer to electrode B. This means we can write the total wavefunction as;

$$\Psi = \psi_u e^{-\frac{iE_u t}{\hbar}} + \sum_{v=1}^{\infty} c_v(t) \chi_v e^{-\frac{iE_v t}{\hbar}} \quad (4.7)$$

The coefficients  $c_v(t)$ , which can be regarded as the amplitude of the  $v$ th state of electrode B at time  $t$ , can be determined by equation 4.5 with the boundary condition that  $c_v(0) = 0$ . As neither  $\psi_u$  and  $\chi_v$  are eigenfunctions of the same Hamiltonian, we need to make an assumption. A basic approximation in this theory is that both wavefunctions are approximately orthogonal;

$$\int \psi_u^* \chi_v d^3 \mathbf{r} \approx 0 \quad (4.8)$$

By inserting equation 4.7 into equation 4.3 and neglecting the infinitesimal second term, we obtain;

$$i\hbar \frac{dc_v(t)}{dt} = \int \psi_u^* U_b \chi_v d^3 \mathbf{r} e^{-\frac{i(E_u - E_v)t}{\hbar}} \quad (4.9)$$

By integrating the above expression over time, we can get an expression for the amplitude of the  $v$ th state of electrode B at time  $t$ ;

$$c_v(t) = M_{uv} \frac{e^{-i(E_u - E_v)t/\hbar} - 1}{E_u - E_v} \quad (4.10)$$

where we have defined the tunneling matrix element  $M_{uv}$  as  $\int \psi_u^* U_b \chi_v d^3 \mathbf{r}$ . Now we can give an expression of the probability of finding the  $v$ th state of electrode B at time  $t$ ;

$$p_{uv} \equiv |c_v(t)|^2 = |M_{uv}|^2 \frac{4 \sin^2[(E_u - E_v)t/2\hbar]}{(E_u - E_v)^2} \quad (4.11)$$

A lot can be deduced from the above equation. For example when  $E_u = E_v$  the equation reaches its maximum and for  $E_u \neq E_v$  the equation approaches zero rapidly. Hence we can state that in order for tunneling to occur, there must be a state  $v$  near in energy to state  $u$  which are both localized on different electrodes. By integrating equation 4.11 over the energy, we can introduce the density of states (DOS) of electrode B at energy  $E$ ,  $\rho_b(E)$ ;

$$p_{uv} = \frac{2\pi}{\hbar} |M_{uv}|^2 \rho_b(E) t \quad (4.12)$$

The same analogy can be applied for electrode  $A$ , where there is a DOS dependence  $\rho_a(E)$  and a bias  $V$  on the number of available states. If we now assume that the DOS near the Fermi energy does not vary significantly, the tunneling current is given by;

$$I = \frac{2\pi e^2}{\hbar} |M_{uv}|^2 \rho_a(E_f) \rho_b(E_f) V \quad (4.13)$$

As can be seen the magnitude of the current is determined by the DOS of both electrodes, i.e. the current is always affected by a convolution of both tip and sample DOS in STM experiments. If either the DOS of electrode  $A$  or  $B$  is zero (e.g. tip or sample DOS is zero as an analogy with STM), the total current will be zero.

### 4.2.2 Scanning Tunneling Spectroscopy

With STM we are often interested in determining the local density of states (LDOS), both at one particle/molecule and spatially. We can understand how to measure the LDOS by following Bardeen's theory. In the equation below, he assumed a Fermi-Dirac distribution of the electrons in both electrodes and a high energy resolution ( $k_b T < \Delta E$ );

$$I = \frac{4\pi e}{\hbar} \int_0^V \rho_a(E_f - V + \epsilon) \rho_b(E_f + \epsilon) |M_{uv}|^2 d\epsilon \quad (4.14)$$

If we now assume that the tunneling matrix element is constant in the energy range of interest and the tip DOS is constant, we can state that the derivative of the current with respect to the applied bias voltage is proportional to the LDOS of the sample at a certain energy (e.g.  $\frac{dI}{dV} \propto \rho_{sample}(E)$ ).

There are many more models to describe the features arising in STM and STS. One of the more applied methods in understanding and simulating STM images is the Tersoff-Hamann model, which finds its origin in Bardeen's theory of tunneling [31]. The derivation of this model assumes a spherically symmetric tip wavefunction (S-wave tip) and shows that the tunneling matrix element is equal to the value of the sample wavefunction at the center of curvature of the tip. However, the model gets increasingly more complicated when the tip is passivated with e.g. a CO molecule, which has a P-wave character, or when the tip wavefunction becomes more hybrid [32]. A comprehensive derivation of this model goes beyond the scope of this thesis.

### 4.3 STM/STS on quantum dots and supercrystals

Quantum dot spectroscopy (and hence also spectroscopy on the supercrystals) forms yet another difficulty in interpreting the obtained features. The underlying cause is the formation of a second tunnel junction [13; 33; 34]. On regular clean metal surfaces, electrons or holes tunnel directly from the tip to the sample, hence there is only one tunnel process (i.e. there is only one potential barrier). However, when a dielectric object such as a QD is placed in the junction between the tip and the sample a second junction is formed. The charge carriers now have to tunnel from the tip to the object (tip-QD junction) followed by tunneling from the object to the substrate (QD-substrate junction); a so called double-barrier tunnel junction is formed (see figure 4.2).

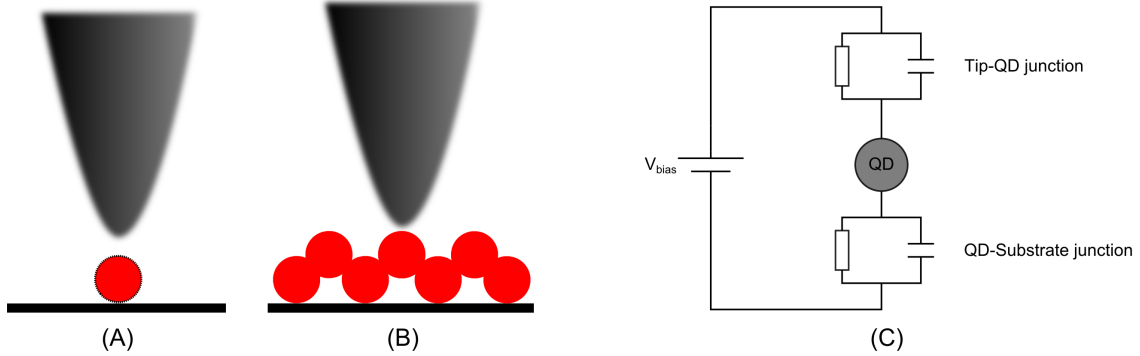


Figure 4.2: (A) Schematic representation of QDs inside a STM setup. (A) Single QD STM/STS, the presence of the QD forms a second tunneling junction, hence the term double barrier tunnel junction. (B) Supercrystal STM/STS, where the potential distribution is more complex. (C) Electric circuit of the DBTJ.

This placement of a relatively large (w.r.t. molecules) dielectric between the tip and the substrate has another consequence. The electric field between tip and substrate does not drop homogenously; the electrons do not experience the applied electric field everywhere over the tip-sample junction. As a consequence the scalebar in STS cannot be converted from V to eV directly, but needs to be multiplied with the so called lever arm  $\eta$ ;

$$\eta = \frac{V_{dot} - V_{tip}}{V_{bias}} \quad (4.15)$$

where  $\eta$  is the fraction of the bias voltage that drops between the tip and the QD,  $V_{tip}$  is the potential of the tip,  $V_{dot}$  the potential at the center of the QD and  $V_{bias}$  is the total applied bias between the tip and the substrate. The distribution can be calculated by solving the Poisson equation (or rather the Laplace equation) over the tip-dot-substrate system;

$$\nabla^2 V = \frac{-\rho}{\epsilon_0} = 0 \quad (4.16)$$

Where  $V$  is the electric potential and  $\rho$  is the charge density. Using a finite element simulation (Comsol Multiphysics, version 4.1), the Laplace equation was solved for a PbSe QD (modelled as a dielectric sphere) with an organic capping layer, where the substrate is connected to ground (0 V) and the tip is given a potential of 1V;

It has been found that for lower dielectric materials ( $\epsilon < 50$ ), such as CdSe, the potential distribution varies more over the QD resulting in a stronger dependence on  $\eta$  [35]. For the supercrystals in this thesis, for which electronic measurements have been done, this has to be taken into account when converting the energy scale in the spectroscopy experiments. Also the

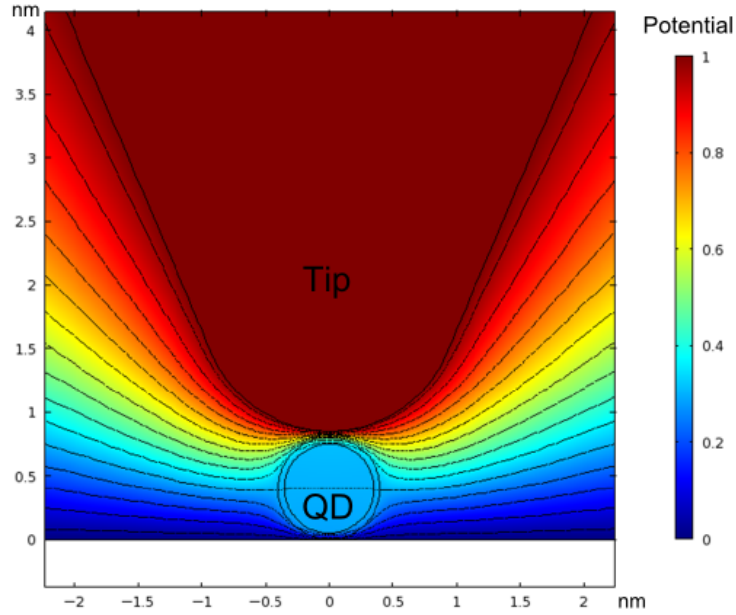


Figure 4.3: Potential drop over the DBTJ by solving the Laplace equation for the electric potential. The 5.0 nm PbSe QD is modelled as a dielectric sphere with  $\epsilon = 227$  capped with an organic layer of 0.5 nm (realistic for oleic acid) with  $\epsilon = 2.5$

fact that the QD gets charged (i.e. the QD is polarized) will result in an 'energy penalty' for which corrections have to be made.

As a last remark the tunneling spectroscopy on QDs and supercrystals is based on resonant tunneling of the electrons and holes in and out of the QD. However, the spectra are very sensitive to whether an electron or hole tunnels through an electrons and hence experience no coulombic interactions with other electrons and holes present. The first is called the shell tunneling regime, where the spectrum resembles the electronic LDOS of the QD or supercrystal. The latter is called the shell filling regime, where the spectrum contains many more features, arising from electron-electron interactions. This regime can be reached by increasing the current setpoint or decreasing the tip-sample distance. Adequate verification of the regime in which is measured is necessary in order to give a clear interpretation of the obtained spectral features.

## Chapter 5

# Experimental

"If your experiment needs statistics, you ought to have done a better experiment" -  
E. Rutherford

This chapter deals with the experimental details of the performed research. First the preparation of the supercrystals is elaborated on. It briefly deals with the synthesis of the NCs. This is followed by synthesis of the supercrystals and the environmental (in)stability of the preparation method (i.e. the sensitivity of the sample preparation to the glovebox environment). Next the STM/AFM setup which was used is discussed, followed by a brief introduction to electron microscopy and electron tomography.

## 5.1 Nanocrystal and supercrystal preparation

The PbSe nanocubes were synthesized by W.H. Evers according to a method described by Steckel et. al. [36]. This is a hot injection method. The major advantage of this method is that the nucleation and growth stage of the NCs are separated, resulting in a low NC polydispersity. The synthesis was performed in a water and air free environment.

The oriented attachment was performed as described in [7]. A glass vial (with an inner diameter of 10 mm) was filled with 1 mL of ethylene glycol which was subsequently heated to 30°C. Then 50  $\mu\text{L}$  of the nanocrystal suspension with an initial concentration of  $\sim 11.3 \times 10^{-7}$  mol/L was placed on top of the ethylene glycol (EG) solution. The ethylene glycol serves as an immiscible liquid substrate for the nanocrystal solution. Then the NC solvent was allowed to evaporate after which a sample was scooped from the ethylene glycol layer with the appropriate substrate (HOPG or TEM-grids). All experiments were performed in a nitrogen purged glove box.

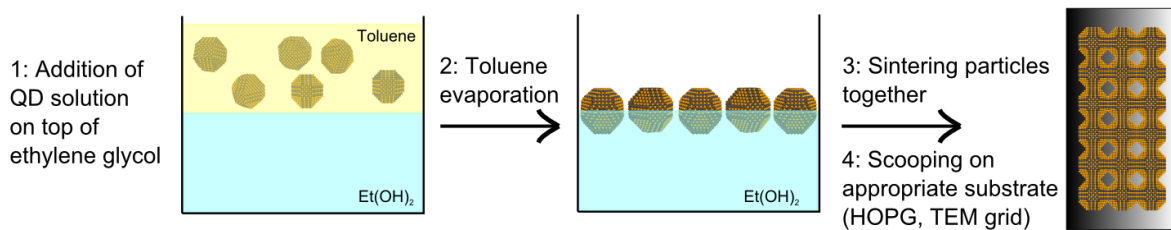


Figure 5.1: Schematic of sample preparation. The preparation is composed out of four stages. In the first stage the QD dispersion is added on top of the ethylene glycol (1). Next the solvent of the QDs is allowed to evaporate, resulting in adsorption of the QDs on the liquid-air interface (2). The QDs are sintered together at a temperature of 30°C (3) after which the formed supercrystal is scooped of the ethylene glycol with an appropriate substrate(4).

Another advantage of using ethylene glycol is the partial solubility of the oleic acid capping ligands. The nanocrystals are, depending on concentration and temperature, stripped of their ligands from specific crystal facets. As the facets are now exposed, they can react and form atomically coherent bonds to create the supercrystals.

## 5.2 Scanning Probe Microscopy setup - the 'beast in the basement'

The results in this thesis are obtained using an Omicron Nanotechnology SPM setup. The setup consist of three main chambers; the preparation chamber, the analysis chamber with the variable temperature (VT) STM, and the low temperature (LT) STM/AFM setup. The whole system resides under ultrahigh vacuum (UHV) conditions with a base pressure of  $< 1 \times 10^{-10}$  mbar. Moreover, due to vibrational coupling of the STM to its surroundings, the whole setup was recently placed on top of active damping legs. This damping system uses piezo driven springs to actively compensate for vibrations, lowering the noise level to  $\approx 10$  pm.

### 5.2.1 Preparation chamber

The preparation chamber consists out of two compartments. The first compartment is a fast entry lock, through which samples can be inserted into the system via manipulator arms which can be manually controlled. The preparation chamber has a heater arm, on which which the samples can be annealed via resistive heating. Furthermore the chamber contains a quartz microbalance and a sputter setup. A recent upgrade has been made in order to install an infrared heat sensor. When a material is heated, it starts to emit black body radiation, the wavelength and intensity of which depend on temperature. Various quartz view ports were replaced with ZnSe windows, as these have a better transmission in the infrared region of the spectrum.

### 5.2.2 Analysis chamber - VT SPM

The analysis chamber has one large manipulator arm, through which samples can be transferred from the preparation chamber to the analysis chamber. As in the preparation chamber, the arm can be heated as well for annealing purposes. If the sample needs to be inserted into the LT compartment, a wobble stick can be used to grasp the base plate. The analysis chamber also has a tip-preparation tool, allowing for the removal of oxygen layers on the tip apex. The actual VT microscope has the possibility to do both STM and AFM. The AFM is operated via laser deflection. Finally there is also a carousel, which allows for up to 12 samples to be stored in vacuum. The microscopy stage is mounted on an Eddy current damping system in order to reduce vibrational coupling with the environment.

### 5.2.3 LT SPM - Combined STM/AFM setup

The LT-STM used mostly for the STS experiments can operate at three temperatures; room temperature, 77K (LN<sub>2</sub>) and 4K (LHe). A low temperature is required for a number of reasons. First of all the drift during measurements is significantly reduced as tip and sample both have the same (low) temperature. Moreover, the molecules are all in their ground state configuration and the energy resolution during spectroscopy is increased significantly. The measurement stage is mounted on an Eddy current damping system in order to reduce vibrational coupling even more in experiments. The conductance signal is recorded using a lock-in amplifier. By sending a modulation voltage  $\sin(\omega t)V_m$  over the applied bias one is able to directly measure the gradient of the current w.r.t. the applied bias, hence the LDOS. The current can now be expanded as a power series w.r.t. the applied modulation voltage;

$$I_t(V, V_m \sin(\omega t)) = I_0 + V_m \sin(\omega t) \frac{dI_t(V)}{dV} + V^2 \sin^2(\omega t) \frac{d^2 I_t(V)}{dV^2} + \dots \quad (5.1)$$

where  $\omega$  is the modulation frequency,  $V_m$  is the amplitude of the modulation voltage,  $V$  is the applied bias and  $I_0$  is the obtained current without the modulation signal. Higher order terms, such as the inelastic tunneling current, are neglected in the above equation. The major advantage of recording the  $\frac{dI}{dV}$  signal in this fashion is that the signal to noise ratio is increased tremendously w.r.t. taking the numerical derivative of  $I - V$  traces. However, the  $I - V$  curves, which are recorded simultaneously, should always be checked for tip changes, artefacts etc.. Moreover these can be used to fit the conductance curves obtained with the lock-in amplifier to get quantitative information from the spectra.

### 5.3 Electron microscopy

Some electron microscopy measurements were performed on the obtained supercrystals, mostly to verify sample quality before inserting them into the STM. This was usually done in transmission mode where monochromatic electrons are fired onto the sample which was placed onto a Cu-TEM grid coated with a formvar polymer layer. The transmitted electrons are collected and the intensity on each pixel is integrated over a certain timeframe. As the number of electrons on an element increases with increasing atomic number  $Z$ , the transmission probability decreases; the amount of electron-electron scattering increases for higher  $Z$  elements. The data obtained are so called bright-field images.

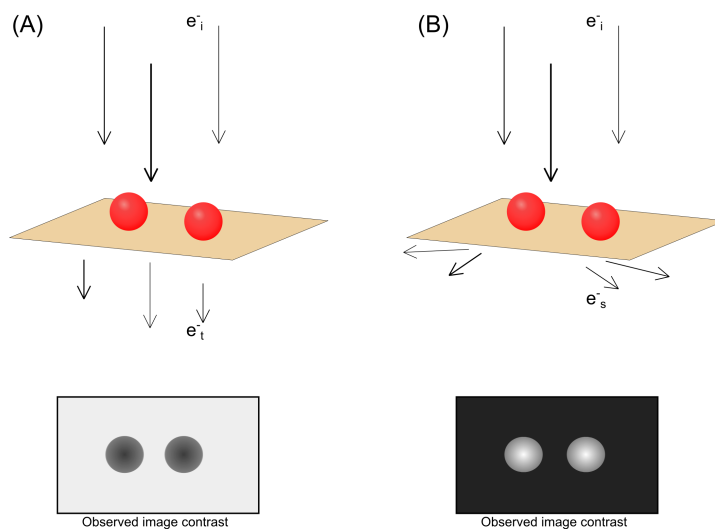


Figure 5.2: Schematic representation of imaging modes in electron microscopy. (A) Normal transmission mode, where the electrons are detected along the incident beam direction. (B) (High angle) annular mode, where the scattered electrons are detected. Note the inverted image contrast between the two detection modes.

The second mode for collecting data is by measuring scattered electrons. As heavier elements (larger  $Z$ ) have more electrons, they scatter more of the incident beam. This provides a second way of data acquisition, mostly known as dark-field measurements. To increase resolution even further one can go to very high scattering angles, in so called (high angle) annular dark field (HAADF) measurements. Here an aperture is placed in the forward direction, allowing only the scattered electrons to pass and blocking the main beam. The main beam then can be used to collect an electron energy loss spectrum (EELS), allowing for imaging and spectroscopy simultaneously.

Most measurements were performed on the TECNAI 10 and TECNAI 12. Specifications of these microscopes are given below;

| Specification                     | Tecnai 10       | Tecnai 12            |
|-----------------------------------|-----------------|----------------------|
| Objective lens                    | TWIN (standard) | BioTWIN (long focal) |
| Point resolution (nm)             | 0.34            | 0.49                 |
| Line resolution (nm)              | 0.20            | 0.34                 |
| Cs objective (mm)                 | 2.0             | 6.3                  |
| Cc objective (mm)                 | 2.0             | 5.0                  |
| Focal length (mm)                 | 2.7             | 6.1                  |
| Minimum focus step (nm)           | 3.0             | 3.0                  |
| Maximum eucentric tilt            | $\pm 70^\circ$  | $\pm 80^\circ$       |
| TEM magnification                 | 35x - 700kx     | 20x - 700kx          |
| SA diffraction camera length (mm) | 35 - 2300       | 68 - 13500           |
| Diffraction angle                 | $\pm 10^\circ$  | $\pm 10^\circ$       |
| STEM magnification                | 70x - 300kx     | 50x - 300kx          |

## 5.4 Electron tomography

In transmission microscopy one obtains a two-dimensional projection of a three-dimensional object. Imaging the object over different consecutive angles, acquiring various 2D images, allows for creating a 3D data stack. This data stack can be used to create a 3D reconstruction of the object. This technique is called tomography and it is used to elucidate the geometry of the honeycomb supercrystal.

Nowadays, the Project-Slice theorem is used most in electron tomography [37; 38; 39; 40]. Here a 2D Fourier transform (FT) is taken from an image, which corresponds to a central slice through the 3D FT of the object. By acquiring images under different tilt angles, hence obtaining different slices in Fourier space, one can use an inverse Fourier transform (IFT) to reconstruct the 3D object. This process is illustrated in the figure below;

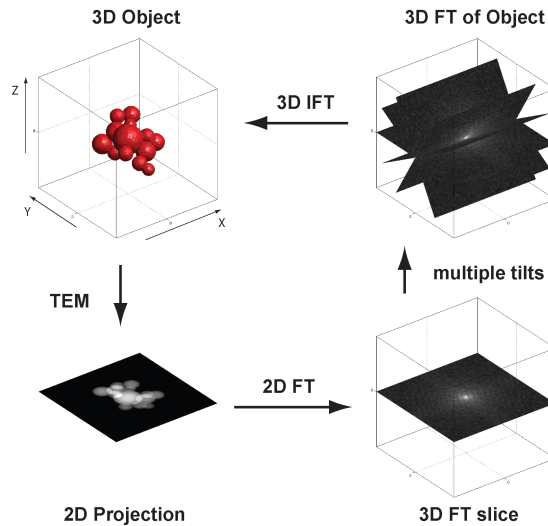


Figure 5.3: Schematic representation of the electron tomographic reconstruction scheme using the Projection-Slice theorem. Image taken from reference [38]

## Chapter 6

# Results

"No one is so brave that he is not disturbed by something unexpected." - Julius Caesar

The results obtained over the past one-and-a-half years are presented in this chapter. We will first deal with the supercrystal synthesis and its stability. It will become clear that a wide variety of supercrystals can be obtained by changing simple synthesis parameters, and that the oriented attachment can be controllably quenched by addition of extra ligands. Each obtained supercrystal (linear, square and honeycomb) will be discussed separately in detail. An emphasis will be on the honeycomb lattice as this is expected to give rise to interesting electronic band structures and properties. Its rather peculiar and unexpected geometric structure will be elucidated by a combination of STM, EM and electron tomography. Finally the first spectroscopy experiments will be presented and discussed.

## 6.1 Supercrystal synthesis

The supercrystals are prepared as described in chapter five. By varying the NC concentration from lower ( $7 \times 10^{-7} \text{ mol/L}$ ) towards higher ( $30 \times 10^{-7} \text{ mol/L}$ ) concentrations, supercrystals with linear, honeycomb and square geometry are obtained respectively. The obtained supercrystals are displayed in an overview in the figure below.

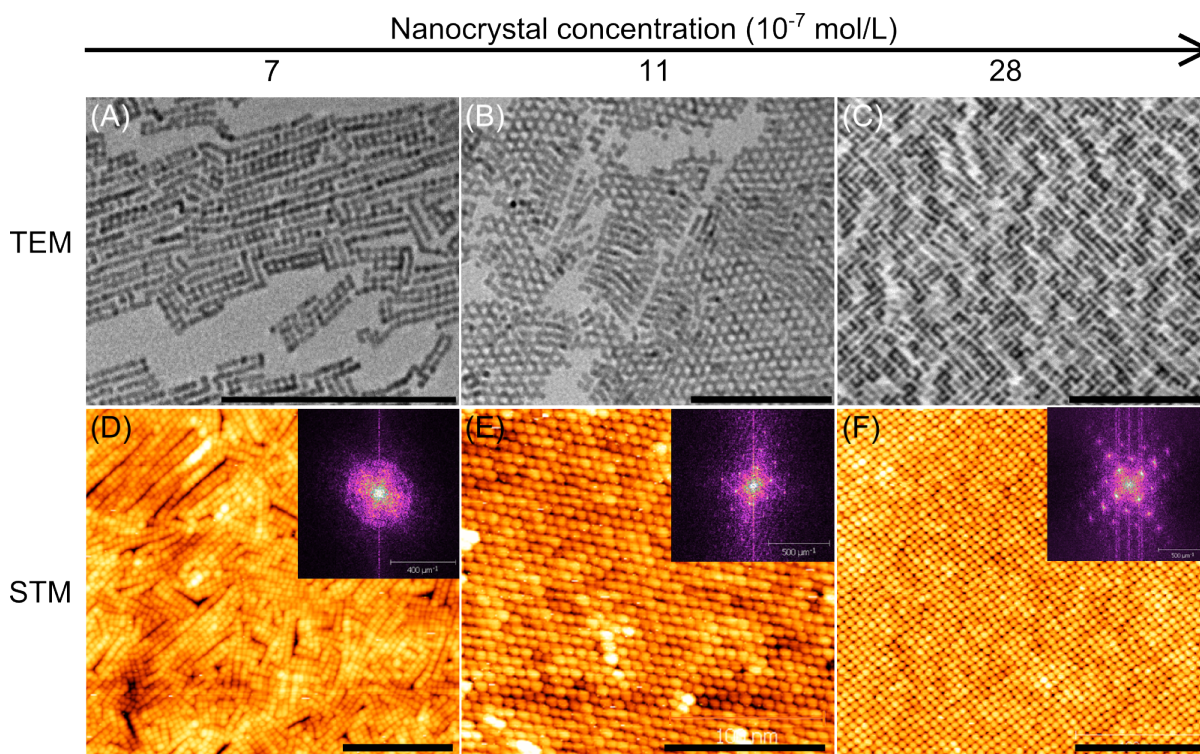


Figure 6.1: Overview of the obtained supercrystals. (A-C) are obtained by TEM, (D-F) are obtained by STM, with the insets being the Fast Fourier transform (FFT) of the image, showing the long range order of the supercrystal. Figures (A) and (D) display the linear structures, which attach via the  $\{100\}$  facets. Figures (B) and (E) display the honeycomb geometry, which is the most widely investigated structure in this thesis. Attachment occurs via the  $\{111\}$  facets (see section on the honeycomb geometry for discussion of facet attachment in these supercrystals). Figures (C) and (F) display the square sheets which attach via the  $\{100\}$  facets. All black scalebars represent 100 nm.

Figure 6.1 shows the obtained atomically coherent supercrystals. At a concentration of  $7 \times 10^{-7} \text{ mol/L}$  of the PbSe NC dispersion the attachment results in linear structures, as seen in figure 6.1 (A) and (D). The attachment likely occurs via the  $\{100\}$  facets, although other experiments have shown buckling of the linear chains (which would result from  $\{110\}$  attachment). More information can be found in the section on the linear supercrystals.

At a slightly elevated concentration of the NC dispersion,  $11 \times 10^{-7} \text{ mol/L}$ , a completely different supercrystal is obtained with a honeycomb geometry as can be seen in figure 6.1 (B) and (E).

The honeycomb supercrystal can form through attachment via two different routes;

- Attachment via the  $\{110\}$  facets, resulting in a flat, graphene-like supercrystal.
- Attachment via the  $\{111\}$  facets, resulting in a buckled, silicene-like supercrystal, where every next nearest neighbour NC is in the same height plane.

The attachment will be discussed in more detail in the honeycomb supercrystal section, where we will elucidate that the attachment occurs via the  $\{111\}$  planes, resulting in a silicene type supercrystal.

At even higher concentrations of the NC dispersion,  $30 \times 10^{-7}$  mol/L, square sheets are formed, as can be seen in figure nr (C) and (F). Attachment occurs via the  $\{100\}$  planes, resulting in flat 2D supercrystals with a square geometry. More information will be given in the section on these supercrystals.

### 6.1.1 Synthesis stability

Throughout the research the reproducibility of the synthesis became questioned, as more and more samples which were obtained contained molten structures. The exact same synthesis procedure was repeated numerous times in a dedicated glovebox ( $N_2$  environment, used for oriented attachment experiments only), however different results were obtained over several experiments. We observed the formation of supercrystals, in which we are able to distinguish the individual NCs, but also molten crystals. In these molten crystals the individual NCs cannot be resolved anymore and no directionality in the supercrystal is observed. The melting can be explained by taking the stability of NC facets into account. In the dispersion, before attachment, the NCs are stabilized by their capping ligands, oleic acid (OA). Once the nanocrystals are injected on top of the EG, the OA also present in the NC dispersion can either stabilize the NCs or redissolve in the EG phase;  $OA_{NC} \rightarrow OA_{EG}$ . As we start from a non-equilibrium condition, with all the OA at the NC surface, some OA will dissolve in the EG phase. Once the NCs get stripped fully, the control over the attachment is lost and the atoms on the NC surface are free to diffuse during the sintering process, resulting in molten crystals.

To test the above stated hypothesis a new line of experiments was performed. An additional amount of OA was added to the EG phase to shift the equilibrium of the ligands towards capping the NC. One has to be careful not to add a too large excess of OA, as the oriented attachment can be quenched by complete blockade of all reactive facets. The results from these experiments are summarized in figure 6.2 on the next page. At very high OA concentration the oriented attachment is blocked, resulting self assembly of the PbSe NCs rather than oriented attachment. At an OA concentration of  $\approx 6 \times 10^{-8}$  to  $12 \times 10^{-8}$  mol/L the oriented attachment process is restored. At lower OA concentrations, ranging from  $\approx 1 \times 10^{-8}$  to  $3 \times 10^{-8}$  mol/L, the NCs were not passivated enough, resulting in melting of the structure. One would say that the problem is now solved, however, repeating the exact same experiments one week later resulted in only molten crystals again. This shows that the OA process is extremely sensitive to its environment; we only add one OA molecule per 10-20 PbSe NCs. For example, if the glovebox is used the day before for different experiments, also utilizing OA, the partial pressure of OA inside the glovebox is slightly elevated. As we only add a minute amount of OA to the experiments ourselves, one can appreciate the importance of the overall environment.

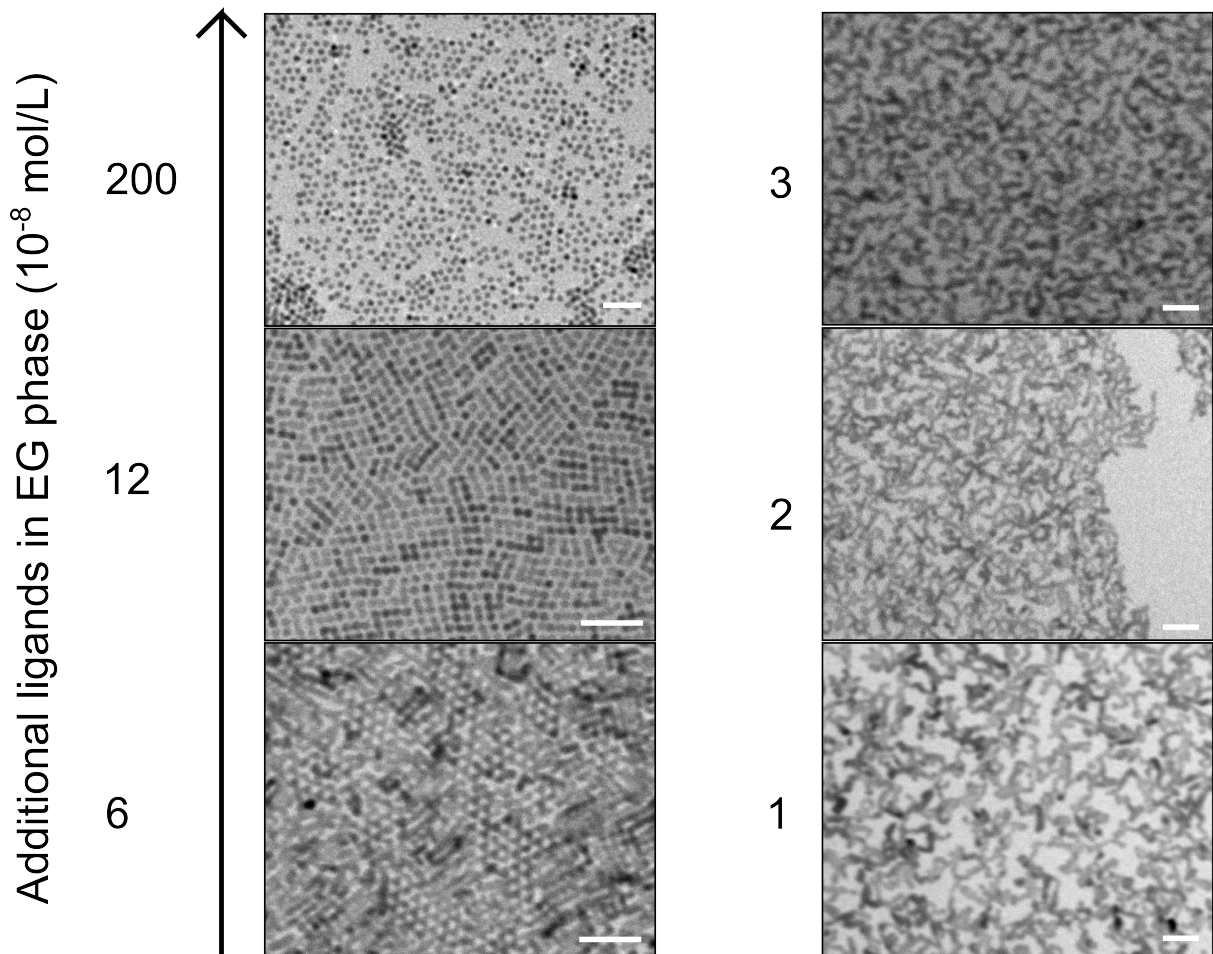


Figure 6.2: Phase diagram, showing the dependence of oriented attachment on the OA concentration in the EG phase. When little to no ligands are added, the crystals melt. Upon increasing the OA concentration the oriented attachment process is restored. Addition of a very large excess of OA to the EG phase quenches the attachment process; as the facets get fully passivated by ligands, the atomic attachment with neighbouring nanocrystals is blocked. Scalebars denote 100 nm.

Figure 6.3 shows several molten structures. (A) shows an overview of a sample containing molten structures. In less dense areas string-like structures are found as seen in (B). These are likely to originate from the linear supercrystals. In more dense areas a network of molten PbSe structures is found, as seen in (C). (D) shows an overview of another sample which contained molten structures. Note that on this sample also attached structures are seen (center of image shows a patch of honeycomb crystal). Throughout the rest of the sample a whole network of strings and wires was found, as seen in (E) and (F).

A detailed analysis has to be performed on the reproducibility of the supercrystal synthesis. Several attempts have already been made, by varying the OA concentration in the EG phase, in order to get a picture on what is the cause of the melting. We now believe that the amount of OA on the NCs is the key factor in melting. Another series of experiments, checking whether a decrease in the amount of EG (which should be the same as increasing the OA concentration) during the sample preparation, also influences the melting behaviour.

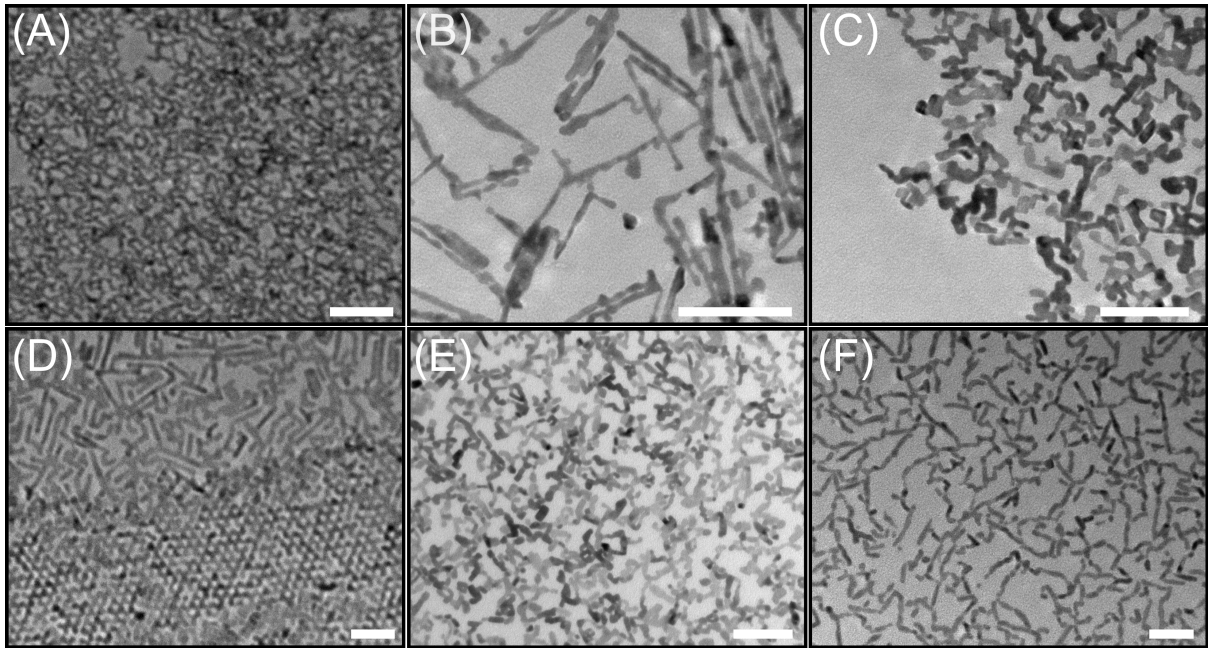


Figure 6.3: Various molten structures. Figures (A-C) are taken on the same sample, as are figures (D-F). Note that in figure D both the molten structures and the oriented attached supercrystals coexist. This is the only sample on which this was found. Many more samples containing molten structures were obtained. Scalebars denote 50 nm.

### 6.1.2 Stripping of surface capping - Meerwein's salt

A small detour was made into creating ligand free supercrystals. This was done by first forming the supercrystal, followed by short submergence into a solution containing meerwein's salt (MWS), which is a short name for the compound triethyloxonium tetrafluorborate. MWS is a trialkyl oxonium salt capable of mildly stripping PbSe nanocrystals from their OA capping layer. The procedure was performed by a slightly adapted scheme as reported in Rosen et. al. [41]; after the supercrystal synthesis and scooping onto a Cu TEM grid, the grid was submerged for 30 seconds in a 50 mM solution of MWS in EG. The TEM grid was left to dry in vacuum for one hour.

Figure 6.4 shows the results obtained by two attempts of removing the capping ligands. The sample in figure 6.4 (A) survived the submergence in the MWS solution, still showing the square supercrystal. However this is not a definite proof that the OA ligands are removed from the sample. The second sample, as shown in figure 6.4 (B) did not survive the treatment. There are two possible explanations for this sample. The first explanation is that we did not prepare the supercrystal and had molten structures to begin with. The second explanation is that the entire sample is etched away by the MWS solution. Further experiments on the removal of the OA layer are required in order to get a better understanding of the process. Full proof of the ligand removal can be given by IR-spectroscopy, probing the CH and CO stretching vibrations.

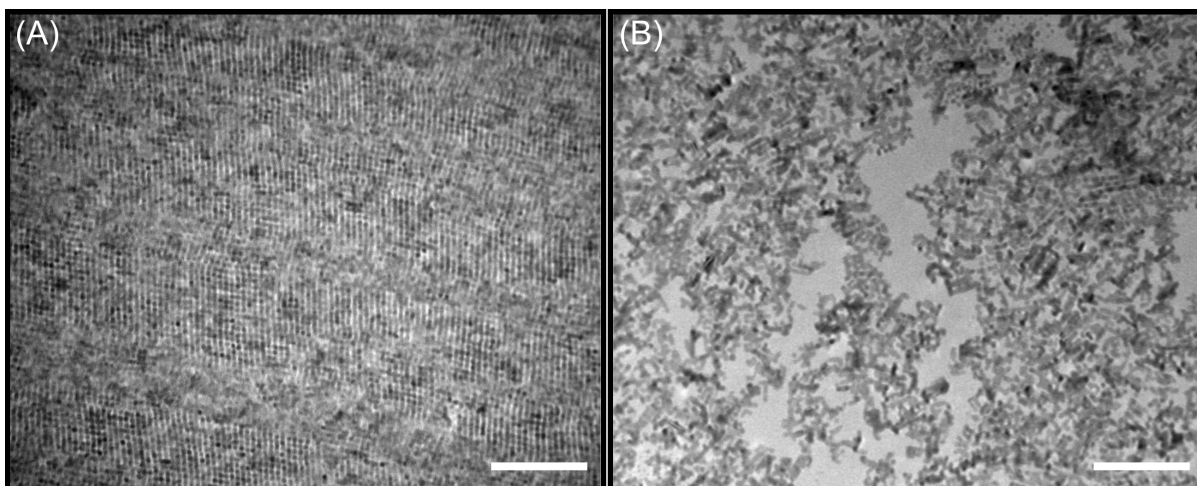


Figure 6.4: Two attempts on stripping the supercrystals from their capping layer. (A) shows an attempt in which the square sheets remained intact after stripping the OA. (B) shows a second sample, which was prepared in a similar fashion as (A), which is completely etched away by MWS. Scalebars denote 100 nm.

## 6.2 Linear supercrystals

Linear structures were obtained at the lowest concentration of the PbSe dispersion ( $7 \times 10^{-7}$  mol/L). The length of these structures varies from sample to sample. Especially when extra oleic acid is added, the chain length is decreased. This can be understood in terms of the amount of reactive, i.e. ligand free, facets.

Figure 6.5 shows a number of TEM images of the linear supercrystals, which have a rod-like geometry. (A) and (B) are images acquired from the same sample, which display chains that are longer than the chains shown in figure (C). The difference is that in the latter, additional OA was used. As more ligands populate the reactive facets, the growth of the structures is hampered, resulting in chains which are smaller in length.

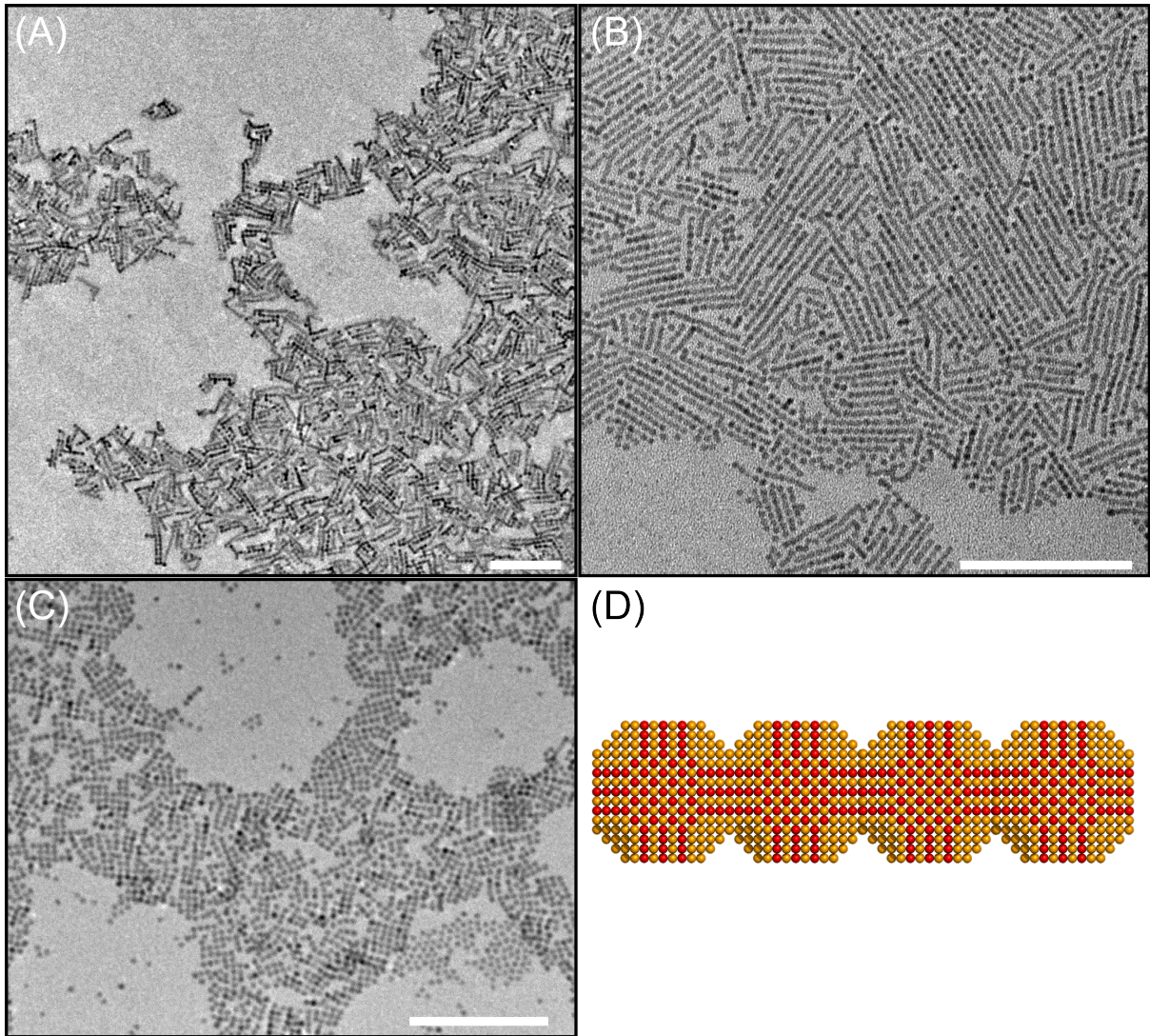


Figure 6.5: Several TEM images on linear supercrystals. (A) and (B) are taken on the same sample and both show overview images of the obtained structures. (C) also shows ribbons, but with  $20 \times 10^{-8}$  mol/L OA in the EG phase. (D) is the atomic model of the linear superstructures, showing the atomic attachment via the  $\{100\}$  facets. Scalebars denote 50 nm.

Figure 6.6 shows two large overview scans obtained in the VT-STM of PbSe linear supercrystals. Densely packed areas are obtained when scooping the crystals from solution, resulting in roughly a monolayer of linear supercrystals on top of the HOPG substrate. Large clusters are seen on both images, which are agglomerates of NCs. Scanning over the obtained structures goes with relative ease, even though the scansize and scanspeed are quite fast (approximately 250 nm/s) and the capping ligands are presumably not fully removed yet. This might be due to the relatively low current setpoint of only 5 pA, leading to a large tip-sample distance.

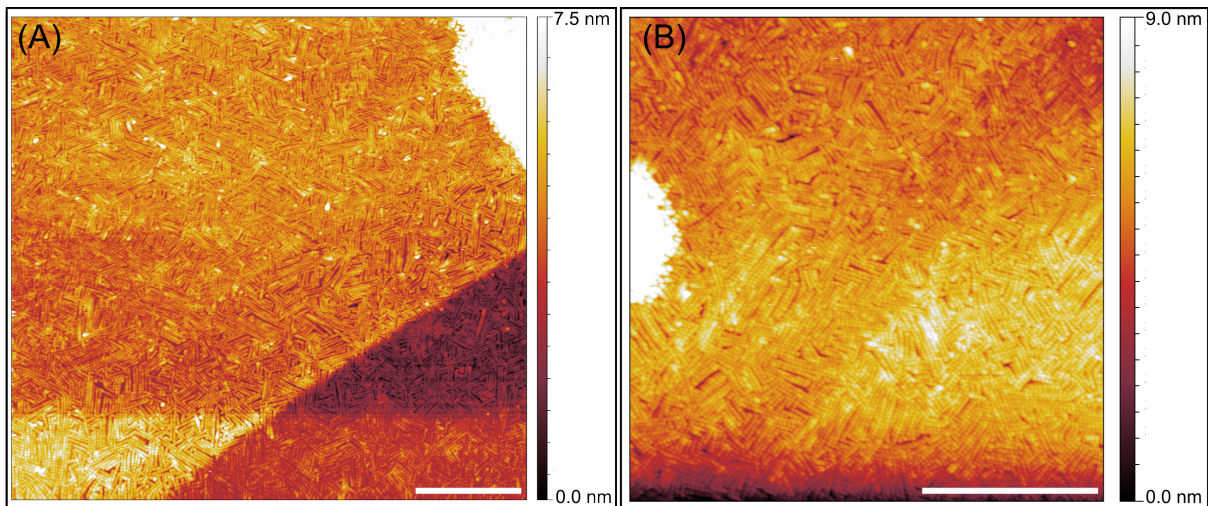


Figure 6.6: Figures (A) and (B) show large overview STM scans of linear supercrystals. Note the HOPG step edge running across the sample in the bottom part of image (A).  $V = 1.5\text{V}$ ,  $I = 5\text{ pA}$ . Scalebars denote 200 nm.

The figure below shows a zoom in of a small patch of linear supercrystals. As can be seen, individual NCs inside the chains can be resolved. The height profile, taken along the line shown in figure 6.7 (A), is shown in figure 6.7 (B). As can be seen, the NC corrugation inside the supercrystal is clearly distinguished over one linear chain. In order to determine the average particle size inside these chains, roughly 20 of these height profiles were obtained and 160 particles were detected. Using Matlab, the average minimum-to-minimum distance was determined for a large number of different scans and particles. Only intraparticle, i.e. within one linear supercrystal, line traces were used. The minimum-to-minimum distance was used as an indication for the average NC size inside the supercrystals, which is shown in figure 6.7 (C). The as obtained average NC size is  $5.9 \pm 0.9\text{ nm}$ . This average size of the NCs is in good correspondence with the obtained TEM particle size, which is 5.5 nm. The deviation cannot be explained by tip sample convolution, as the objects would be broadened, but the center-to-center distance should not change.

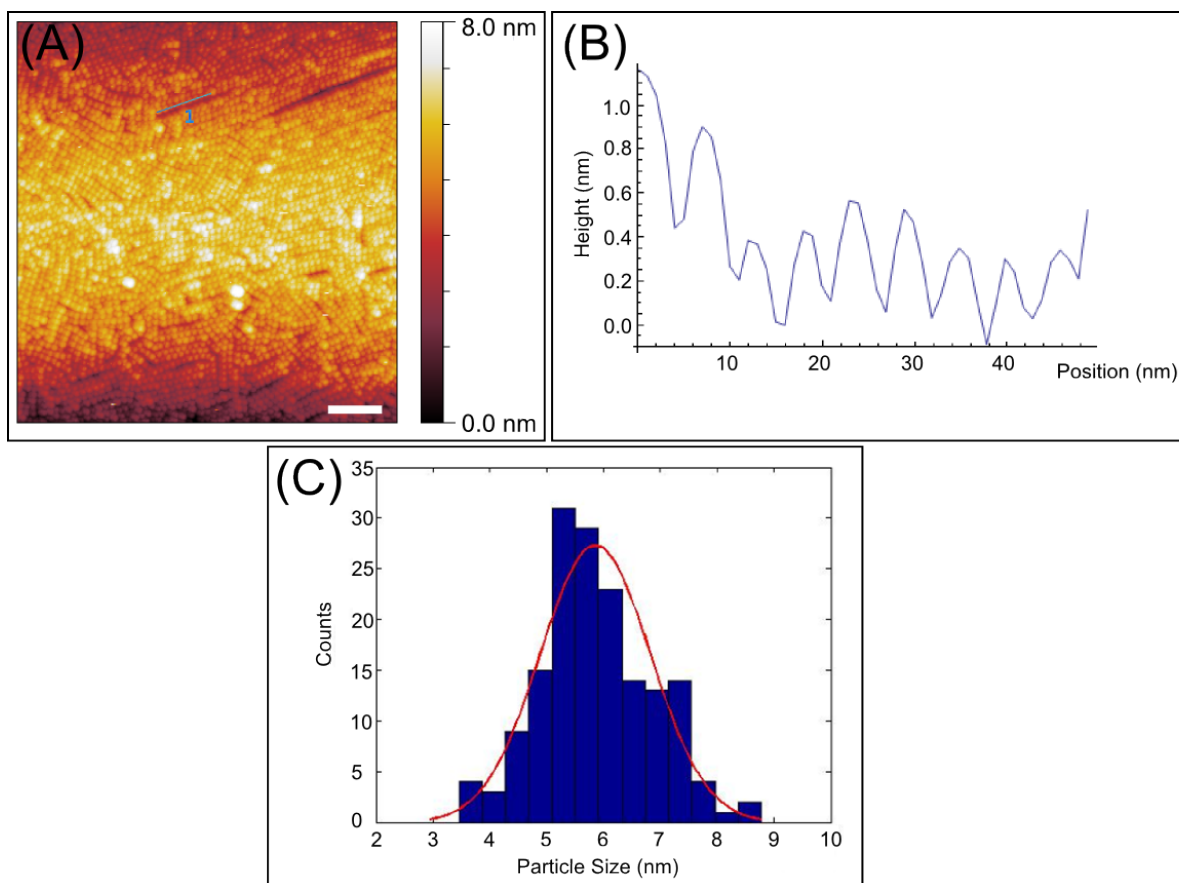


Figure 6.7: (A) Zoom onto linear structures.  $V = 1.5\text{V}$ ,  $I = 5\text{ pA}$ . The small line denotes the path over which the height profile, as seen in (B), was taken. (C) Size distribution of the NCs inside the linear supercrystal. Scalebar denotes 60 nm.

Long range ordering can be investigated by taking 2D Fourier transformations of the acquired images. As one gets from real to reciprocal space (analogous as going from time to frequency space) one gets information on the periodicity of the sample. This can be seen in the figure below for the linear structures;

As can be seen in figure 6.8 (A) an overview is acquired with mild scan parameters. The image is filtered with the Gwyddion software package, where an FFT of the image is generated. As expected for the linear structures, little to no long range order is observed, as there are no bright, well defined spots in the FFT image. There does appear to be some form of directionality in the FFT, which might be due to alignment of the chains with the trigonal lattice of the HOPG. This statement has yet to be proven.

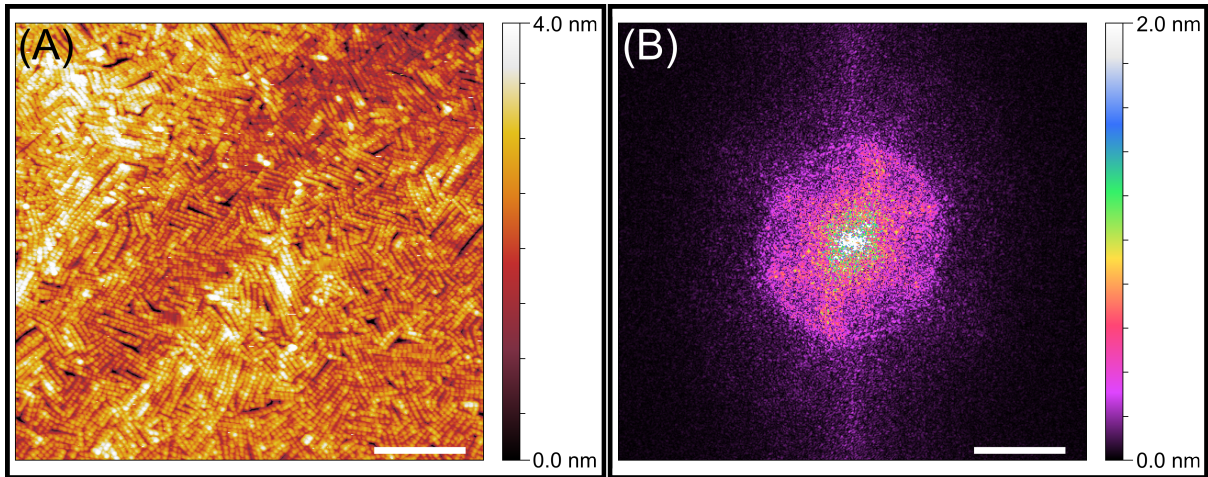


Figure 6.8: (A) Overview at  $V= 1.5V$  and  $I= 5pA$ , scalebar denotes 100 nm. (B) FFT of (A) which shows little long range correlation, scalebar denotes  $0.1 \text{ nm}^{-1}$

### 6.2.1 Anomalous facet attachment

Recently, Evers has succeeded in achieving complete cation exchange from Pb to Cd on the supercrystals. This resulted in a change of the atomic crystal structure, namely from rocksalt to zinc blende, but with preservation of the NC shape and supercrystal geometry. HAADF-STEM measurements have been performed, initially with an interest on the honeycomb crystals, but some linear and cubic geometries were also present on the sample grid. An example is shown in figure 6.9 (A). Regions of enhanced contrast within the supercrystal are observed, which can be explained by overlap of the constituent NCs in the supercrystal. This can occur if the facets do not attach via the  $\{100\}$  planes, but via the  $\{110\}$  planes. An atomic model, illustrating this type of attachment is shown in figure 6.9 (B). The contact area between the nanocrystals is smaller when attachment occurs via  $\{110\}$  planes compared to attachment via the  $\{100\}$  planes. An in depth study into this subject has not been performed yet.

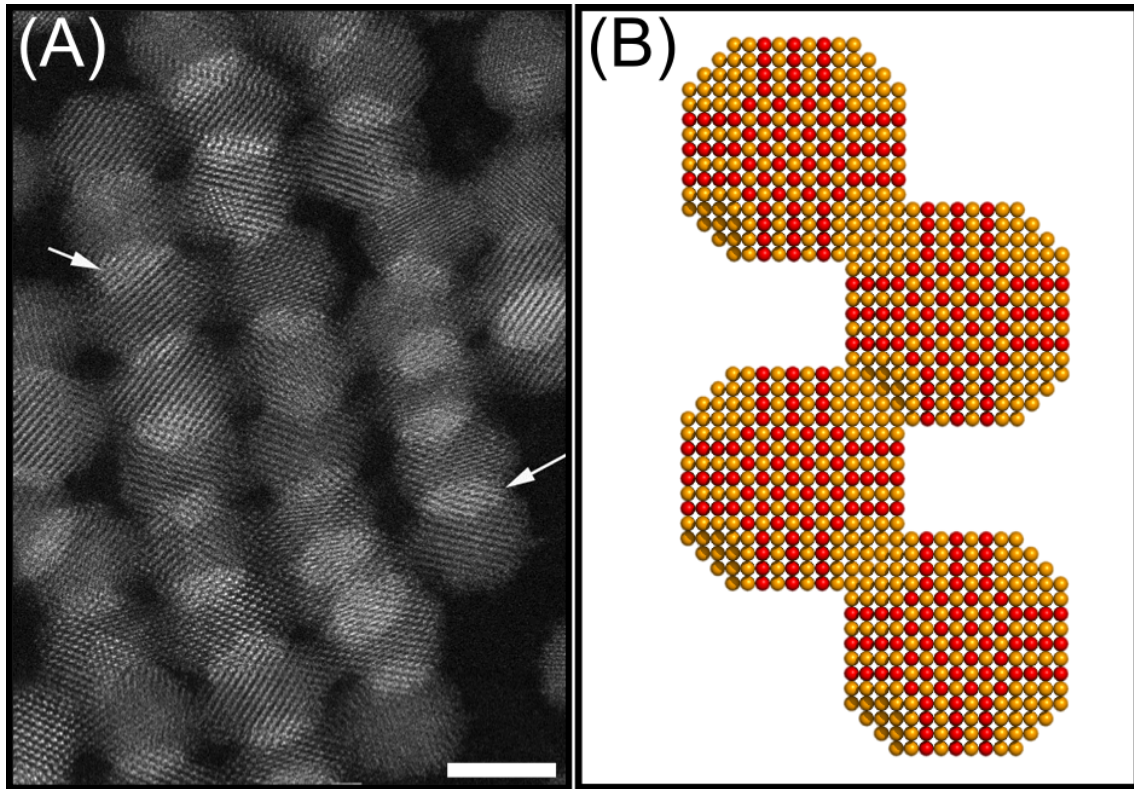


Figure 6.9: (A) HAADF-STEM micrograph of the CdSe linear superstructures. Arrows indicate some areas where overlap of the NCs in the structure occurs, as seen by the enhanced contrast. (B) Side view of the proposed facet attachment of the NCs via the  $\{110\}$  facets. Scalebar denotes 5 nm.

### 6.3 Square supercrystals

At the highest NC dispersion concentration ( $30 \times 10^{-7}$  mol/L), we obtain the square sheet supercrystal geometry. The grids were almost always covered with small patches of linear structures as well. No honeycomb supercrystals are observed on these grids, which is remarkable as they form in between the linear and square supercrystal concentration. The figure below shows acquired TEM images of a few samples;

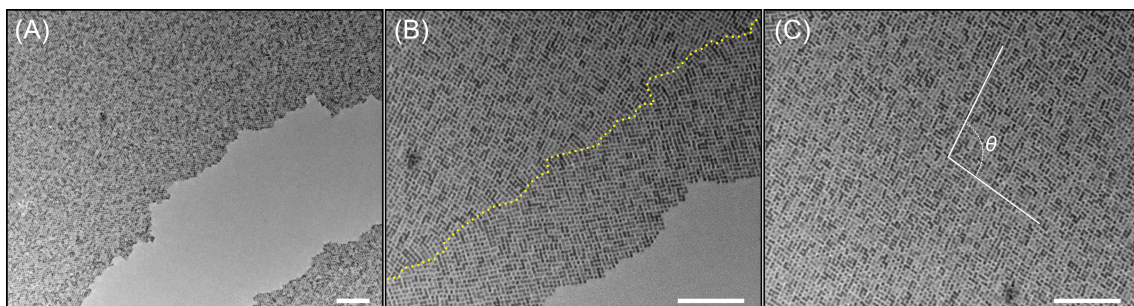


Figure 6.10: Overview images of the square supercrystals. (A) shows a large overview of approximately  $1 \mu\text{m}^2$ . A large square sheet is formed. (B) Zoom in of (A), where the dashed line shows a grain boundary. (C) Large domain within a square sheet. The angle between the two directions in the supercrystal  $\theta$  ( $100^\circ$ ) is indicated. Scalebars denote 75 nm.

As can be seen in figure 6.10 (A) large patches of square superlattice are formed. They connect via four  $\{100\}$  facets. Most of the time the square supercrystals contain several domains, in which the orientation of the square sheets is slightly rotated. These regions are separated by grain boundaries, which is illustrated in figure 6.10 (B). Note that the angles between constituent particles are not always exactly 90 degrees, which one would expect for (truncated) cube shaped particles. There appears to be a shift towards higher ( $\theta \approx 100^\circ$ ) angles, which is illustrated in figure 6.10 (C). This is presumably caused by deformation of the particles into more diamond shaped particles, i.e. deformation along a body diagonal.

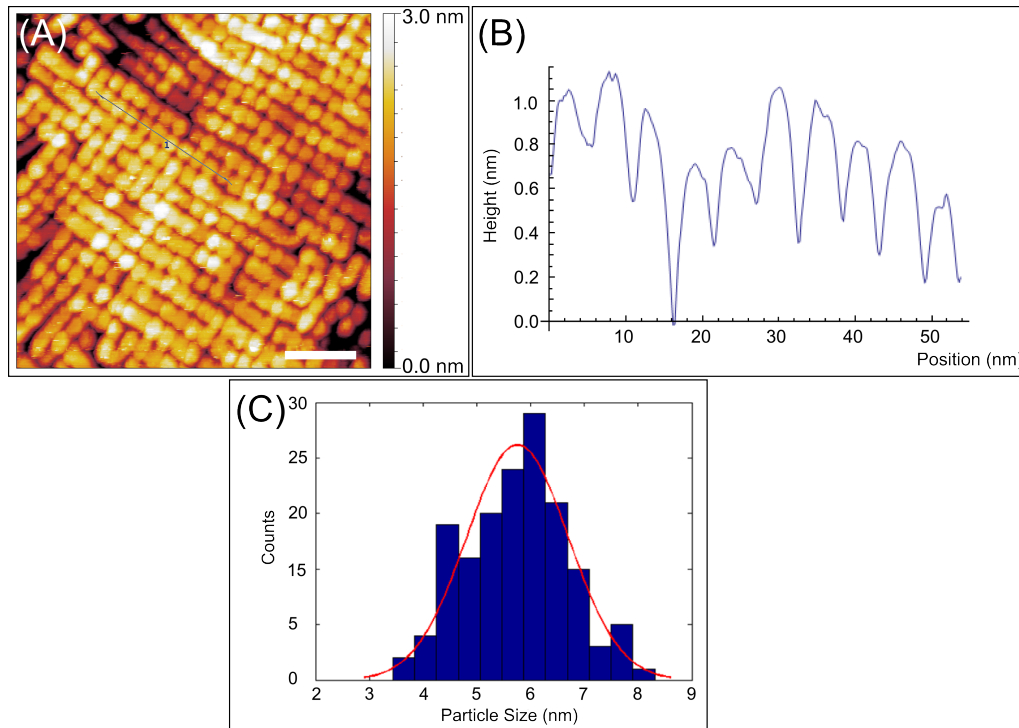


Figure 6.11: (A) Zoom onto square structures,  $V= 1.5$  V,  $I= 5$  pA. The small line denotes the path over which the height profile, as seen in (B), was taken. (C) Size distribution of the NCs inside the square supercrystal. Scalebar denotes 25 nm.

The above figure shows a zoom in onto a region with a square supercrystal. As can be seen, the individual NCs inside the system are resolved. A line trace was taken over a square sheet, which is depicted in figure 6.11 (B). The NC corrugation inside the supercrystal is clearly distinguished. The average particle size within the supercrystal was determined as described in the section on the linear supercrystals. The as obtained average NC size over 130 detected particles within the supercrystal is  $5.8 \pm 1.4$  nm.

The long range order was investigated by taking the 2D FFT of acquired images, which are shown in the figure below;

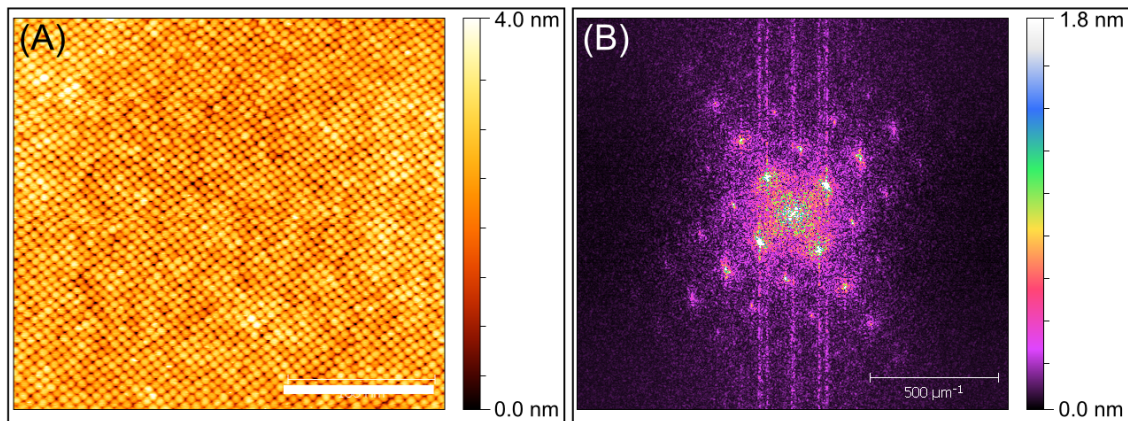


Figure 6.12: (A) overview of a single domain of square supercrystal, scalebar denotes 100 nm. Image obtained at  $V= 1.5V$  and  $I= 5 \text{ pA}$ . (B) FFT of (A). The long range square order of the constituent particles can be observed clearly through the clear square pattern of spots appearing in the FFT.

The clear square pattern in the FFT shows that there is a long range four-fold symmetric order of the constituent NCs. The average periodicity obtained from the FFT is, quite intuitively, approximately the NC diameter ( $0.178 \text{ nm}^{-1} \equiv 5.6 \text{ nm}$ ).

## 6.4 Honeycomb supercrystals - geometry and electronic structure

### 6.4.1 Geometry - TEM

At intermediate concentrations ( $\approx 11 \times 10^{-7}$  mol/L) the honeycomb supercrystals are obtained. Almost all samples also contained linear and square supercrystals, but the honeycomb supercrystal dominates the substrate at these conditions. The figure below shows acquired TEM images of these structures;

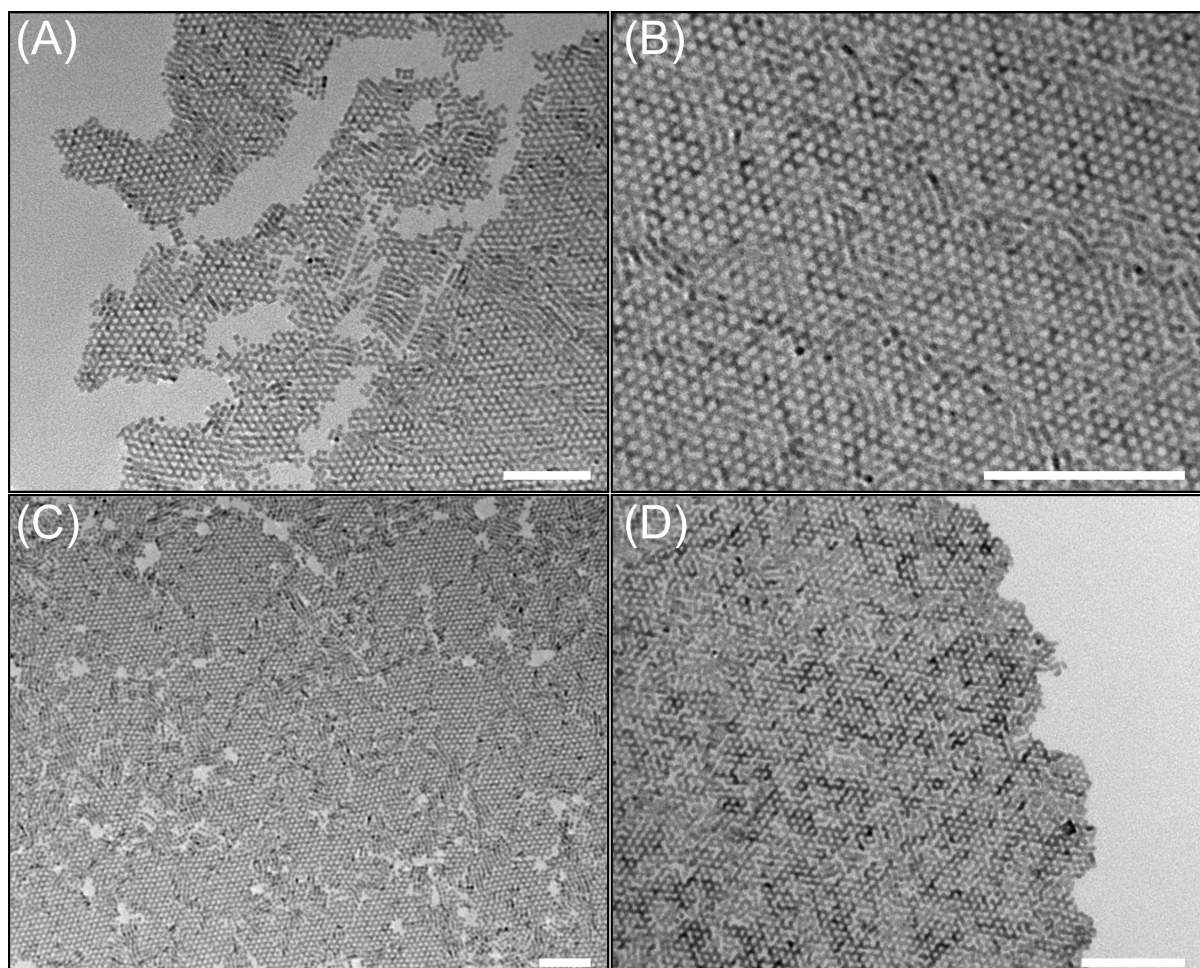


Figure 6.13: TEM overviews of the acquired honeycomb supercrystals. (A) Overview of honeycomb supercrystal near edges. The micrograph was acquired at this position to prove that the seen structure is not a measurement artefact. (B) Same sample as in (A), where linear defects are seen throughout the structure. (C) Different sample in which the supercrystal contained more defects. Linear structures and cracks run throughout the sample. (D) Again a different sample, image acquired on a relatively large honeycomb sheet near the edge of the supercrystal. Scalebars represent 100 nm.

Figure 6.13 shows several micrographs of the honeycomb supercrystal. Figure 6.13 (A) and (B) are taken on the exact same sample, while (C) and (D) show structures on other acquired samples, which are synthesized on different days. The overviews clearly show the

honeycomb geometry of the crystals; the triangular lattice, which is analogous to graphene, is distinguishable from the other supercrystals. To demonstrate that the honeycomb geometry is a property of the supercrystal and not a measurement artefact (which can easily be acquired in TEM measurements on self assembled hexagonal patches of particles by an incorrect focal depth setting), the structure was checked along its edges, as seen in (A). When we zoom in, as seen in (B), we can immediately see that the structure is not defect-free. However, even in the presence of (large) defects, the overall atomic and nanocrystal coherence is retained and large sheets of single-crystalline supercrystals formed. (C) displays a very large overview, where cracks and linear defects are seen. Most supercrystals contained cracks, which are presumably caused by drying the sample. (D) again shows an acquired micrograph along the edge of a different sample.

One could easily assume that the honeycomb structures are perfectly two-dimensional and attach via the  $\{110\}$  facets. However one must always bear in mind that with TEM (or any other transmission microscopy technique) the acquired images are a 2D projection of a 3D object. The proof that the structures are actually quasi-2D will be given below.

#### 6.4.2 Geometry - STM

To study the electronic structure of the honeycomb supercrystals, samples were also scooped on HOPG and inserted into UHV for STM measurements.

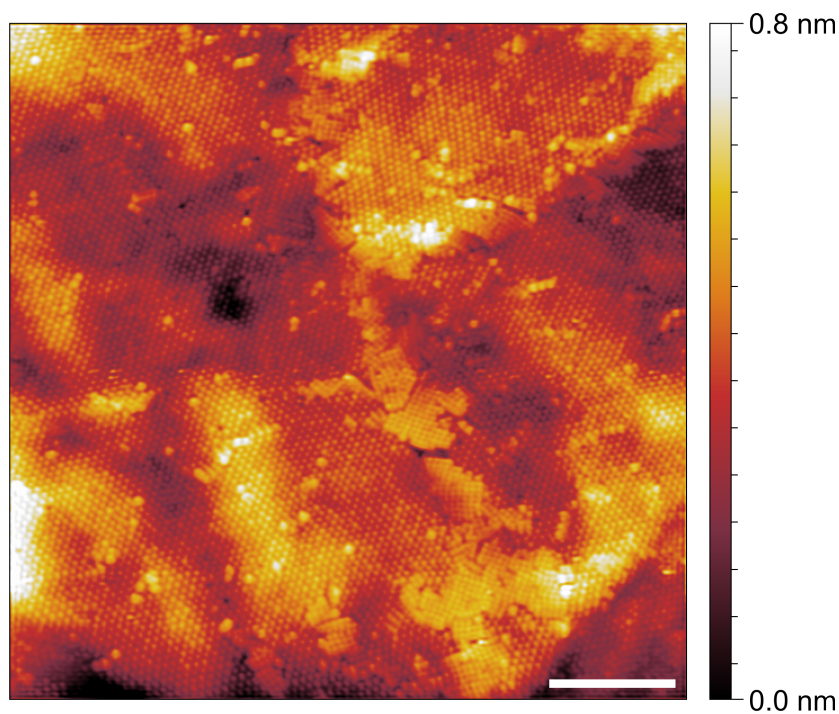


Figure 6.14: Large overview of a PbSe honeycomb supercrystal in STM. Large sheets are obtained, containing linear and square defects, which were also observed in TEM. The contrast displays an hexagonal geometry which is elaborated on further in this section. Image acquired at  $V= 1.5$  V and  $I= 5$  pA. Scalebar denotes 125 nm.

The figure above shows a large overview ( $600 \times 600 \text{ nm}^2$ ) of the obtained honeycomb supercrystals. A rather peculiar and unexpected close-packed hexagonal layer is observed in the image contrast. This is unexpected since at these synthesis conditions we never observed self-

assembled hexagonal patches in TEM. It will be shown that the contrast is mainly determined by the bluntness of the tip apex. Defects show linear and square supercrystals, as well as large cracks in the structure.

Same as for the linear and square supercrystals, we can obtain the average size of the constituent NCs inside the supercrystals. The results are displayed in the figure below;

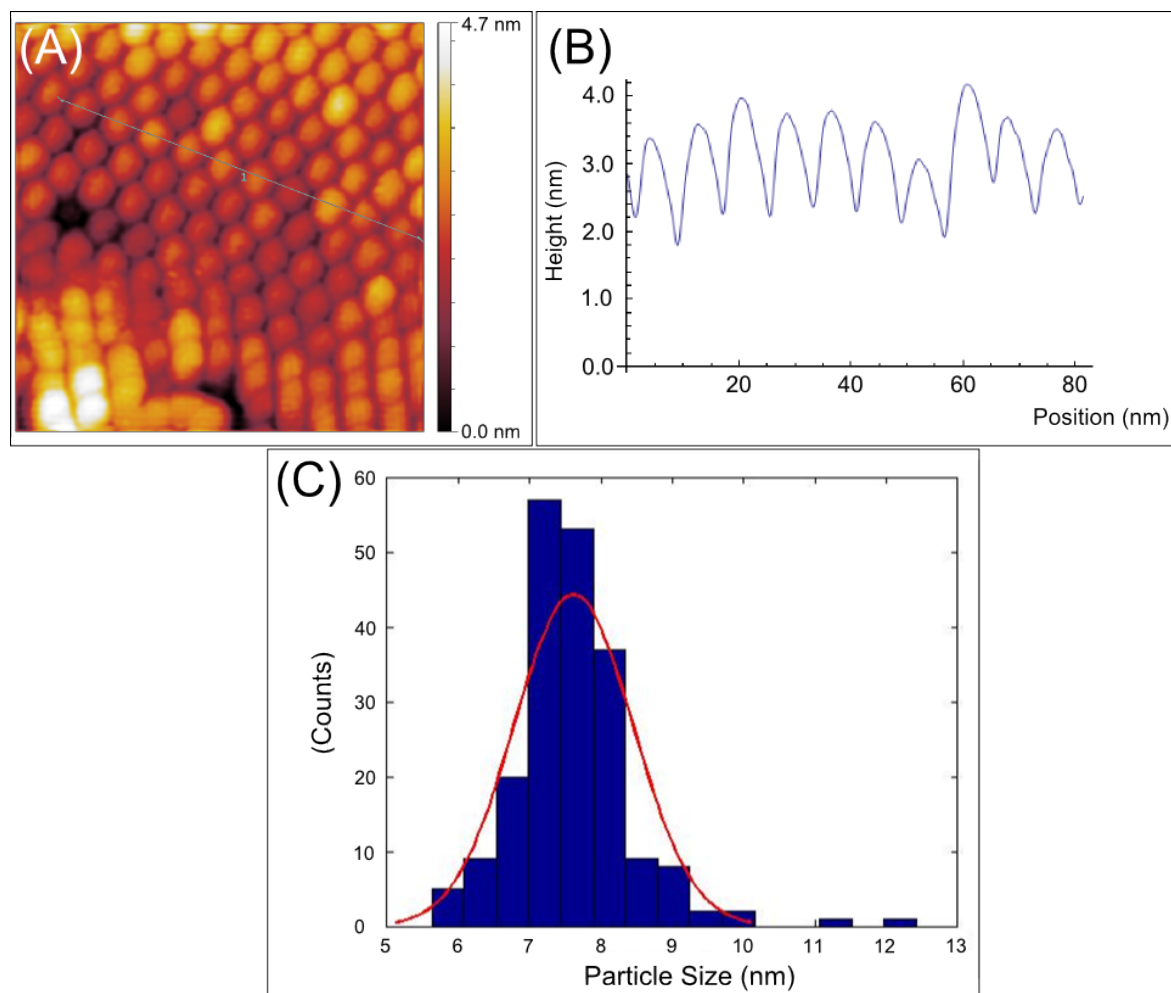


Figure 6.15: Size distribution of the NC's inside the honeycomb lattice. (A) overview of an hexagonal array of particles, image obtained at  $V=1.5\text{V}$  and  $I=5\text{pA}$ . The line depicts the path over which the height profile, as seen in (B), was taken. (C) obtained size distribution of the NCs inside the supercrystal.

As can be seen in figure 6.15 (A), the NCs inside the supercrystal can be again resolved quite easily. Again a large number of height profiles (detecting 210 particles), as seen in (B), are collected in order to obtain the histogram as displayed in figure 6.15 (C). A rather peculiar result is obtained however, as the particle size in STM acquired in this manner is  $7.6\pm 0.8\text{ nm}$ , which deviates substantially from the average NC size as obtained in TEM ( $5.5\text{ nm}$ ). Even more interesting is the fact that the particle size deviates almost  $2\text{ nm}$  from the linear and square supercrystals. Several theories to account for the large deviation of  $2\text{ nm}$  have been proposed so far. A hypothesis could be that when the tip apex is quite blunt, the current running from

tip to sample on a hollow position in the supercrystal (in a 'hole') could be larger than on top of a constituent NC, as there would be current running through several NCs. This would result in a hexagonal array of particles as we observed in STM images. However we can discard effect on basis of the edges, as the particles at these positions still appear as a close-packed hexagonal layer.

The last hypothesis is that we are imaging every other NC inside the supercrystal. Further elaboration on this will be done below.

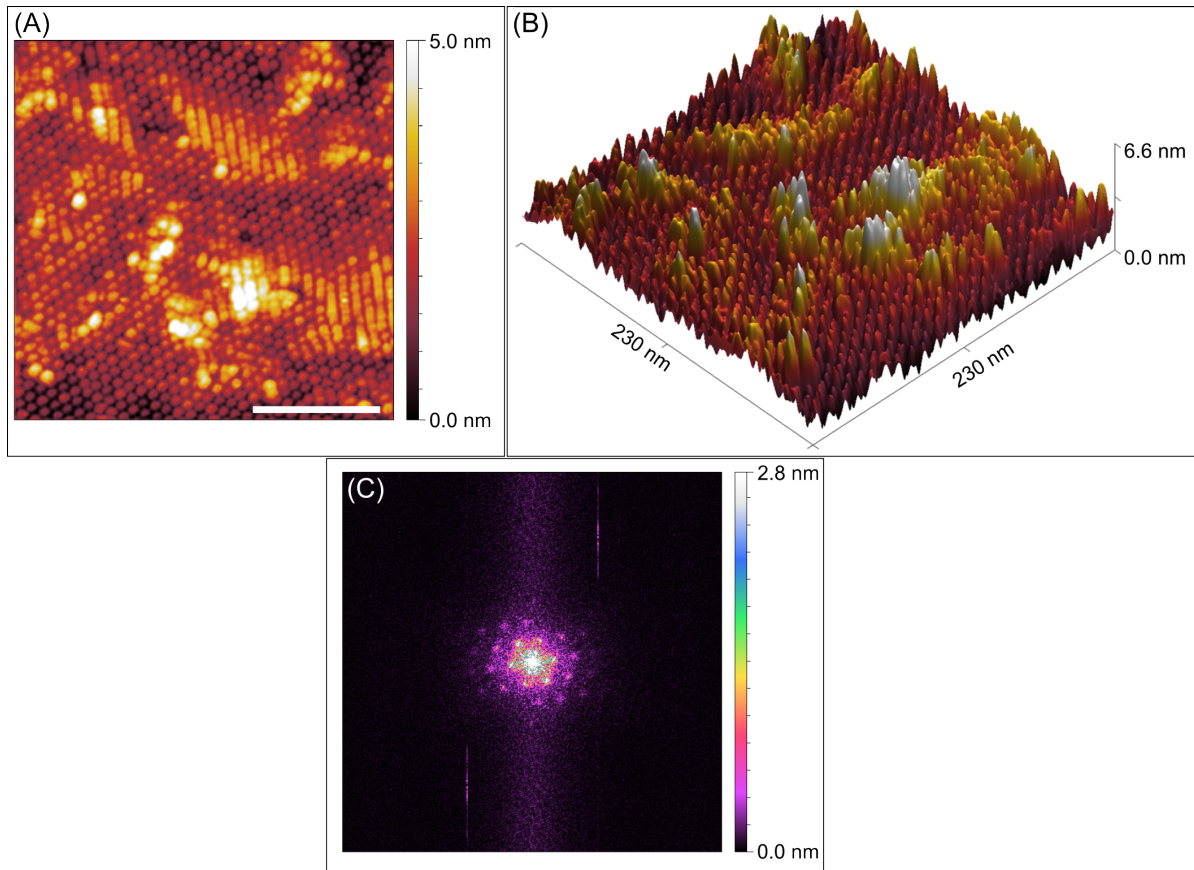


Figure 6.16: Different sample containing PbSe honeycomb supercrystals. (A) shows an overview of an hexagonal packing of particles, which is rendered in 3D in (B). Figure (C) is the FFT of (A), showing the long-range order of the crystal. Scalebar denotes 100 nm.

The long range order can be verified by looking at the 2D FFT of a large overview. Clear hexagonal order of the constituent particles is observed, as seen in the FFT in figure 6.16 (C).

The experiments described below were all performed on CdSe supercrystals. As stated above the atomic crystal structure is changed from rock-salt to zinc-blende. This has no direct consequences for the overall supercrystal geometry, but does have an impact on the electronic structure. This effect is described later on in the section on STS. During these LT-STM experiments we have observed three different types of image contrast, which are all displayed in figure 6.17.

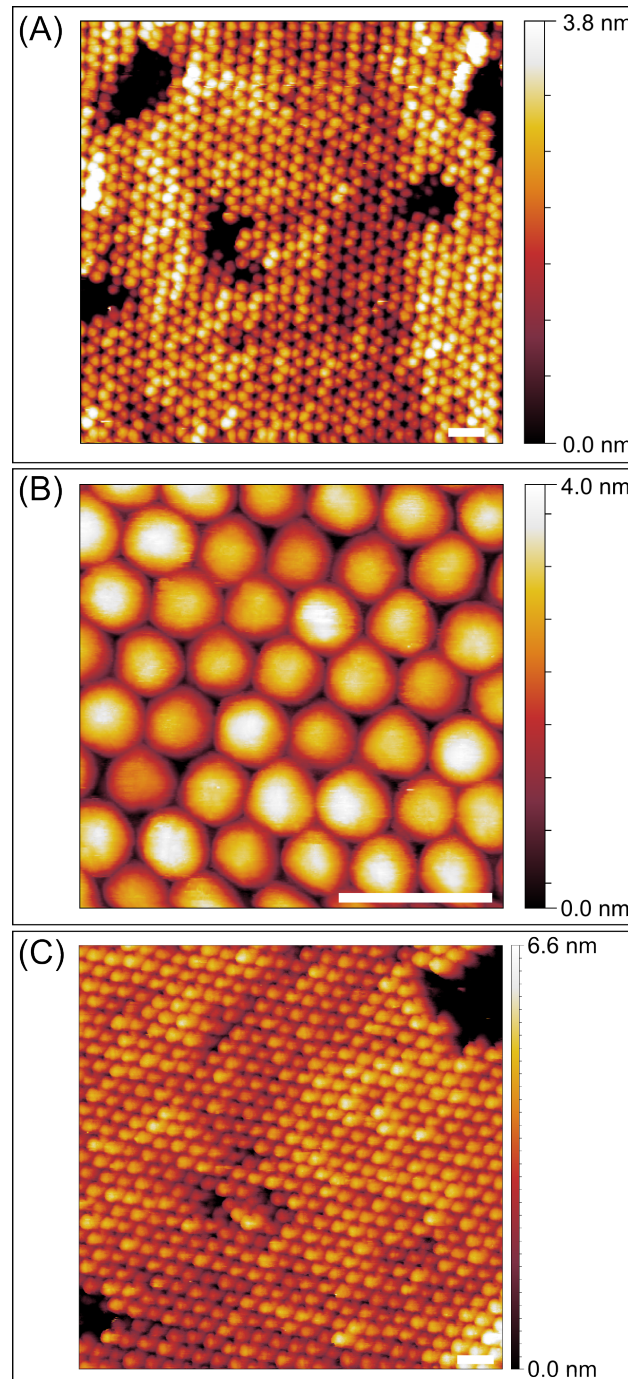


Figure 6.17: Three different types of image contrast observed; honeycomb (A), hexagonal (B) and silicene (C). Scalebars indicate 15 nm. Images acquired at  $V=3.5$  V,  $I=10$  pA. Scalebars denote 15 nm.

- Honeycomb image contrast, clearly displaying the geometry of the supercrystal.
- Hexagonal image contrast, where we only observe the A-positions of the supercrystal.
- Silicene image contrast, where we are able to distinguish between the A and B-positions of the supercrystal.

(A) clearly displays a honeycomb contrast. If this is due to the actual geometry or an electronic effect is still not clear. (B) displays a clear hexagonal contrast which was also observed on the PbSe crystals. (C) shows a silicene lattice, not seen before in the VT-STM experiments. What makes the obtained images even more peculiar is that they were taken on roughly the same sample area. Also experiments on the same area, but with a different tip have been performed, displaying different contrast (after tip-preparation on a different spot). As the sample is unaltered, we can conclude that the image contrast which is observed on these supercrystals is dictated by the bluntness of the tip apex. As the tip becomes more blunt, we are not able to penetrate deep enough in the supercrystal to observe the lower B-positions of the supercrystal. The hexagonal image contrast is then build up out of the NCs on the higher A-positions, which in combination with tip-sample convolution, also explains the increased particle size.

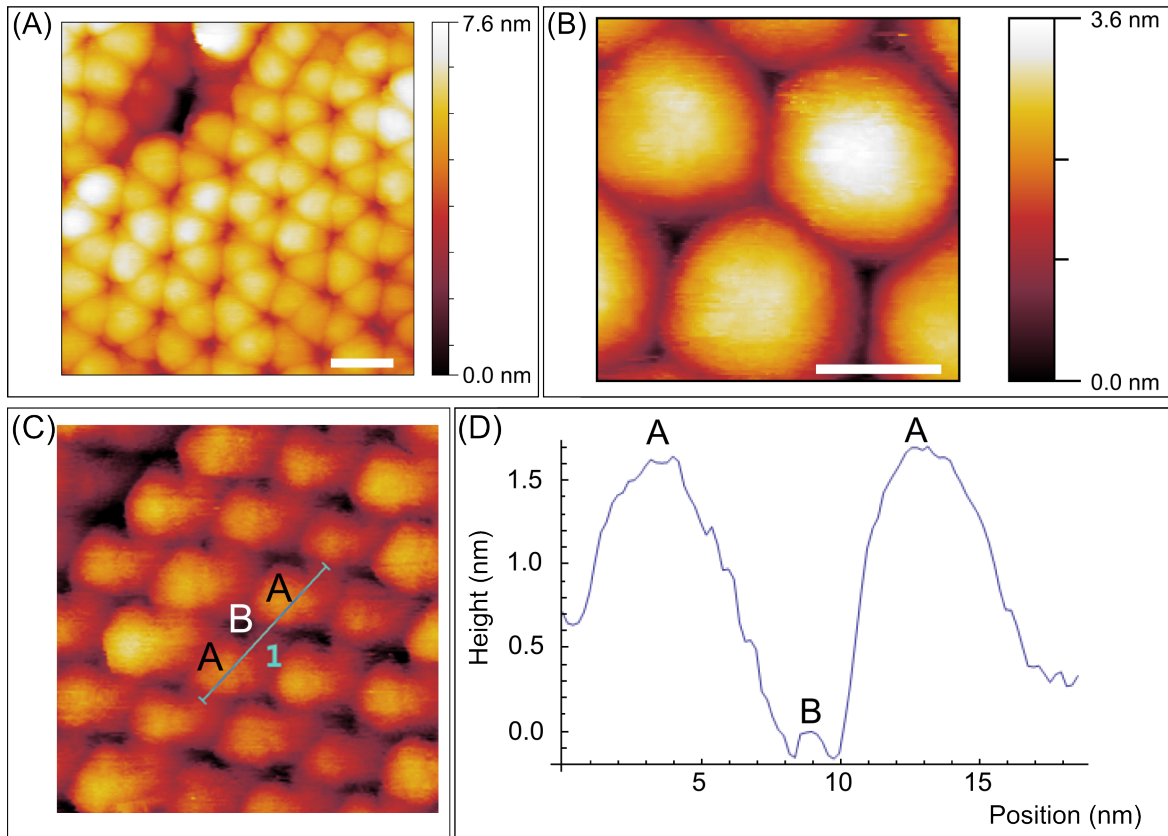


Figure 6.18: Zoom in on the honeycomb (A) and hexagonal (B) image contrast. (C) zoom in on the silicene-like supercrystal. (D) acquired height profile over the line as seen in (C). Scalebars indicate 6 nm. Image acquired at  $V= 3.5$  V and  $I= 10$  pA.

The figure above shows some zoom-in micrographs obtained on the honeycomb (A) and hexagonal (B) image contrast. As stated above the sharpness of the tip dominates the obtained image contrast. Hence the honeycomb and hexagonal image contrast as can be seen in (A) and

(B) were recorded with a relatively sharp and a relatively blunt tip apex respectively. Figure 6.18 (C) shows a zoom in on the supercrystal, while figure (D) shows the acquired height profile over the line in figure 6.18 (C). As can be seen from the height profile we can distinguish both sublattices in height; the A-positions and B-positions are marked both in the height profile as in the acquired image

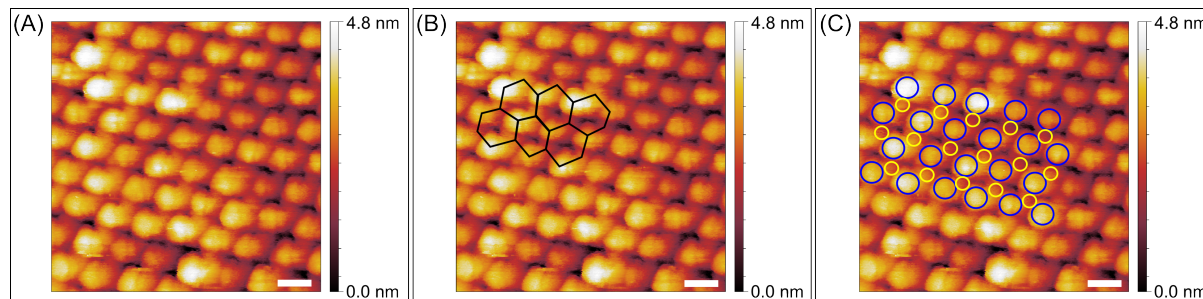


Figure 6.19: Zoom in on the images with silicene image contrast. Where (A) shows the raw image, (B) has a distorted honeycomb lattice overlaid to it as a guide to the eye and (C) shows the A-positions (blue circles) and B-positions (yellow circles) as a guide to the eye. Image acquired at  $V = 3.5$  V and  $I = 10$  pA. Scalebars represent 5 nm.

The silicene image contrast is quite remarkable; we are able to see both sublattices with the STM, which was not seen with the experiments at room temperature. The higher sublattice, the A-positions, are seen more clearly and appear larger than the lower sublattice, the B-positions - see figure 6.19 (A)). The honeycomb nature of the supercrystal becomes more clear in figure 6.19 (B), where a distorted honeycomb lattice was positioned over the image as a guide to the eye. Figure (C) contains markers for each sublattice; the blue circles indicate the A-positions, while the yellow circles mark the B-positions. The ability to resolve both sublattices gives us the opportunity to perform spectroscopy on both of sublattices respectively, to see whether there is a significant change in the DOS on either the A or the B sublattice.

### 6.4.3 Geometry - HR-SEM

To confirm whether the peculiar image contrast in STM is a tip artefact or due to a densely packed hexagonal layer of QDs, HOPG substrates containing the hexagonal packed particles (as measured in STM) were transported in an inert atmosphere to Ghent University where HR-SEM measurements have been performed. The figure below shows an overview image on one of the substrates;

To obtain the above image several difficulties had to be overcome. Focus was hard to achieve due to the high electron beam energy; the nanocrystals were very easily fused or destroyed. Adjustment of the electron beam had to be very quick and no perfect focus could therefore be achieved. Also the HOPG crystal was not perfectly flat, resulting in complete readjustment of the focal plane every time a different spot had to be imaged. These difficulties are resembled in the obtained image in figure 6.20 (A). As can be seen the image is quite blurry. After taking the 2D FFT of the image, (B), we can apply a filter to remove the noise from the image, however one is not to overfilter the image. The image difference (D) should not contain any regular patterns arising from the supercrystal and only noise should be filtered away. The obtained image (C) is somewhat more clear. It can be seen that no longer a hexagonal packing of particles is observed, but a hexagonal packing of holes. The hexagonal geometry is furthermore seen in the Fourier analysis of the image. This would correspond to the honeycomb lattice, but would not explain

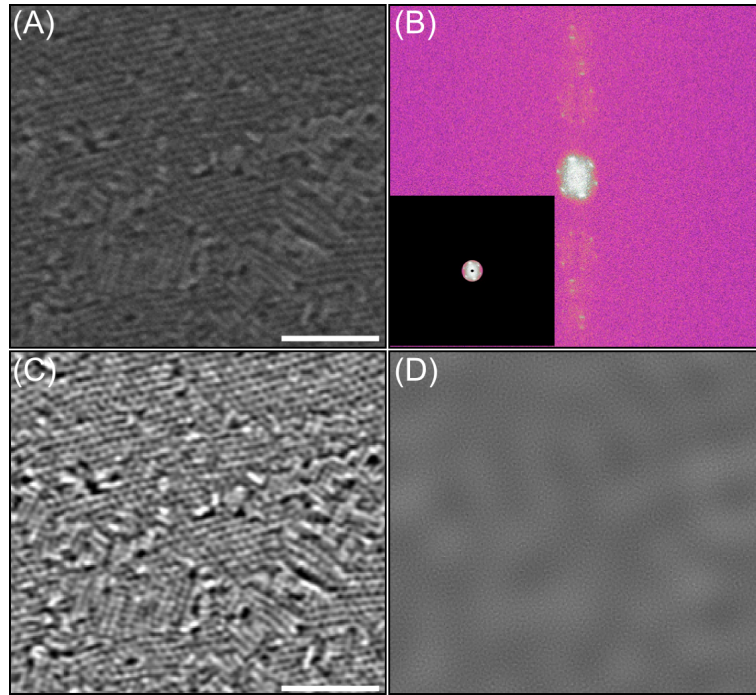


Figure 6.20: (A) Overview image on one of the HOPG substrates (raw data), obtained at 18 kV. (B) Fourier transform of (A), where the inset shows the applied filter to generate (C). (D) is the image difference from the filtered and unfiltered image,  $(D)=(A)-(C)$ . Scalebars denote 100 nm.

the image contrast in STM. More analysis is done in the next figure, where multiple zoom-in images on the raw data have been filtered.

Figure 6.21 shows an overview image and zoomed-in regions acquired with HR-SEM. (A) is an overview of the honeycomb superlattice. Several regions from the raw data have been picked out and used further. (B), (F) and (J) are the raw acquired micrograph zooms. (C), (G) and (K) are the FFTs of the (B), (F) and (J) respectively, which were used to filter out the noise from the images. (D), (H) and (L) are the filtered images acquired after FFT filtering and (E), (I) and (M) is the noise which was filtered away from the raw data. The sample, which showed a hexagonally packed particles in STM, apparently does contain honeycomb supercrystals. This is even more clearly shown in (D), (H) and (L) where trigonal lattice is observed. Further analysis on the honeycomb supercrystal is done in order to determine where this effect in STM comes from.

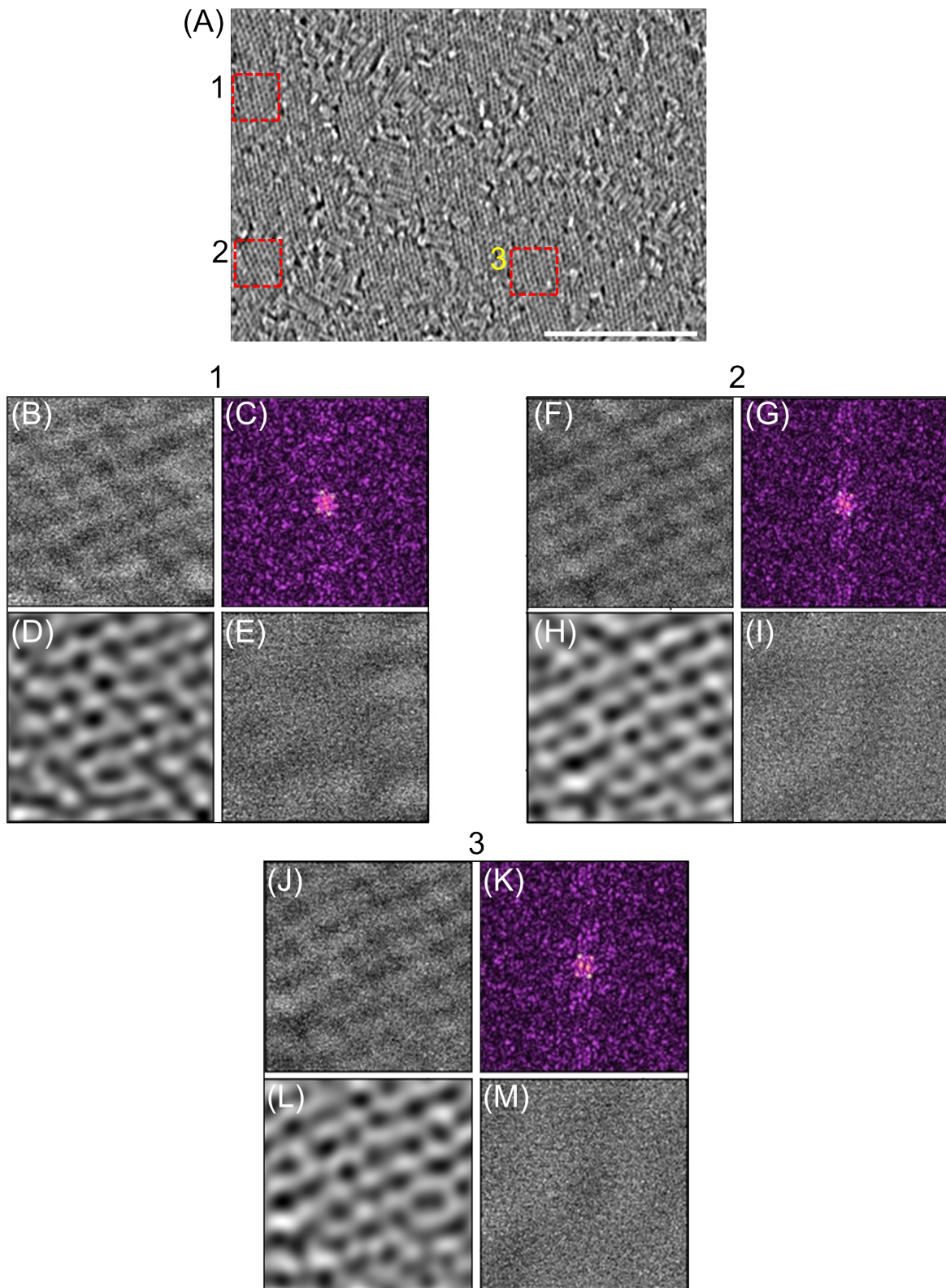


Figure 6.21: HR-SEM overview images which are filtered with 2D Fourier transform filters. Scalebar denotes 100 nm.

#### 6.4.4 Geometry - Electron Tomography

In transmission microscopy one obtains a two-dimensional information stack about a three-dimensional object. However, when imaging the object over different consecutive angles, acquiring different 2D data stacks, one can combine these into a 3D reconstruction of the image. This technique is called tomography and it is used to elucidate the geometry of the honeycomb supercrystal. As described in chapter 2 the honeycomb lattice can be formed via attachment via two facets;

- Attachment via the  $\{110\}$  facets of PbSe results in a flat, graphene like structure.
- Attachment via the  $\{111\}$  facets of PbSe results in a buckled, silicene like structure, where two sublattices on different heights are formed.

The second option, the buckled silicene lattice, could explain the obtained STM contrast if the tip apex is blunt and hence only the top lattice can be imaged. Electron-tomography is the ideal technique to determine whether the supercrystal is flat or buckled, as we can obtain slice-throughs of the superlattice and perform particle detection. Slices from the obtained three-dimensional tomographic reconstruction of the lattice are shown in figure 6.22 below.

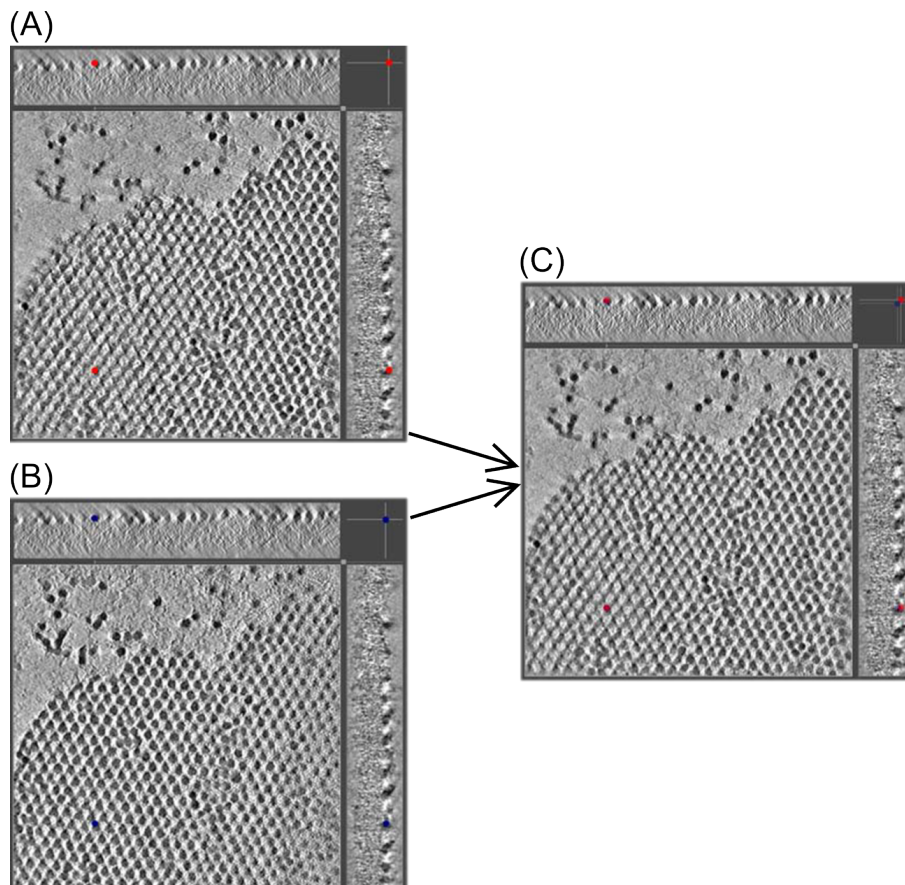


Figure 6.22: Results obtained by electron tomography on the honeycomb lattice. (A) and (B) show slice throughs of the 3D tomographic reconstruction of the superlattice at different height planes. (C) shows the combined images, depicting the honeycomb lattice once again. The insets on the top and right side of the image are side views of the obtained reconstruction.

When the 3D reconstruction is performed, we are able to look at the superlattice at different height planes (figure 6.22 (A) and (B)). We see only the partial triangular lattice of the honeycomb lattice in either one of them, which supports the hypothesis that every other NC is located at a different height in the supercrystal. When combining both images the honeycomb lattice is retrieved again. To further support the hypothesis, particle detection through the lattice was performed by M.P. Boneschanscher, using a spherical particle template. When the correlation between the data and the template was sufficient, a particle was allocated to that position. The figure below shows the obtained results;

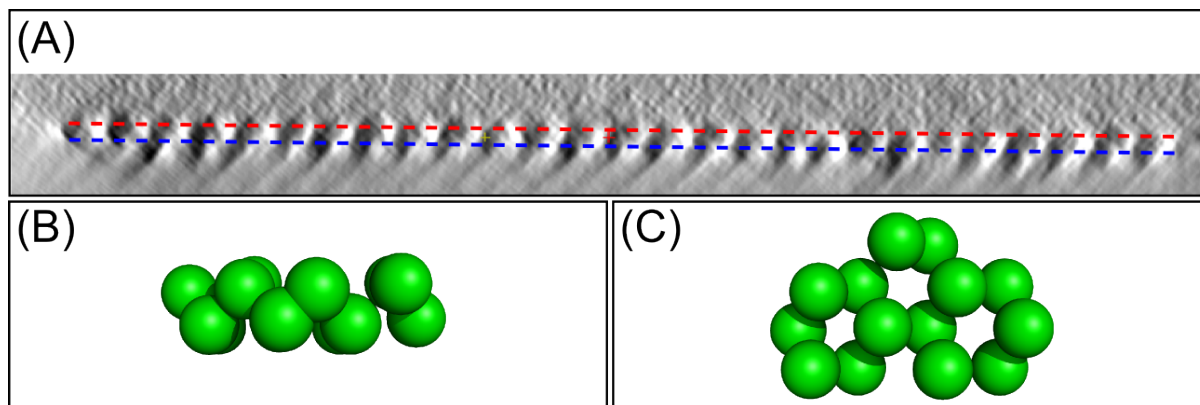


Figure 6.23: Results obtained by particle recognition through the reconstructed tomogram. (A) shows a side view of the tomogram, where two different particle heights are seen. Note that the particles appear black (B) Template position obtained by particle detection, side view, clearly showing two different particle heights. (C) Idem, but from a top view.

Clearly two different particle heights are detected<sup>1</sup>, with an interplanar spacing of  $\approx 2.6$  nm, which can be seen in figure 6.23 (A). Particle detection resulted in a silicene-type lattice, where every other atom is in a different sublattice, located at a different height. Better tomography experiments have to be done to ensure that no artefacts are present in the measurement. For example in figure 6.23 (A), clear wedges at the bottom of the slice are seen. These so called 'missing wedge' artefacts occur from the fact that not all angles can be measured; the obtained tomogram was measured between a sample angle of  $-60^\circ$  to  $+60^\circ$ . The missing angles are the cause of the wedges which occur in the data. Further improvement of the tomographic data can be done by using fiducial markers. These are often small particles, such as Au or Ag clusters, which are placed throughout the sample by simply emerging the TEM grid in a solution containing these markers. Throughout the tomography measurements, these particles can be traced and hence can be used as reference points for the reconstruction. By adequately determining the marker position at each tilt angle, very high z-resolved tomograms can be obtained.

<sup>1</sup>Data was obtained from initial tomography results, we zoomed in on a region of interest

### 6.4.5 Geometry - HAADF-STEM

Further verification that the honeycomb supercrystal actually has a silicene-type lattice was given by HAADF-STEM measurements. The figure below shows the two models, the graphene and the silicene analogue, overlaid on the atomically resolved micrographs recorded in the  $\langle 111 \rangle$  direction. When we attach the particles via the  $\{110\}$  facets, we are able to overlay one NC over the image, but its neighbouring particles do not overlap with NCs in the micrograph. Moreover, no atomic coherence can be obtained this way; it is not possible to overlap two nanocrystals attached via the  $\{110\}$  facet in such a fashion that the atomic columns overlap. If we now attach the NCs via the  $\{111\}$  facet we get full correlation between the model and the images. All the NCs overlap quite nicely and moreover the atomic columns of the models and the recorded micrograph overlap perfectly. This is illustrated in the figure below.

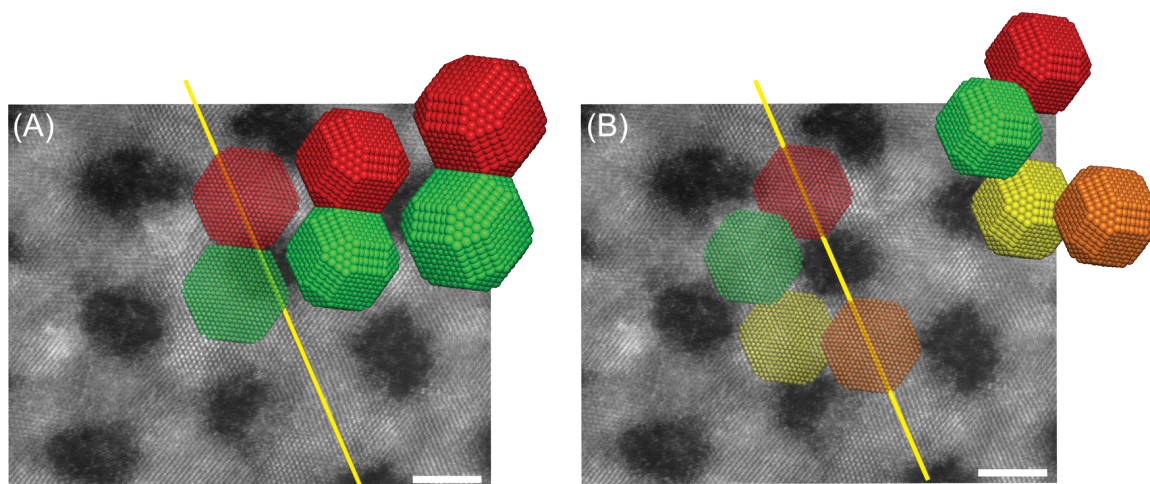


Figure 6.24: Atomic models on a HAADF-STEM micrograph. (A) shows attachment via the  $\{110\}$  plane resulting in a graphene-like structure. As can be seen no coherence between the atomic model and the micrograph can be obtained; the nanocrystals do not overlap the supercrystal and moreover, the atomic lattice is not reproduced by the model. (B) attachment via the  $\{111\}$  plane resulting in the silicene-like supercrystal. Good correlation between the micrograph and the models are obtained, both for the NC and atomic periodicity. Scalebars denote 5 nm.

More evidence is given by HAADF-STEM measurements on the ion-exchanged supercrystals. In these samples the Pb ions were replaced with Cd ions, changing the overall atomic crystal lattice from rocksalt to zinc-blende and preserving the supercrystal geometry. This also shows that the anionic crystal lattice is quite rigid, as the supercrystals are still retained.

Figure 6.25 is recorded in the  $\langle 111 \rangle$  direction. As indicated by the white arrows, there are several regions where NCs overlap, exactly at the area where they attach. This can be explained by NC overlap via attachment of the  $\{111\}$  facets or by incomplete cation exchange. As explained in the experimental chapter, higher Z number atoms and ions scatter more of the incoming electrons due to their own higher electron density. As Pb has a higher Z than Cd, regions where there would be Pb would result in a brighter contrast. Energy dispersive X-ray spectroscopy (EDX or EDS) however showed that the cation exchange resulted in a CdSe based supercrystal where the amount of Pb was below the detection limit of the detector (1%). Hence we can conclude from the above micrograph again that we have a silicene-like supercrystal.

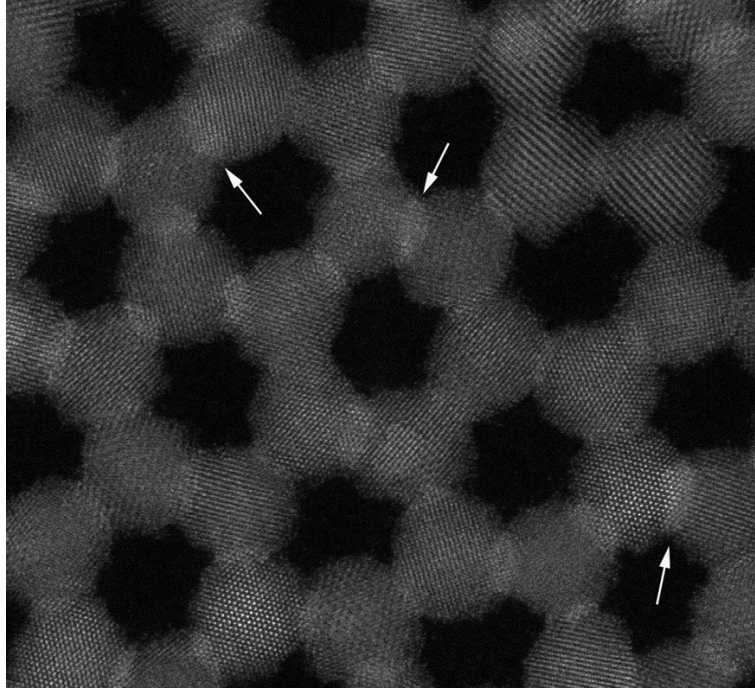


Figure 6.25: HAADF-STEM micrograph on a CdSe honeycomb supercrystal. The brighter areas, at the place where the NCs attach, originate from an increased number of atoms at that region, which in turns indicates overlap of the NCs. Scalebar denotes 5 nm.

#### 6.4.6 Electronic Structure - STS

Atomistic tight-binding calculations, i.e. giving each atom in the two-NC based unit cell a basis set, have been performed by E. Kalesaki and C. Delerue [17] in order to grasp the electronic structure of the supercrystals, in particular the band structure of the honeycomb supercrystal. It became clear that the band structure of PbSe supercrystals is very complex; as the intrinsic bandgap of the PbSe NCs lies at the  $L$ -point in reciprocal space, which is four-fold degenerate (8-fold when including spin), the states near the band edge experience a large amount of intervalley coupling and become hybridized. Understanding the supercrystal bands near the band edge hence becomes increasingly difficult. For CdSe, the bandgap lies at the  $\Gamma$  point, it does not experience hybridization of the states near the band edge. Hence, the bandstructure near the bottom of the conduction band and the top of the valence band is much simpler

In figure 6.26 (A) the band structure as calculated by Kalesaki and Delerue is displayed. For simplicity only the conduction bands are shown, which show the most remarkable features. As can be seen both the  $s$ -bands and  $p$ -bands do not touch each other at the  $K$  and  $K'$  points; this is due the slightly different potential the NCs experience at the different sublattices. The band structure can be translated to a DOS vs. energy diagram, by basically counting the number of allowed  $k$ -states at each energy; the more horizontal the band, the more allowed  $k$ -vectors it has there and hence the more states it has per unit energy at that specific energy. Adding up these allowed  $k$  points at each energy results in the DOS vs. energy diagram as seen in figure 6.26 (B). Some characteristic features are seen starting at 1.9 eV and ending at 2.15 eV, belonging to the  $s$ -bands of the supercrystal. The higher energy states originate from the  $p$ -bands of the supercrystal. Whether the rather dispersionless bands will be measured in STS experiments remains to be seen, as they arise from destructive interference of wavefunctions on neighbouring NCs.

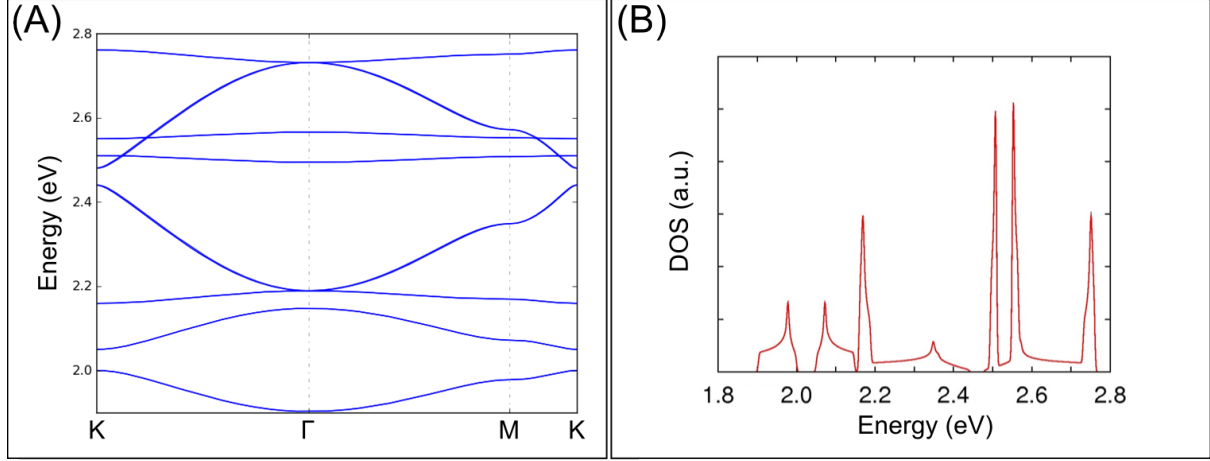


Figure 6.26: (A) calculated band structure of the silicene-type supercrystal going along the direction K- $\Gamma$ -M-K in reciprocal space. (B) Corresponding DOS of the supercrystal as calculated by integrating over the bands in (A). Image courtesy of E. Kalesaki and C. Delerue.

Another note on the interpretation of the spectra lies within the potential distribution (as described in chapter 4);

$$\eta = \frac{V_{tip-CdSe}}{V_{tip-CdSe} + V_{CdSe} + V_{CdSe-substrate}} \quad (6.1)$$

This lever arm will depend not only on the shape of the tip, but also on its position. When the tip is placed above an A-position of the supercrystal a maximum amount of the applied potential will be over the CdSe and hence the leverarm will be the smallest. The lever arm will increase more towards the sides of such an A-position and it logically follows that it will be the largest on a B-position. This effect can hence cause a shift in the obtained spectra along the energy (voltage) axis from position to position.

In principle, some  $k$ -dependence could be expected in the spectra. Normally when the electrons (or holes) tunnel from tip to sample they will have a wavevector perpendicular to the sample and hence couple weakly with states diverging from the  $\Gamma$ -point. The more lateral tunneling occurs in the supercrystals, the more they will have an in-plane wavevector component and hence couple with states further away from the  $\Gamma$ -point. However, this statement has yet to be proven.

Figure 6.27 shows the first spectroscopy experiments performed on the silicene supercrystal. All spectra obtained have been taken at the conduction band side of the supercrystal; the most interesting features in the calculated band structure appear here. The image obtained clearly shows both sublattices again, so we are able to perform spectroscopy on both the hollow sites as well as on the A and B-positions. In order to test whether we are in the shell filling or shell tunneling regime, spectra at different setpoint currents were recorded. As no extra resonances are observed, we can conclude that we are still in the shell tunneling regime, where the rate of electrons (holes) tunneling into the supercrystal is smaller than the rate of electrons (holes) tunneling out of the supercrystal. Furthermore, quite sharp resonances are observed in the tunneling spectra. This indicates that the system is not behaving as a 2DEG, where a step-wise increase in the DOS is expected.

Sudden increases in tunneling current are a result of a change at the tip-apex and hence must be disregarded in further interpretation. Large differences are seen from position to position in the obtained spectra. Whether this is a result of change in LDOS of the sample at each position or from tip-instabilities still has to be verified experimentally.

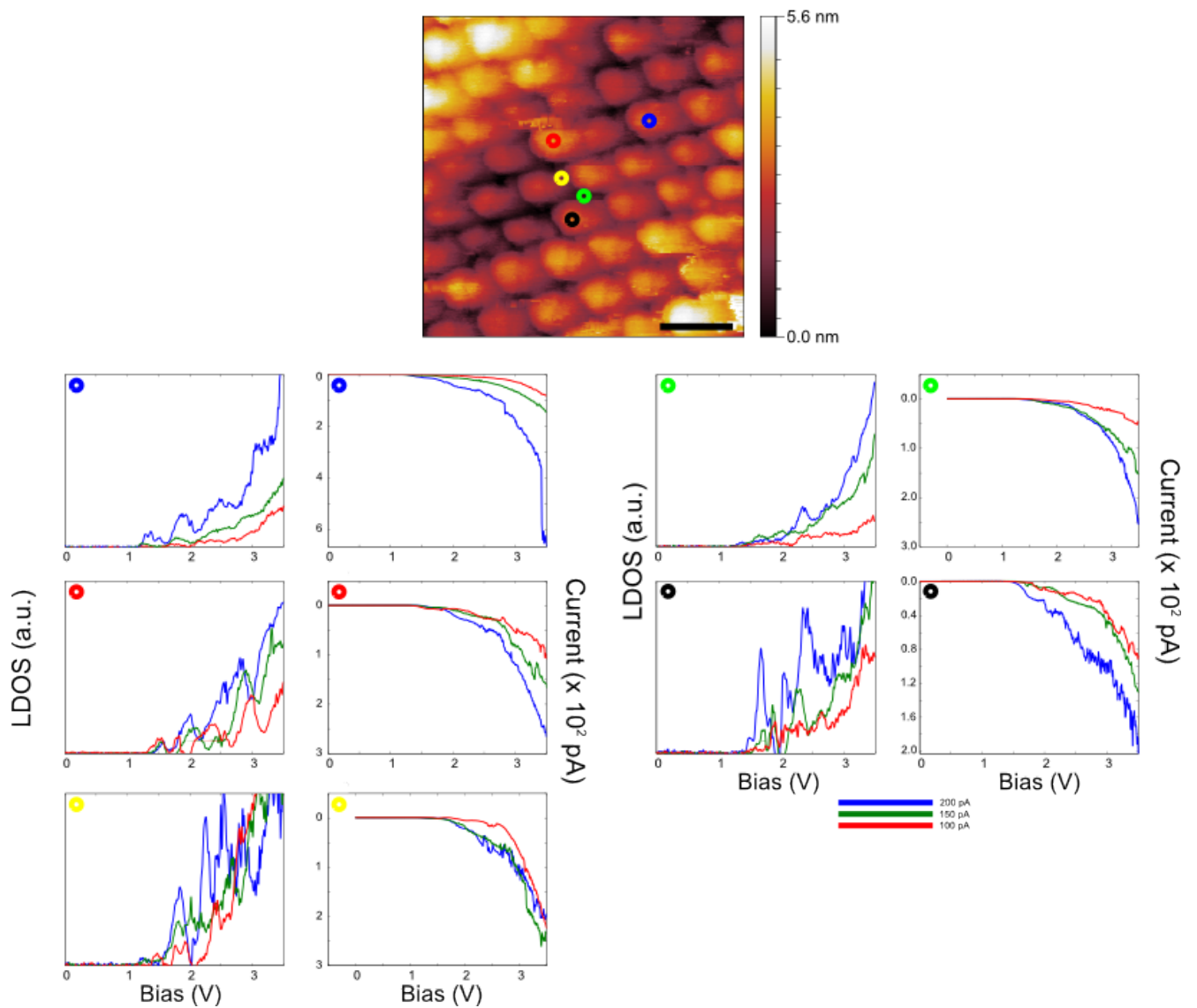


Figure 6.27: Spectroscopy on a part of a silicene supercrystal. Scan parameters  $V = 3.5$  V,  $I = 10$  pA, scalebar denotes 10 nm. These spectra were recorded with an oscillation amplitude of 20 mV at 730 Hz and a lock-in sensitivity of 100 mV at different setpoint currents.

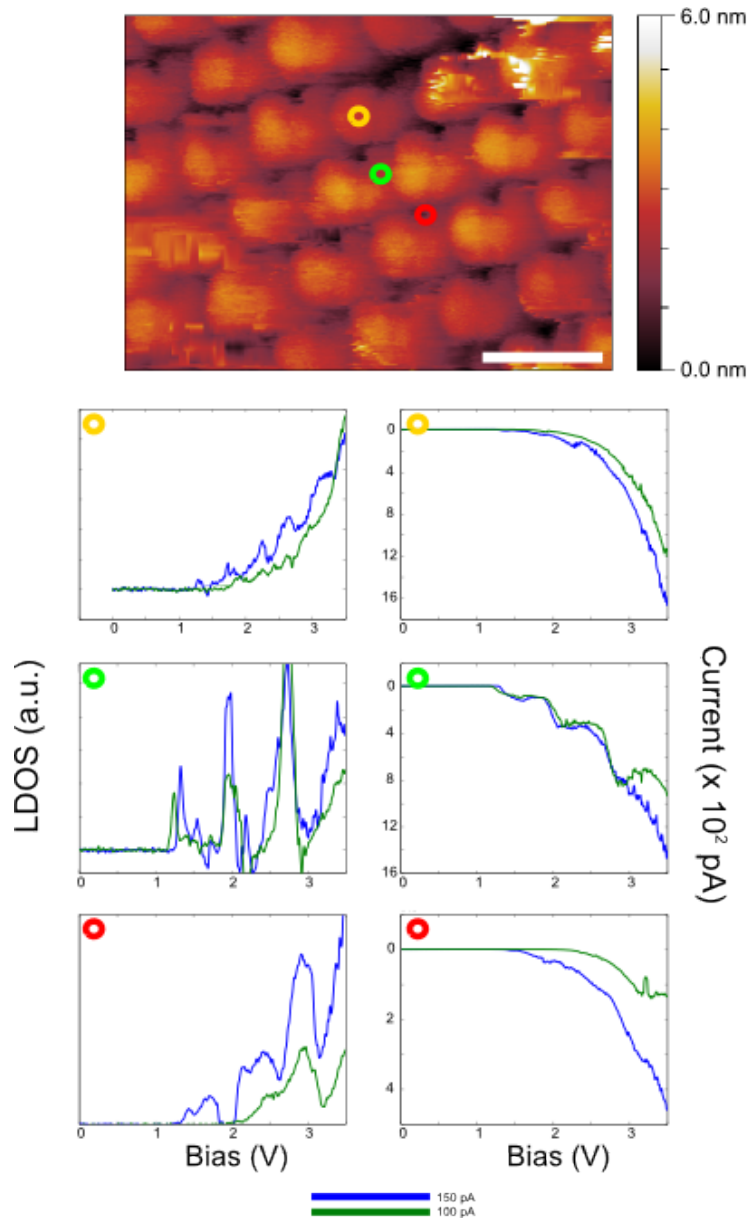


Figure 6.28: Spectroscopy on another area of a silicene supercrystal. Scan parameters  $V= 3.5$  V,  $I= 10$  pA, scalebar denotes 10 nm. These spectra were recorded with an oscillation amplitude of 50 mV at 730 Hz and a lock-in sensitivity of 100 mV at different setpoint currents.

In figure 6.28 the spectroscopy experiments are repeated on a different part of the supercrystal and for two different current setpoints, i.e. 100 and 150 pA. Again the silicene lattice in the image is clearly observed. When taking the spectra at the three different positions, the tip appears slightly more stable than during the previously described experiment. Whether this is due to a cleaner sample surface or due to a more stable tip is unclear. Again sharp resonances are observed, which appear to have an on-set of conductance slightly below 1.5 V. The position of the resonances again varies substantially from position to position and especially at the red position the tip stability is questionable.

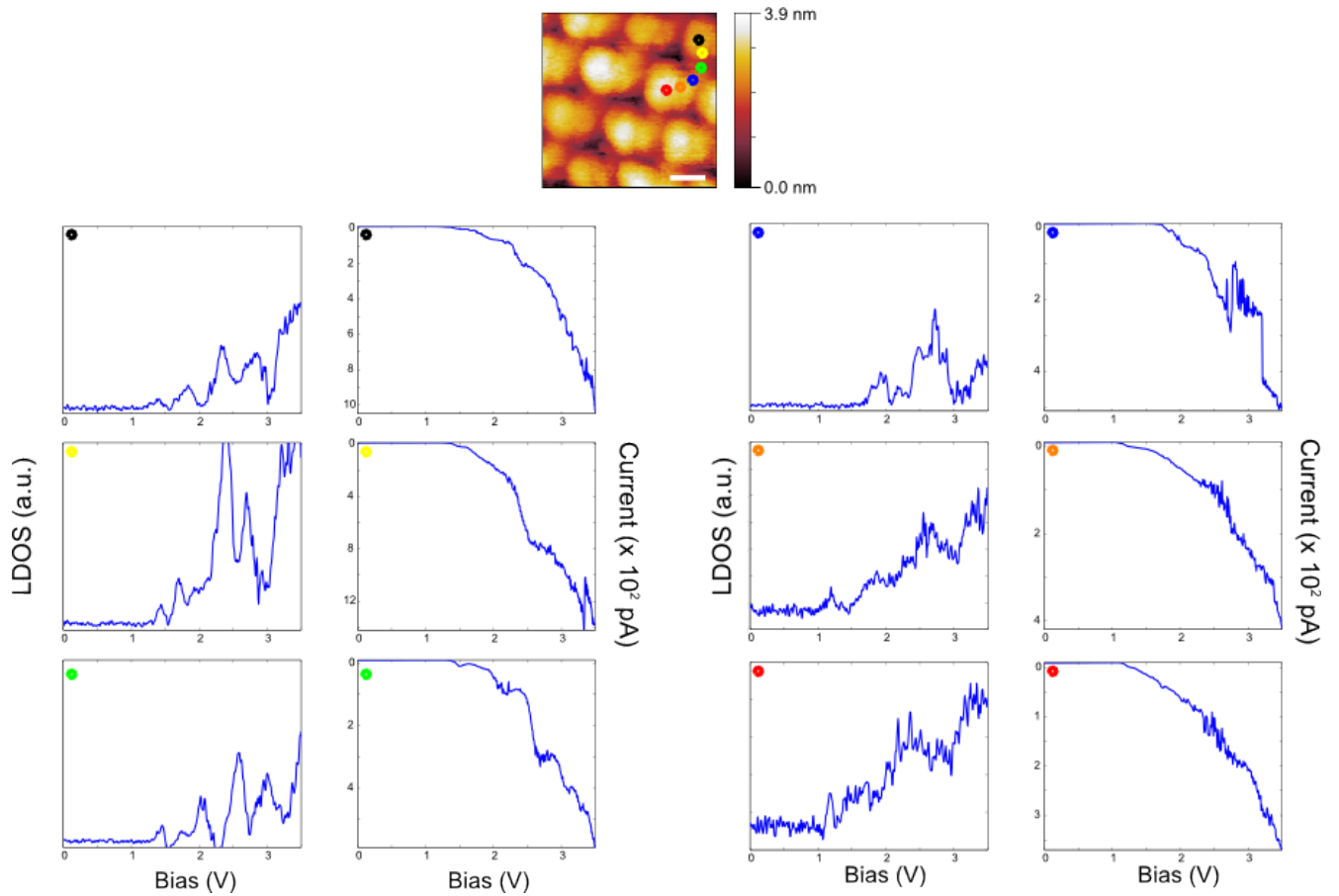


Figure 6.29: Spectroscopy on another area of a silicene supercrystal. Scan parameters  $V=3.5$  V,  $I=10$  pA, scalebar denotes 5 nm. These spectra were recorded with an oscillation amplitude of 20 mV at 730 Hz and a lock-in sensitivity of 100 mV. All spectra were recorded at a setpoint current of 50 pA.

Figure 6.29 describes another spectroscopy experiment at yet another position on the silicene supercrystal. An attempt was made to take a series of spectra going from an A-position to an adjacent A-position via a B-position. Tip stability was maintained during the first three spectra. However, when the fourth spectra retrace started this stability was lost, as can be seen by the hairy features in the spectrum. Presumably the tip has picked up a molecule present on the substrate. This is even more reflected in the spectra taken at the orange and red positions. From the first three spectra it can be seen again that similar features are observed as in the previous experiments; the onset of conductance lies slightly below 1.5 V and the resonance structure at higher biases is comparable.

An attempt to initial interpretation of the spectra can be done. The first resonances, lying between 1.5 V and 2.0 V belongs to the first  $s$ -band of the band structure. The first resonance belongs to the lowest  $s$ -band and accordingly the second resonance belongs to the upper  $s$ -band. The distinctive 'M'-shape of the band can be recognized in a couple of the acquired spectra. The second 'M'-shape, which is seen less often in the spectra and lying between 2.0 V and 3.0 V, belongs to the dirac  $p$ -bands. Even higher resonances could belong to the other  $p$ -bands. Even though some remarkable features are already observed in the obtained spectroscopy curves, improvements to these measurements have to be made. To start of the metallic nature of the

tip has to be verified every couple of spectra in order to be able to interpret the spectra truthfully. Also the way we collect data can be improved by using grid spectroscopy; a sub-grid is positioned over the scan image and at every point in this subgrid a spectrum is taken. This can be extended into overnight measurements. These experiments have already been started and have resulted in a few hundred spectra, yet to be interpreted. Furthermore these experiments can also be done at different current setpoints, to ensure that the spectra are taken in the shell-tunneling regime.

# Chapter 7

## Conclusions and outlook

”It’s more fun to arrive at a conclusion than to justify one ” - Malcolm Forbes

### 7.1 Conclusion and discussion

The work described in this thesis gives a solid foundation for future experiments. It is shown that various atomically coherent nanocrystal superlattices can be formed by changing synthesis parameters, such as concentration and temperature. Upon increasing concentration superlattices with linear, square and honeycomb geometry are formed. The supercrystal synthesis proves to be highly sensitive to the ligand concentration present in the ethylene glycol. By increasing the oleic acid concentration we can quench the oriented attachment process completely. Also molten structures were obtained. Once the nanocrystals are fully stripped of their ligand layer, little to no control over the growth of the supercrystal is preserved, resulting in superlattices where the individual nanocrystals cannot be resolved anymore (i.e. molten structures). We have shown that the process can be controlled by adding a minute amount of oleic acid to the ethylene glycol prior to adding the nanocrystal dispersion. Initial experiments on stripping the supercrystal from their capping layer have been performed as well, by immersing the supercrystals into a solution containing Meerwein’s salt. Further proof of the removal of the oleic acid from the superstructure has yet to be obtained. The linear and square supercrystals were obtained and analyzed. We have shown that the linear chains attach via the  $\{100\}$  facets, but sometimes connect via different facets, buckling the supercrystal. The square lattices also attach via the  $\{100\}$  planes and form large, defect-free sheets. The honeycomb crystal has proven to be quite intriguing. We have used a combination of TEM, STM, Electron Tomography, HR-SEM and HAADF-STEM to proof that its geometry is not graphene-like but silicene-like. In the silicene-like supercrystal the facets of the nanocrystals attach via the  $\{111\}$  planes. It is shown that the contrast in STM experiments is largely determined by the radius of curvature of the tip. Three different image contrasts are obtained: hexagonal, honeycomb and silicene-like on roughly the same area. We conclude that the hexagonal contrast is caused by measurements with a blunt tip, where we are only able to image one of the sublattices in the honeycomb supercrystal. Initial STS experiments have been performed on the honeycomb supercrystal. The acquired results show interesting features, which substantially deviate from spectra one would expect in a 2DEG. Future experiments will have to show whether we are really measuring individual nanocrystal properties or the interesting collective features arising from the supercrystal.

## 7.2 Outlook

More experiments on the supercrystal synthesis stability are necessary in order to increase its reproducibility. Already a glovebox dedicated to oriented attachment experiments is present in the laboratory now, which is a tremendous help. Furthermore for STM experiments it is desired to strip the nanocrystals of their ligand layer. First experiments using Meerwein's salt have already been performed, but do not give enough proof of the removal of oleic acid. Infrared spectroscopy (in reflection mode) could be performed to check for the presence of CH and CO stretching vibrations. More spectroscopy experiments should be performed on the CdSe based superlattices. We have presented some initial results, but more data can be acquired using grid spectroscopy. Furthermore tip stability can be improved and the metallic nature of the tip should be verified after the experiments on the HOPG substrate. Furthermore wavefunction mapping can be performed to measure the spatial extend of the electronic states. This should give definite proof whether the states are located on one NC (and hence a single NC property) or delocalized over the supercrystal (making it a collective electronic property). STS should be performed on the different types of supercrystals, i.e. linear and square geometry and based on different materials (PbSe and CdSe). More ion exchange can be performed and other materials could be made as well.

In order to study the electronic properties in reciprocal space, thereby elucidating the entire dispersion relation of the supercrystals, angle resolved photo-electron spectroscopy (ARPES) can be performed. By varying the polar and azimuthal angles between the detector and the sample the  $E - k$  relation can be mapped through the entire Brillouin-zone of our structures. From the dispersion relation a vast amount of data can be obtained, such as whether the systems display linear dispersion and group velocities.

We can say without exaggeration that the formation of the superlattices is a really intriguing mystery that has to be studied in detail. To elucidate the mechanism of formation, the use of in-situ time-resolved grazing-incidence small angle x-ray scattering (GISAXS) is proposed. The degree of atomic coherence will be addressed using high-resolution grazing incidence diffraction (GID) with sub micron beams. By performing the experiments under grazing incidence we ensure that the beam only probes the liquid-air interface at most 10-20 nm deep into the nanocrystal dispersion. This gives us the opportunity to do time-dependent studies on the formation of the supercrystal, both probing the atomic and nanocrystal alignment of the particles during oriented attachment.

The experiments described in this outlook will shed light on the unique electronic properties of 2D supercrystals. Combined with the theoretical framework discussed above this will hopefully lead to an understanding of the electronic properties of the supercrystals in direct and reciprocal space. The purpose of these experiments is to do fundamental chemistry and physics on novel two-dimensional supercrystals. The systems which are studied are ideal candidates to host interesting phenomena, such as (linear) dispersion of the electronic bands, increased spin-orbit coupling, strong light-matter interaction, etc.. With an eye on fundamental studies, but not losing sight of possible applications, this project is bound to be of enormous interest in the nanoscience community.

# Bibliography

## 7.3 Bibliography

- [1] Bealing, C. R., Baumgardner, W. J., Choi, J. J., Hanrath, T. & Hennig, R. G. Predicting nanocrystal shape through consideration of surface-ligand interactions. *ACS nano* **6**, 2118–27 (2012).
- [2] Fang, C., van Huis, M. A., Vanmaekelbergh, D. & Zandbergen, H. W. Energetics of polar and nonpolar facets of PbSe nanocrystals from theory and experiment. *ACS nano* **4**, 211–8 (2010).
- [3] Schapotschnikow, P., van Huis, M. A., Zandbergen, H. W., Vanmaekelbergh, D. & Vlugt, T. J. H. Morphological Transformations and Fusion of PbSe Nanocrystals Studied Using Atomistic Simulations. *Nano Letters* **10**, 3966–3971 (2010).
- [4] Cerf, R. *The Wulff Crystal in Ising and Percolation Models* (2006).
- [5] Wulff, G. No Title. *Zeitschrift für Kristallographie und Mineralogie* **105**, 449–530 (1901).
- [6] Swart, I. *Solids and Surfaces - Reader* (2012).
- [7] Evers, W. H. *et al.* Low-Dimensional Semiconductor Superlattices Formed by Geometric Control over Nanocrystal Attachment. *Nano Letters* **13**, 2317–2323 (2013).
- [8] de Mello Donegá, C. Synthesis and properties of colloidal heteronanocrystals. *Chemical Society reviews* **40**, 1512–46 (2011).
- [9] Groeneveld, E. *Synthesis and Optical Spectroscopy of (Hetero)-Nanocrystals - An exciting interplay between chemistry and physics*. Ph.D. thesis (2012).
- [10] Kittel, C., Zettl, A. & Mceuen, P. *Introduction to Solid State Physics* (2004), 8th revise edn.
- [11] Bloch, F. ber die Quantenmechanik der Elektronen in Kristallgittern. *Zeitschrift für Physik* **52**, 555–600 (1929).
- [12] Koole, R. *et al.* Optical investigation of quantum confinement in PbSe nanocrystals at different points in the Brillouin zone. *Small (Weinheim an der Bergstrasse, Germany)* **4**, 127–33 (2008).
- [13] Overgaag, K., Liljeroth, P., Grandidier, B. & Vanmaekelbergh, D. Scanning Tunneling Spectroscopy of Individual PbSe Quantum Dots and Molecular Aggregates Stabilized in an Inert Nanocrystal Matrix. *ACS Nano* **2**, 600–606 (2008).

- [14] Koole, R. *Fundamentals and Applications of Semiconductor Nanocrystals : A study on the synthesis, optical properties, and interactions of quantum dots*. Ph.D. thesis (2008).
- [15] Houtepen, A. J. *Charge injection and transport in quantum confined and disordered systems*. Ph.D. thesis (2007).
- [16] Sun, Z., Swart, I., Delerue, C., Vanmaekelbergh, D. & Liljeroth, P. Orbital and charge-resolved polaron states in CdSe dots and rods probed by scanning tunneling spectroscopy. *Physical review letters* **102**, 196401 (2009).
- [17] Kalesaki, E., Delerue, C., Morais Smith, C. & Vanmaekelbergh, D. Dirac-type Conduction Bands in 2D Zincblende Semiconductors imposed by a Honeycomb Nanogeometry. *Submitted* .
- [18] Geim, A. K. & Novoselov, K. S. The rise of graphene. *Nature Materials* **6**, 183–191 (2007).
- [19] Geim, A. K. & MacDonald, A. H. Graphene: Exploring Carbon Flatland. *Physics Today* **60**, 35 (2007).
- [20] Novoselov, K. S. *et al.* A roadmap for graphene. *Nature* **490**, 192–200 (2012).
- [21] Novoselov, K. S. *et al.* Two-dimensional gas of massless Dirac fermions in graphene. *Nature* **438**, 197–200 (2005).
- [22] Rashba, E. I. Looking Back. *Journal of Superconductivity* **16**, 599–623 (2003).
- [23] Binnig, G., Rohrer, H., Gerber, C. & Weibel, E. Surface Studies by Scanning Tunneling Microscopy. *Physical Review Letters* **49**, 57–61 (1982).
- [24] Binnig, G. & Quate, C. F. Atomic Force Microscope. *Physical Review Letters* **56**, 930–933 (1986).
- [25] Giessibl, F., Hembacher, S., Herz, M., Schiller, C. & Mannhart, J. Stability considerations and implementation of cantilevers allowing dynamic force microscopy with optimal resolution: the qPlus sensor. *Nanotechnology* **15** (2004).
- [26] Gross, L. Recent advances in submolecular resolution with scanning probe microscopy. *Nature chemistry* **3**, 273–8 (2011).
- [27] Millikan, R. A Direct Photoelectric Determination of Planck’s ”h”. *Physical Review* **7**, 355–388 (1916).
- [28] GURNEY, R. W. & CONDON, E. U. Wave Mechanics and Radioactive Disintegration. *Nature* **122**, 439–439 (1928).
- [29] Bardeen, J. Tunnelling from a Many-Particle Point of View. *Physical Review Letters* **6**, 57–59 (1961).
- [30] Chen, c. J. *Introduction to Scanning Tunneling Microscopy* (2008).
- [31] Tersoff, J. & Hamann, D. R. Theory and Application for the Scanning Tunneling Microscope. *Physical Review Letters* **50**, 1998–2001 (1983).
- [32] Gross, L. *et al.* High-Resolution Molecular Orbital Imaging Using a p-Wave STM Tip. *Physical Review Letters* **107**, 086101 (2011).

- [33] Overgaag, K. *et al.* Electron-phonon coupling and intervalley splitting determine the linewidth of single-electron transport through PbSe nanocrystals. *The Journal of chemical physics* **131**, 224510 (2009).
- [34] Jdira, L. *et al.* Scanning Tunnelling Spectroscopy on Arrays of CdSe Quantum Dots: Response of Wave Functions to Local Electric Fields. *Nano Letters* **8**, 4014–4019 (2008).
- [35] Overgaag, K. *Electronic Coupling in Self Assembled Nanocrystal Arrays - a scanning tunneling microscopy study*. Ph.D. thesis (2008).
- [36] Steckel, J. S., Yen, B. K. H., Oertel, D. C. & Bawendi, M. G. On the Mechanism of Lead Chalcogenide Nanocrystal Formation. *Journal of the American Chemical Society* **128**, 13032–13033 (2006).
- [37] Boneschanscher, M. P. *Structural Analysis and Modeling of Nanocrystal Superlattices*. Ph.D. thesis (2009).
- [38] Friedrich, H. *Quantitative Electron Tomography for Nanostructured Materials*. Ph.D. thesis (2009).
- [39] Friedrich, H. *et al.* Quantitative Structural Analysis of Binary Nanocrystal Superlattices by Electron Tomography. *Nano Letters* **9**, 2719–2724 (2009).
- [40] Boneschanscher, M. P. *et al.* Electron Tomography Resolves a Novel Crystal Structure in a Binary Nanocrystal Superlattice. *Nano Letters* **13**, 1312–1316 (2013).
- [41] Rosen, E. L. *et al.* Exceptionally mild reactive stripping of native ligands from nanocrystal surfaces by using Meerwein’s salt. *Angewandte Chemie (International ed. in English)* **51**, 684–9 (2012).
- [42] Dion, M., Rydberg, H., Schröder, E., Langreth, D. & Lundqvist, B. Erratum: Van der Waals Density Functional for General Geometries [Phys. Rev. Lett. 92, 246401 (2004)]. *Physical Review Letters* **95**, 109902 (2005).
- [43] Klimeš, J. & Michaelides, A. Perspective: Advances and challenges in treating van der Waals dispersion forces in density functional theory. *The Journal of chemical physics* **137**, 120901 (2012).
- [44] Langreth, D. C. *et al.* Van der Waals density functional theory with applications. *International Journal of Quantum Chemistry* **101**, 599–610 (2005).
- [45] Vydrov, O. A. & Van Voorhis, T. Improving the accuracy of the nonlocal van der Waals density functional with minimal empiricism. *The Journal of chemical physics* **130**, 104105 (2009).

# Acknowledgements

”No duty is more urgent than that of returning thanks.” - James Allan

The most fun part to write of the entire thesis in my opinion; the acknowledgements. It allows me to express my sincere gratitude to each and every person who has helped me accomplish this work, which is more than necessary I would say!

To start I would like to thank the professor who allowed me to perform these cool experiments in his group, prof. Daniel Vanmaekelbergh. Your tremendous insights, positive attitude and dry sense of humor made it a pleasure to work here. The continuous interest in the results I obtained were a great boost to my motivation.

Then there is Mark. We first met when I did my bachelor thesis in this group and we have had some very interesting discussions during those days. It was also at this time that you started grasping my curiosity for the ’beast in the basement’, the STM/AFM. At the end of my bachelors we had a discussion and I asked if I could do my thesis with you. This resulted in the thesis here. I cannot thank you enough for your inspiring guidance throughout the last two years, I will do my best to give the level of support to my students as you did to me! (p.s. Thanks for the naturemagnourl superlatex file!)

After already doing research for over six months here, Ingmar joined the group as an assistant professor. This changed the attitude of the group a bit (for the better!). Everything tidied up and we were able to do some cool upgrades on the machine. Your help and always critical insights on my work were inspiring and allowed me to bring up my work to another level. Then all of a sudden you asked me what I wanted to do after my masters and you nominated me for the DINS graduate programme. This allowed me to write my own proposal for a Ph.D. position, which was awesome! A lot of work, but awesome. Not only did you help me correct my proposal, you were also willing to become a copromotor for my promotion. I cannot thank you enough for the help and everlasting patience with me over the past one-and-a-half years, even more so as I actually got the position! Furthermore I would like to thank Andrei Petukhov and Frank de Groot for also helping me writing the proposal, thanks a million!

During my work here I was ’stuck’ in the basement for quite a while. Luckily for me there was plenty of company. Joost was mostly there to join me with his extremely dry sense of humor and witty remarks. You helped me a lot getting started with the setup and correcting silly mistakes I made (I am still very sorry that I dropped your Au crystal!). Thanks a million for helping with everything man! Also Peter joined in after a year as a student working for Joost. Your talents as both a chemist and physicist and continued interest in everything were a great help! I also have to mention Rogier, whose work I continued during the first few months of my stay at the CMI group. Kiane also had a brief visit for her bachelor thesis in the basement, thanks for the pleasant company! I also would like to gratefully acknowledge Peter Liljeroth, who was not here in Utrecht very frequently, but whose ideas always inspired everyone for some new experiments!

Now that I have adressed every person in the basement its time to go upstairs. I have had the pleasure to work in the CMI group with a number of great people. A person who has helped me tremendously during my thesis is Wiel, also known as the guy with the golden hands. Your synthesis skills are unmatched and your help with the supercrystals was awesome! I am looking forward to more collaboration during my Ph. D.! I also would like to thank Chen Hu for the tremendous effort she has put in measuring the SEM images. Then there is Hans, our lab technician, who is more of a metaphore than a person. Every group should have a Hans! I'd like to thank Stephan for his help with computer problems and the numerous hours we spend at the TEM. Relinde, I'd like to thank you as well for your continued interest and TEM sessions. Together with Freddy, Ward, Dariusz, Francesca and more people you have made the hours on the fifth floor of the Kruyt building more pleasant. Mathijs, Bert, Zachar, Arnoud, Yiming, Yu, Marianna, Freddy (thanks for your amazing mathematica and theoretical help!), Dominika, Rashid, Nico, Robin, Quinten, Eline, Joren, Jacobien, Josine, Jantina, Daniel Gamelin (thanks for the cool lectures on magnetic quantum dots!), Christophe Delerue (your lectures on solid state physics were enormously clear!). I would also like to give a special thanks to Harold de Wijn, who's put a major effort in giving physics lectures for chemists. I have learned a great deal in these classes!

Everyone needs some diversion every once in a while after work. For me this started with the Lifeguards in Bunschoten. Every monday I thought kids to swim and save other people in the water. Thanks everyone from the RBS, and ofcourse also from Texel (TRB), where I spend (and will keep spending) my summers on the beaches! Let's just hope we do not run into 'Satan the Seal' again, haha.

Besides swimming and running I discovered a whole new passion which I never thought I would like; dancing. Passion maybe is not the correct word, it has become more like an addiction. Starting with salsa and bachata (and later on ballroom, latin, argentine tango, zouk and others), Udance has opened a whole new world for me. Together with Jeffrey (physics ftw!) and Wout (maths ftw!) and many others, dancing snuck into my life. Nowadays, every tuesday and thursday evenings are spend in the city doing salsa with a lot of people! This diversion might be the biggest one up to now and I'd like to thank each and every person who guided (mr. Percy!) and joined (all Udancers!) me on this trip over the last year. I JUST WANNA FEEL... UDANCE!

As a person I feel very lucky to have many close friends. Within the university I spend most of my time with Dide (and Kevin), Léon (and Sharon) and Dayinta (and Rutger). I feel so lucky to have you guys as close friends! Together with Danny we shared lots of great memories. We followed quite the number of courses together and studied for hours and hours (with most of the time me teaching you how to solve certain problems, which was great!). I think both Dide and Léon will pursue me in an academic carreer, the both of you are capable enough! In four years we will give a tremendous party when we're all at the next step of our careers! Thanks a million for joining me on this journey and I hope we may have many more (dinners, parties, holidays, etc.) in the future! I also owe Maarten, who was lucky enough to spend a major time in Spain during his studies, thanks. You have turned over to the dark (nanotech) side of chemistry, woohoo!

During my master I also got a place of my own (finally!), moving out approximately 1.5 years ago. Luckily Jeroen got me in at AL16, which made it possible for me to extend my sleep up to about 8:30. Thanks for the awesome time we shared there! I would also like to thank Iris, Maurits, Rens, Lilian, Sven, Jasper and all other 'hallmates' which made my stay there more pleasant. I'm not sure how long I will still live there, but I would like to thank each everyone of my roommates for the great time I have here.

Family is very important as well, this became even more clear to me over the past two years. I have two great sisters who are always very interested in my, lets call it, well being. Naomi, thanks for your cookies every once in a while, haha! This made my grade go up by at least one point! Marieke and Nadin, thanks for having me over in the weekends. I love being over, as I get to see my two biggest friends Jayden and Bas and my princess, Vayenne! Dad, thanks for always supporting me. You were always pushing me to my greatest extend, helping me study and do what I love the most, and for this I can never thank you enough. Remind me that I spend my first salary on some 'thank you' gift for you!

Last but not least, I would like to thank my mom, who has passed away two and a half years ago. Although you are physically not with us anymore, your support and pride throughout the years have shaped me into who I am today. Thanks for everything and keep a watchfull eye on me during my next adventures.

## Appendix A

# Ab Initio Density Functional Study of the Energetics of PbSe Nanocrystal Facets through Passivation by Capping Ligands

The surface energy of PbSe nanocrystal facets is studied by an *ab initio* Density Functional Theory study. We implement Dion's Van der Waals functional at the PBA\_GGA level using the VASP code. Allowing full relaxation of both the passivating molecule and the surface, it is shown that rigorous rearrangements take place, both in the surface geometry and surface energy. This study allows for further understanding and control of the overall nanocrystal shape, leading to the design of novel functional materials.

### Introduction

The overall properties, both physical and chemical, of a nanocrystal (NC), such as molecule adsorption, crystal morphology and growth are mostly depending on the atomic structure of the surface and its energetics. For structure in this size regime, the surface energy becomes an increasingly important factor to the overall free energy due to the large surface to volume ratio. These surface energies can be modified by addition of capping ligand, stabilizing or destabilizing specific crystal facets. Knowledge on how the overall energy changes as a function of surface passivation is of tremendous importance in controlling the overall NC synthesis and eventually processing them into novel materials. Over the last years, PbSe NCs have been studied intensively due to their attractive electronic and optical properties and promising applications in near-infrared photovoltaics. Recently it has been shown that PbSe truncated nanocubes can be fused together to form atomically coherent supercrystals with linear, square and honeycomb morphologies [7]. Especially the honeycomb lattice is very interesting due to its direct analogy with graphene. Understanding the process of formation, which is dominated by surface energetics of the PbSe nanocubes, is of great importance. A suggestion on the driving force between the oriented attachment is the electric charge on the PbSe NCs. Although it has been experimentally confirmed that the {111} Pb and Se facets are dipolar in nature, the above statement on the oriented attachment has not been confirmed.

Recently new exchange correlation functionals were proposed by Dion et. al. to implement Van der Waals (VdW) interactions into novel density functional theory calculations (DFT) [42]. Van der Waals forces do not originate from exchange interactions, however some approximations

have been made to the reduced density gradient in order to get a comparison with experiment. For the correlation part of the functional, Dion has derived an expression for two jellium slabs which assumes planar symmetry and pairwise additivity of the electron-electron interactions. The total expression for the exchange correlation functional becomes

$$E_{xc} = E_x^{GGA} + E_c^{LDA} + E_c^{nl} \quad (\text{A.1})$$

The terms on the right hand side are the exchange energy, the LDA correlation energy and the non-local correlation energy term, which accounts for the long range VdW interactions. Combined, these terms are called the van der Waals density functional (vdW-DF). Recently the functional was slightly modified by Klimes et. al. [43] for applications on solid state systems (plane-wave basis sets instead of Gaussians plus extension to three-body interactions) [44; 45]. More recently a theoretical study by Bealing et. al. has shown that the oleic acid passivation can be simulated by an acetate ion, which reduces the computational effort tremendously [1]. However, in this study the surface slab and capping ligand were optimized separately and only static calculations on the surface-ligand complex were performed. Furthermore, only the on-top position was assumed, placing the acetate ion directly above a Pb atom. By using Dion's vdW-DF we show that the surfaces relax in different fashions for various ligand positions and, hence, the surface energy is different for different adsorption geometries.

Table A.1: Results for unpassivated surfaces.

| Crystal plane     | $\gamma_{surface}$ (Jm <sup>-2</sup> ) calculation | $\gamma_{surface}$ (Jm <sup>-2</sup> ) literature | Comment        |
|-------------------|--|---|----------------|
| {100}             | 0.382  | 0.184   | –              |
| {110}             | 0.309  | 0.318   | –              |
| {111}-Pb nonpolar | –  | 0.328   | No convergence |
| {111}-Se nonpolar | –  | 0.419   | No convergence |

## Surface energetics

In order to obtain the surface energy of the various crystal facets, surface slabs were build. The slab is terminated by the facet of interest and perpendicular to the surface a column of atoms is build, which again is terminated by the facet of interest. The surface energy of a specific crystal facet can then be calculated according to the formula below;

$$E_{surf}^{hkl} = \frac{E_{slab}^{hkl} - \frac{n_{slab}}{n_{bulk}} E_{bulk}}{2A} \quad (\text{A.2})$$

Here  $E_{surf}^{hkl}$  denotes the surface energy of a crystal facet with indices {hkl},  $E_{slab}^{hkl}$  is the energy of the bare surface slab and  $E_{bulk}$  is the energy of the bulk crystal, as obtained by the periodic DFT calculations. Note that the bulk energy is corrected for the ammount of atoms in the surface slab unit cell by a factor  $\frac{n_{slab}}{n_{bulk}}$ .

## Acetate ion

For binding energy calculations the acetate ion was allowed to relax in order to obtain the equilibrium geometry and energy. The acetate ion (CH<sub>3</sub>COO<sup>-</sup>) was constructed from scratch with chemical intuition. Upon relaxation (as an anion) both carbon atoms moved outward as can be seen in figure 1 (A). This can be solved by adding a Na<sup>+</sup> ion to neutralize the molecule, this way a chemically reasonable configuration was obtained. However, since energy calculations should

be performed with the anion only, the sodium ion had to be omitted. Geometry optimization with a Gaussian basis set resulted in convergence into a reasonable configuration without a positive counter ion. The energy of the as obtained configuration was calculated again with a plane wave basis set for later use.

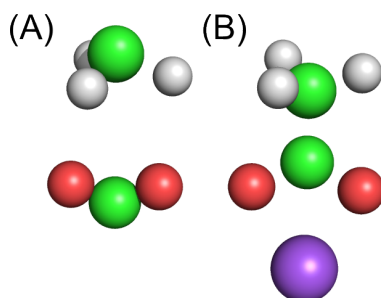


Figure A.1: Resulting acetate ion geometries for the negative ion alone (A) and overall neutral sodium acetate molecule (B). Both of these calculations were performed with a plane wave basis set in VASP. Red=hydrogen, white=hydrogen, black=green.

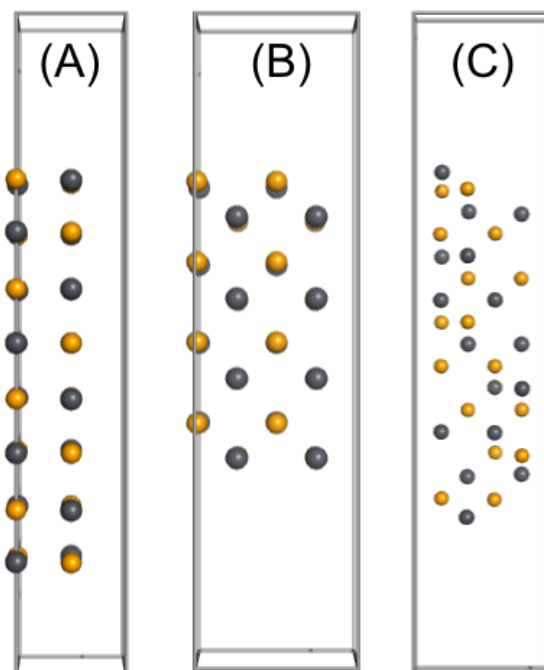


Figure A.2: Constructed supercells for the  $\{100\}$  (A),  $\{110\}$  (B) and  $\{111\}$  (C) surfaces. The  $\{111\}$  surface was constructed for both Pb and Se terminated nonpolar configurations. Black=lead, yellow=selenium.

## Bare surfaces

The results from the calculations are summarized in table 1. The calculated surface energies are given and values from literature are shown as a reference. For the  $\{100\}$  surface the energies differ substantially. The calculations were repeated several times with different cutoff energies

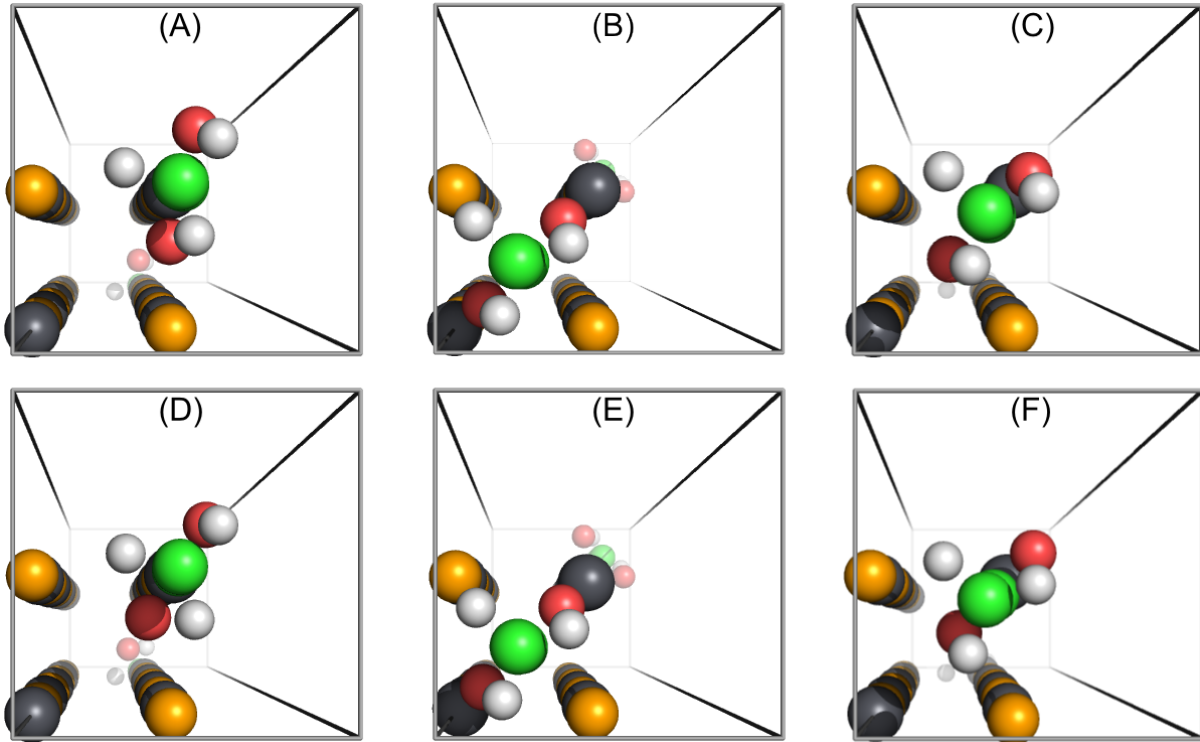


Figure A.3: Initial (A-C) and final (D-F) configurations; On top (A,D), bridged (B,E) and off-center (C,F).

and k-mesh values, however the obtained energy only slightly varied. Hence the difference in energy must originate from the non-local correlation term, which is the difference between the PBA\_GGA functionals used in this study and in reference [1]. Using the vdW-DF we found that  $\gamma_{100} = 0.382 \text{ Jm}^{-2}$ . For the  $\{110\}$  surface reasonable agreement is reached between the obtained results and literature. Full convergence was reached and a surface energy was found of  $\gamma_{110} = 0.309 \text{ Jm}^{-2}$ . Why the  $\{100\}$  is less stable than the  $\{110\}$  facet and why a better agreement was found for the  $\{110\}$  surface remains unclear. For the  $\{111\}$  surface non polar surfaces, were constructed as the polar surfaces are unstable without passivation. For the used Pb and Se non polar surfaces no convergence was reached. During the initial electronic convergence steps, the calculations stopped after a maximum of ten iterations. Many attempts to solve these problems have been tried, however none succeeded.

## Surface passivation

The relaxed acetate ion was used to find the equilibrium configuration and energy for a passivated PbSe surface. For the  $\{100\}$  facet this was done by positioning the acetate ion on top of a Pb ion with the carboxylate oxygen-oxygen bridge ( $\text{COO}^-$ ) direction slightly tilted away from the Pb-Se bond direction ( $13^\circ$ ), avoiding the initial configuration to be a local minimum. This can be seen in figure 3 (A). Different starting positions have been studied as well to obtain the energetically most favorable configuration, viz. bridged and arbitrarily placed. Geometry optimization resulted in the systems seen in figure 2 (D-F). Clearly a  $45^\circ$  angle is preferable for the ion in the on top position. Upon placing the ligand in the bridged conformation, all lattice ions move toward the acetate ion. The off center conformation relaxes to an on top

conformation with the  $45^\circ$  angle. Not only in the lateral direction an optimum configuration is found, also in the axial direction ions move upon introduction of the acetate.

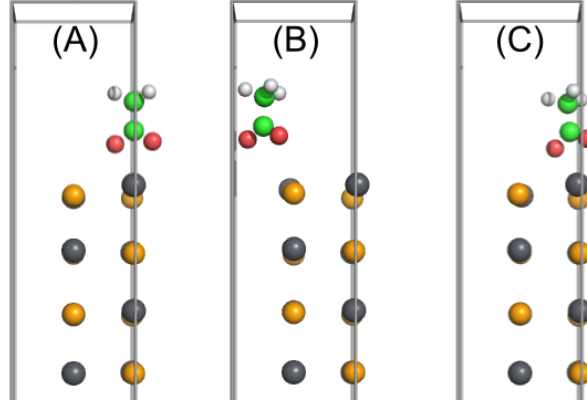


Figure A.4: Side views of the top half of the supercell, after convergence of the geometry optimization. The terminal Pb ions move out of their equilibrium position in the lattice when the acetate ion is added.

The shift of the ions is clearly shown in figure 4 and the results are summarized in table 2. Here  $|\mathbf{r} - \mathbf{r}_0|$  is the magnitude of the displacement vector of the lattice ion from their equilibrium position  $\mathbf{r}_0$ , upon passivation by the acetate ion. In the on-top position the Pb ion closest the acetate ion moves out of the lattice ( $0.90 \times a_0$ ). The distance between the other Pb ion in the same plane of height and the acetate ion is larger, hence there is less interaction between this ion and the ligand, and therefore moves a lot less;  $0.023 \times a_0$ . Second layer Pb ions move only  $0.017 \times a_0$  and  $0.006 \times a_0$ , this difference is caused most likely by the ligand at the other surface. Interestingly, the third layer ions move slightly more than the second layer ( $0.024 \times a_0$  and  $0.008 \times a_0$ ). This is because these are situated in the column of ions directly below the ligand, as in the first layer.

Also the bridged position of the acetate ion, i.e. between two Pb ions in the unit cell, has been considered. Here, the axial shifts are slightly larger (table A.3) with respect to the on-top position.

The off-center position was used as a reference calculations, to verify that the initial starting positions of the former configurations are not local minima. As can be seen in figure 4 (C), the acetate ion relaxes towards the on-top position. These configurations all have their own specific energy, the most favorable will be the naturally occurring configuration. With these energies we were able to calculate the binding energy of the acetate ion to the PbSe surface in each case;

$$E_{bind} = \frac{E_{slab+ligand} - E_{bare\ surface} - 2 \times E_{ligand}}{2} \quad (\text{A.3})$$

The obtained binding energies, for different acetate ion positions, are given in table 3.

This results in an energy of -2.35 eV for the on top configuration, -2.54 eV for bridged and -2.36 eV for off center. Moreover, the surface energy can now be determined for the passified surface;

$$E_{surf+ligand} = \frac{E_{slab+ligand} - \frac{n_{slab}}{n_{bulk}} E_{bulk} - 2 \times E_{acetate}}{2A} \quad (\text{A.4})$$

The obtained surface energies for both the on-top and bridged positions could not be determined accurately; as the acetate ion is allowed to relax in the supercell with the ligand, its

Table A.2:  $|\mathbf{r} - \mathbf{r}_0|$  (factor  $\times a_0$ )

|         | On top         | Bridged       | Off center     |
|---------|----------------|---------------|----------------|
| Layer 1 | 0.090 & 0.023  | 0.101 & 0.097 | 0.097 & 0.023  |
| Layer 2 | 0.017 & 0.006  | 0.018         | 0.014 & 0.011  |
| Layer 3 | 0.024 & 0.008  | 0.023         | 0.025 & 0.010  |
| Layer 4 | 0.003 & -0.005 | -0.002        | 0.002 & -0.003 |

energy can vary again. If we do calculate the binding energies in this manner, i.e. with the earlier obtained energy of the acetate ion, values of -0.599 and -0.677 Jm<sup>-2</sup> are obtained, which are unrealistic as they are negative. We can conclude, however, that the surface energy of the {100} facet goes down upon passivation.

Table A.3: Binding energies of several configurations after relaxation

|            | $E_{slab+ligand}$ (eV)    | $E_{binding}$ (eV) |
|------------|---------------------------|--------------------|
| On top     | $-0.17924587 \times 10^3$ | -2.3485765         |
| Bridged    | $-0.17961949 \times 10^3$ | -2.5353865         |
| Off center | $-0.17926544 \times 10^3$ | -2.3583615         |

## Conclusion

We have managed to calculate the effects of surface passivation by oleic acid on the PbSe {100} surface. Various efforts to run calculations on the {110} and {111} surface have been attempted as well, but failed to converge. The surface energy of the passified {100} facet goes down, but we obtained unrealistic values due to relaxation of the ligand, again changing its energy. The binding energy of the ligand to the {100} surface varies around 2.4 eV for the two different adsorption geometries. Further effort has to be made to extend the calculations to the other surfaces, as we are then able to study the impact of surface passivation on NC geometry by Wulff constructing the various surfaces.

The calculations performed in this appendix were done by L. Witteman and the author for the Advanced Quantum Modelling course at Utrecht University. The authors would like to acknowledge R. Koster and C. Fang for his help with calculations using the NanoCluster. Furthermore we would like to thank M.A. van Huis and I. Swart for usefull discussions.

## Methods

All calculations were carried out using the Vienna *ab initio* Simulation Program (VASP) employing density functional theory within the projector-augmented wave (PAW) method. A Generalized Gradient Approximation (GGA) by Perdew, Burke and Emzerhof (PBE) was used, which is adapted by Dion and Klimes to account for non-local exchange and correlation effects to account for VdW interactions. We tested different  $k$ -meshes from 4 x 4 x 4 to 30 x 30 x 30 for a conventional cell of bulk PbSe and different cutoff energies. These tests resulted in good convergence (<1 meV/atom). Calculations were computationally quite intensive; the passified surfaces took about a week to converge each with 32 cores on the NanoCluster at Utrecht University.

## Appendix B

# STM Tip Preparation by Electrochemical Etching and Fast Ion Bombardment

In order to achieve high lateral resolution the tips used in STM have to be extremely sharp. One way of achieving this is by electrochemical etching of the tips.

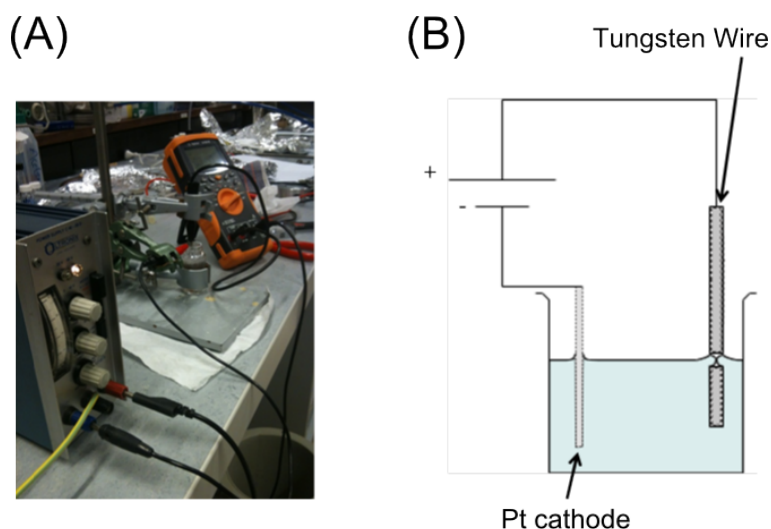
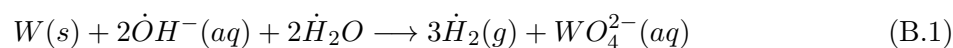


Figure B.1: Electrochemical etching setup. (A) Photograph taken of the used setup, a multimeter is inserted into the setup in order to measure the current during the etching process. (B) Schematic of the



We have used a 2M *KOH* solution as etching reagent. An over-potential is applied to the tip in order to drive the reaction. During the preparation of the tips, we have used a voltage of 6-10V, leading to currents of about 400-600 mA.

We have used a 2M *KOH* solution as etching reagent. An over-potential is applied to the tip in order to drive the reaction. In our case, we've used 6-10V, leading to currents of about 400-600 mA.

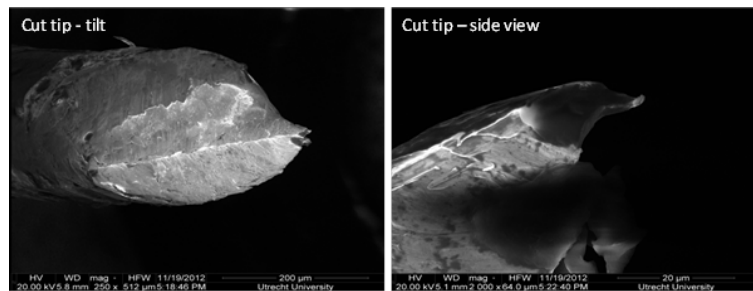


Figure B.2: Normally used tips. These are PtIr tips made by cutting with a scissor. As can be seen the outermost end of the tip is very ill defined.

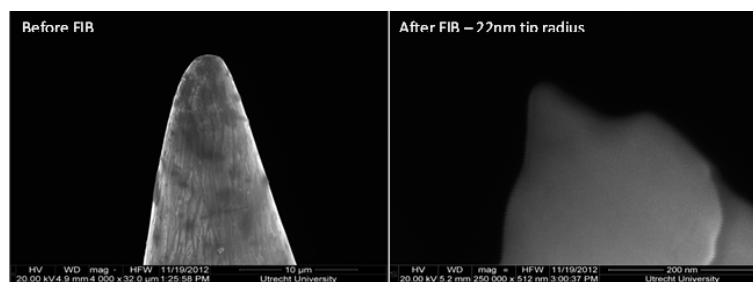


Figure B.3: First of the etched tungsten tips. The left image shows the pre-etched tip. The radius of the tip is about 1 micron. After FIB (image on the right), the radius of the tips is decreased to approximately 22 nm.

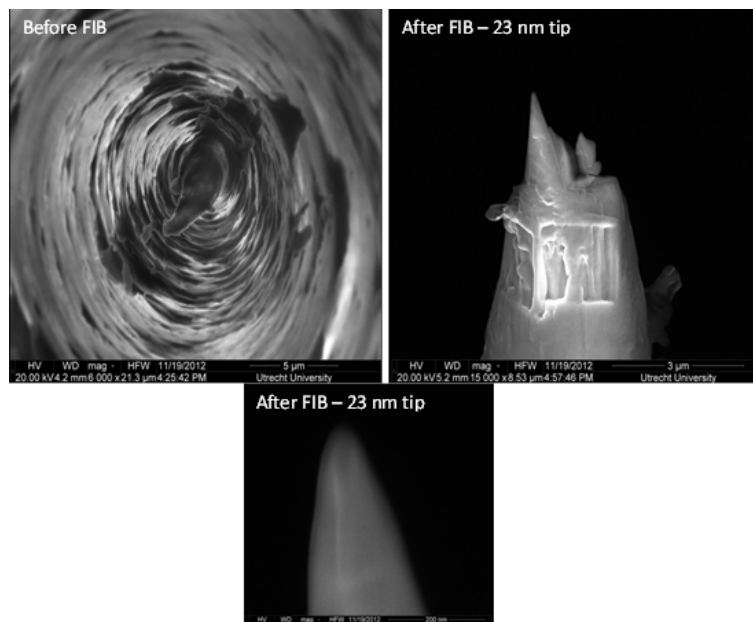


Figure B.4: Second of the etched tips. Top left image shows the etched tip from above. Top right and bottom images show the FIB'ed tip with a radius of approximately 23 nm.